FERMILAB-THESIS-1996-69

RICE UNIVERSITY

SEARCH FOR EVIDENCE OF PHOTOPRODUCTION OF HIGHER-TWIST QCD EVENTS AT EXPERIMENT 683 AT FERMI NATIONAL ACCELERATOR LABORATORY

by

MICHAEL TRAYNOR

A THESIS SUBMITTED
IN PARTIAL FULFILLMENT OF THE
REQUIREMENTS FOR THE DEGREE

DOCTOR OF PHILOSOPHY

APPROVED, THESIS COMMITTEE

Gordon Mutchler
Professor of Physics

Marjorie Corcoran
Associate Professor of Physics

Richard Wolf
Professor of Physics

HOUSTON, TEXAS
MAY, 1996

Search for Evidence of Photoproduction of Higher-Twist QCD events at Experiment 683 at Fermi National Accelerator Laboratory

by

Michael Traynor

Abstract

Experiment 683 at Fermilab Wide Band Photon Laboratory observed events via $\gamma p \rightarrow$ jets during the 1991-1992 fixed target run. The present analysis attempted to observe the **higher-twist** subprocess in QCD using that data to measure the $p_\perp$ spectrum via a clustering algorithm tuned to optimize the distinctive topology of higher-twist events. Results indicate a substantial $k_\perp$ promotion effect at lower $p_\perp$ and a significant NLO contribution to the photoproduction.

Table of Contents

Acknowledgements

In the category of professional acknowledgments, I would like to thank:

- SS Anselm and Aquinas. More than anyone else I know, they inspired me to attempt to bridge the fields of Faith and Reason. It has motivated me throughout my life so far. I can't say I have been totally successful, but I have learned a great deal in the attempt.

- John Marraffino. John was a constant source of advice and aid in explaining physics, mathematical methods, programming, library routines, and technical writing.

- George Chang. George has gone above and beyond the call repeatedly in helping me as a graduate student both academically and professionally. His work in physics is to be commended. I always knew that no question I had would be rejected as too dumb.

- Carol Hawk. There will be more later, but Carol has helped me with the understanding of photons, QCD, and *modern* computing techniques.

- Chafiq Halli. I have never seen a harder-working graduate student than Chafiq. He was thorough in his explanations and his aid in debugging the Beam Monte Carlo.

- Gordon Mutchler. He has been a very understanding and patient advisor.

- Med Webster for offering his name as a reference.

- Andy Hocker, Greg Morrow. Andy has been a source of aid in the format of the thesis and LaTeX. Greg has also aided in being a timely source of information included in this thesis.

- Jim Mcpherson, Phil Birmingham, Jianping Xu. Six months of Owl shift together without coming to blows–need I say more? Jianping deserves a great deal of respect for his work.

- Joel Butler. For his work in prolonging the timeframe of dismantling VMS on FNAL.

- Jorge Morfín. For reviewing the thesis and for many useful comments and suggestions.
- Arlene Lennox. I very much appreciate her effort in my career transition. Her work is exemplary and of vital importance.
- Jeff Owens. Jeff is the paragon of competence and friendliness. I was continually stunned by both his patience and his cooperation with my work–without any incentive on his part.
- Gunnar Ingelman, Ian Knowles. Torbjörn Sjörstrand. For writing the Monte Carlos relevant to this analysis and for personally explaining pheomena to me when I was utterly bewildered on Monte Carlos.
- The CDF graduate students and postdocs. Now I know why they discovered the top. Friendly, competent, and always willing to help with understanding physics and computing without being the slightest bit condescending.
- Rose Smith, Elaine Morris, Helen Viereck, and Wayne Robinson, the friendliest, most competent, and most helpful department aides I have ever seen.
- All the other wonderful E683 collaborators whose names escape me. I expect that the quality of treatment shown to me by them will return to them manyfold over their lives.

Eppur si muove.

In the category of personal acknowledgments, I would like to thank:

- Sharon Dulewski, James Baker, Robert Kman, Stephen Matuszak, Coach Rogowski, and Professor Bernard Norling. These teachers were the most supportive teachers I ever had. It meant a lot in these past few years that some teachers had confidence in my work.
- Frank Krohn from Sargent and Lundy for being a great friend when I could use one.
- My parents. The older I get the more astonished I am at the magnitude of the sacrifices my parents made for my sake. It is not the slightest bit of exaggeration to state that my parents devoted their lives for the sake of their children. I wish I could have given you more than I have. My mother has been an incredible support for her family. As for my father, I wish he had some idea of how talented he is. He showered love in every possible way on his children. I am proud to be his son.
- My sisters. Well, I will never forget the day that Angie saved my life from an oncoming car. Mary could (and should) have been able to get her Ph.D. Now she is helping her children to have the chances she didn't. Ruthie has been an inspiration in the past few years for uncountable reasons. Karyn has been an incredible sister. There are a lot of very young and formerly very sick children that owe their lives to her.
- My nephews and nieces. Teaching them has taught me continually what a joy it is to be able to help people. The dreams they have are achievable with the talent and work they show. I hope they have the opportunities God has given me.
- My uncles, aunts, and cousins. My uncle Sal–my godfather, every Christmas and birthday without fail brought me a present stressing development and encouraging curiosity.
- Niccolo Pintozzi, M.D. Dr. Pintozzi died recently, but his work lives on and on. Dr. Pintozzi would come into our house with five children, each sick, and treat them without charge. Dr. Pintozzi would have screaming bouts with patients who were not listening to his exotic suggestions such as exercise, nutrition, and discipline.

Dr. Pintozzi agonized over each sick and dying patient he had. Dr. Pintozzi worked until he was ninety without taking a vacation because of his devotion to his patients. Dr. Pintozzi tried **not** to prescribe unnecessary medicine and **not** to advise unnecessary sugery. Dr. Pintozzi lost more money by his compassion and competence than most doctors make in their lifetimes. Dr. Pintozzi was a wonderful man.

- The Hawk family. They have treated me like family from before the day I met them.
- John Marraffino. John was more than a workmate. John was a true friend. He was there during one particular crisis in my time here when I did not know where to turn. I can say with some assurance that I don't know if I could have finished school without his help.
- All my friends I have met over the years. One friend in particular, Ken Soergel, has been a constant (if virtual) late-night companion in multi-hour discussions of life, the universe, and the foibles of Notre Dame football. It is appreciated.
- WMVP–1000 AM. Yes, I know this is rather unusual, but in the past year or two I have had them on from 4pm-7am in my office while I was working on this analysis–they are friendly and competent in every area of sports (except they're too hard on the Irish). Brian, Norm, Lance, Jim, Cheryl, Les, Tom–if you ever want a tour of the lab, it's yours for the asking. We're right by the Kane County Cougars. Peter can come too, but he'd better be nice to the guards or they'll kick him off site!
- The ladies from FNAL Housing: Linda Olson-Roach, Pam Fox, Dianne Snyder, Jackie Cyko, and Cheryl Bentham. for their generally wonderful attitude and their incredible patience with someone who stayed for a-couple-months-more for four years. They had a unique talent to tolerate my Companions All Through my Stay.
- Binkley, Squeaky, Cindy, and Smoky, for their constant support.
- Carol Hawk. I mention her twice, because she was integral to the analysis professionally and personally. **Her** analysis and thesis is the best graduate student work I have ever seen without the slightest doubt in my mind. She has been doing the

work of a senior postdoc the past few years. I can say that she is the closest friend I have ever had and am ever likely to have. There are very few people in this world that I admire, but Carol is one. I am privileged to be a part of her life.

La dama nuestra, tienes mi vida en las manos.

List of Figures

List of Tables

1 Theoretical Overview

1.1 Overview of Photoproduction

1.1.1 What is Photoproduction?

Photoproduction is the production of particles and **jets** via the photon-parton interaction, mediated by the strong nuclear force (Quantum Chromodynamics or QCD) for resolved photons or via the electromagnetic force (Quantum Electrodynamics or QED) for direct photons. A jet is a well-collimated group of particles.

The formation of jets follows from one of the principles of QCD, the principle that bare quarks are unobservable. As a quark struck in an interaction moves away from its companions in a hadron, the force between the exiting quark and its companions increases along the line whose direction is defined by the exiting quark. Eventually, the energy density in the field increases to the point that a new q $\overline{q}$ forms in the line between the exiting quark and its former companions. This continues to happen as long as there is sufficient energy in the exiting quark and its new q-$\overline{q}$ pairs. As they in turn recede from each other, new q-$\overline{q}$ pairs are formed along that line between the quarks. Eventually a series of composite particles are produced along the direction of the exiting initial quark, forming a jet.

The photon acts as both a point particle (direct photons), and as a composite particle (resolved photons). This may seem nonintuitive at first; however, this is true at lower energies as well. For example, in the photoelectric effect, the photon acts purely directly, as it transfers the entirety of its energy to the struck electron according to the formula E=hν. However, the photon exhibits its resolved nature in pair-production. In pair production, the photon virtualizes into an e $\overline{e}$ pair based on the Heisenberg Uncertainty Principle. If the energy of the photon is greater than $2m_e$, and a nucleus exists nearby such that the virtual e $\overline{e}$ pair can balance momentum, a real e $\overline{e}$ pair forms.

Likewise in photoproduction, the photon virtualizes into q $\overline{q}$ pairs that are constantly forming, evolving, and annihilating. If the photon interacts with a nucleus while the q $\overline{q}$ pair is evolving, the q $\overline{q}$ pair emerges from the virtual sea, and either the quark or antiquark interacts separately with a quark from the nucleus. Indeed, the q $\overline{q}$ pair often evolves during its virtualization , emitting gluon radiation that often transforms the bare q $\overline{\text{q}}$ pair into a meson. Discussion of this follows in more detail as the Vector Meson Dominance model (VDM or VMD) for the photon.

1.1.2 Classes of Photoproduction

Schuler and Sjorstrand[1] describe the various models of photoproduction. In the **direct process** the photon interacting in a pointlike manner with a quark from the nucleon. In the **resolved process** the photon splits into a **bare** q $\overline{\text{q}}$ with **no** gluon exchange between the quarks. The **Vector Meson Dominance** model describes the process in which the q $\overline{\text{q}}$ pair do exchange gluons between themselves, softening the distribution function of the original q $\overline{\text{q}}$ pair, and allowing the pair to evolve into a meson. Of course the meson that evolves must share the same quantum numbers as a photon; the low-mass mesons that best match the quantum state of the photon are the ρ^0, the ω, and the ϕ.

Sjorstrand[1] parameterizes the photon as:

$$\mid \gamma >= \sqrt{Z_3} \mid \gamma_{direct} > + \sum_{V=\rho^0,\omega,\phi} \frac{e}{f_v} \mid V > + \frac{e}{f_{\text{q}\overline{\text{q}}}} \mid \text{q}\overline{\text{q}} > \tag{1}$$

where

$$Z_3 = 1 - \sum_{V=\rho^0,\omega,\phi} \frac{e^2}{f_v^2} - \frac{e^2}{f_{\text{q}\overline{\text{q}}}^2} \tag{2}$$

is used for normalization. The parameter $\frac{e^2}{f_v^2}$ which appears in Equation (1) has been measured in various experiments. It is the relative coupling strength for a photon evolving into a given meson. Similarly, the parameter $\frac{e}{f_{\text{q}\overline{\text{q}}}}$ that appears in Equation (1) is the coupling strength for a photon splitting into a q$\overline{\text{q}}$ pair.

1.1.3 The Vector Meson Dominance Model

While the VMD plausibly describes photoproduction at low $p_\perp$, its predictive power fails with higher $p_\perp$. It is useful as a model of photoproduction below a $p_\perp$ cutoff of ≈ 0.5 GeV/c. Theorists originally developed the Vector Meson Dominance (VMD) model as an attempt to explain all aspects of photoproduction. Later experimental measurements at high-$p_\perp$ limited the validity of VMD. It is now used as a complement to the resolved and direct models. In VMD, the photon is paramaterized as a hadron. The pointlike photon makes no contribution to photoproduction in this model[1]. Figure(1) shows a

ρ^0	ω	ϕ
.0034	.00031	.0004

Table 1: Photon-meson coupling factors in the VMD model

diagram of the VMD contribution to photoproduction. Results from the high-$p_\perp$ photoproduction experiments show that the VMD model does not explain the contribution to the photoproduction cross-section[1]. The VMD contribution to the photoproduction cross-section falls off sharply as $p_\perp$ increases above ≈ 2.0 GeV/c. As previously discussed, the VMD model only contains the low-mass vector mesons that have strongly-overlapping quantum states with the photon. Table (1) lists these probabilities for the strongest-coupling mesons.

The value $\frac{1}{210}$, which is the ratio of $\frac{\sigma(\gamma p)}{\sigma(\pi p)}$ is commonly used for the conversion probability integrated over all mesons. VMD is considered to be phenomenologically valid for photoproduction $p_\perp < 0.5$ GeV/c. At this energy scale, the q $\overline{\text{q}}$ pair from the resolved photon has time (via the Heisenberg Uncertainty Priciple) to evolve into a full vector meson. VMD is the only model available at low $p_\perp$ since the direct and resolved contributions are based on perturbative QCD (pQCD), which fails as $p_\perp < 1.0$ GeV/c and $\alpha_s \rightarrow 1.0$. Thus the VMD model contributes to a general photoproduction process, predominantly at low $p_\perp$, instead of serving as a comprehensive model for photoproduction.

1.1.4 The Direct Photon Model

The direct photon contribution to photoproduction results from the interaction of a pointlike photon with a parton inside a nucleon. The photon imparts the entirety of its momentum in an interaction with one of the valence or sea quarks in the nucleon. The leading direct photon processes are shown in figure (2). Figure (2)(a) shows the photon-gluon fusion process; the photon interacts in a pointlike manner with a sea quark produced when a gluon from the nucleon virtualizes into a q $\overline{\text{q}}$ pair. Both the struck sea quark and the antiquark then hadronize into jets. Figure (2)(b) shows the QCD Compton process, where the photon interacts in a pointlike manner with a quark from the nucleon. This quark then emits a gluon which hadronizes into a jet, balanced in $p_\perp$

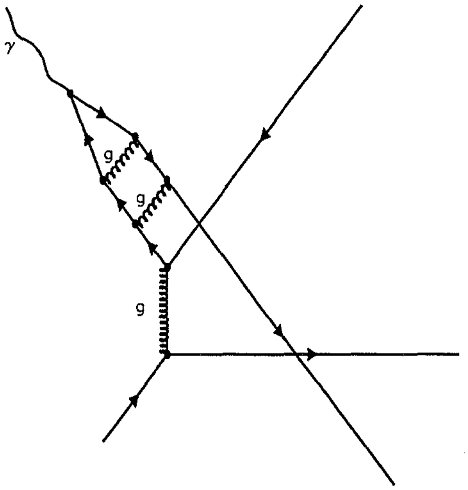

Figure 1: VMD Feynman diagram: note that the q $\overline{\text{q}}$ pair exchanges gluons in its evolution to a meson

by the jet resulting from the hadronization of the recoiling quark. The hadronization of the remaining two quarks in the nucleon forms a third 'target' jet. The distinctive experimental signature of all direct events is the lack of a 'beam' jet. This is because the photon interacts in its entirety with the quarks from the nucleon, instead of having a substantial portion of the beam particle travel without interacting.

1.1.5 The Resolved Photon Model

The third term in Equation 1 parameterizes the resolved processes. In these processes, the photon splits into a **bare** q $\overline{\text{q}}$ pair as opposed to the VMD evolved meson. The q $\overline{\text{q}}$ pair are so highly virtual as to lack the time necessary to evolve into a true vector meson. This high virtualization permits a substantially higher $p_\perp$ than the VMD processes; thus the resolved photon predominates over VMD at higher $p_\perp$. Figure (3) shows a diagram of a typical resolved photon interaction. As in other composite particles, the resolved photon has a non-interacting remnant 'beam' jet. As with the direct processes, the resolved processes are inherently calculable via pQCD. Because pQCD fails for $p_\perp \ll$

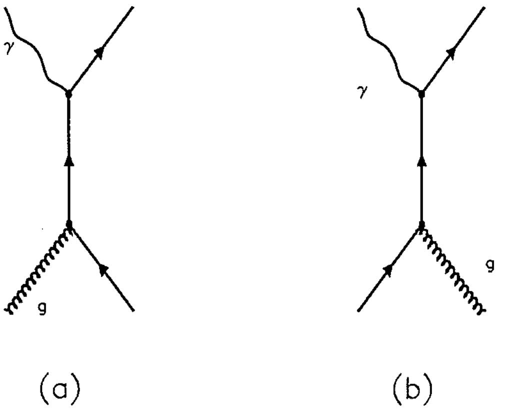

Figure 2: Direct photon Feynman diagrams: (a) is γ-g fusion; (b) is QCD Compton

1.0 GeV/c, the resolved contribution is restricted to $p_\perp$ greater than that cutoff. This threshold, however, is an **artifice**; it should **not** be thought of as a cutoff inherent in the physics of the processes, since the resolved model naturally evolves into the VMD model with the additional gluon evolution. Rather, this cutoff was imposed by the inherent limitations of pQCD calculations. One should think of the resolved model evolving naturally into the VMD model as $\alpha_s \rightarrow 1.0$.

1.1.6 Next to Leading Order Contributions

The distinction between the direct and resolved photon contributions becomes blurred as one moves from leading-order to next-to-leading-order (NLO) diagrams. The NLO diagrams contain an additional factor of α_s via the additional vertex in the diagrams. Jeff Owens[2] has noted that all photoproduction Monte Carlos presently used, such as LUCIFER, TWISTER, PYTHIA, and HERWIG, currently only account for the **leading-order** diagrams in their calculations of the photoproduction cross-section. These yield an **artificially clear** distinction between direct and resolved processes. Figure (4) illustrates how a NLO direct diagram is topologically (and experimentally) indistinguishable

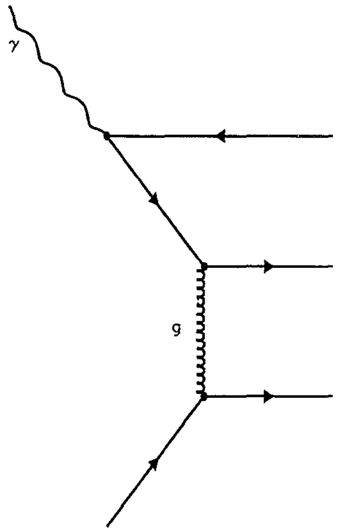

Figure 3: Resolved Feynman diagram: the q $\overline{\text{q}}$ pair do **not** exchange gluons before interaction with the parton from the incoming nucleon

from a LO resolved diagram. Furthermore, NLO calculations contribute measurably to the photoproduction cross-section, and evidently, its $p_\perp$ spectrum.

1.2 Higher Twist

1.2.1 Definition and Characteristics of Higher Twist

To quote Jeff Owens[2]:

> The term **higher-twist** refers to a property of operators which appear in the Operator Product Expansion which was used in the early '70's as a means of calculating **higher order** corrections to deep-inelastic scattering. Basically, "twist" is the dimension of the operator minus its spin.
>
> **Lower twist** give the **leading contributions in** q^2 while terms of "**higher twist**" give **power suppressed corrections**

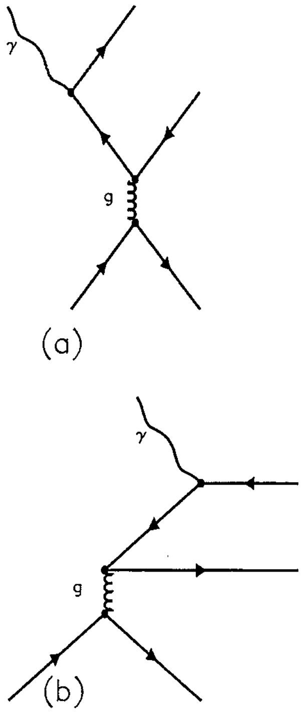

Figure 4: Diagram (a) is first order resolved: photon splits into q $\overline{q}$ pair and q exchanges g with the incoming q from the proton. Diagram (b) is second-order direct: proton q emits g that splits into a q $\overline{q}$ pair, incoming photon interacts with the $\overline{q}$. They are topologically indistinguishable.

> ... the basic idea of power suppressed corrections survives.
> For high $p_\perp$ scattering, the **least suppressed** terms
> are called **leading twist**, while **terms suppressed by**
> **higher powers of $p_\perp$ are called higher twist**
> ...
> (emphasis added).

1.2.2 Comparison between Higher-Twist and Minimum-Twist Processes

Figure (5) contains the Feynman diagrams for one possible higher-twist photoproduction. Diagrams (a) and (b) represent the direct-photon contribution to higher-twist photoproduction: the gluon emited by the quark struck converts into a q $\overline{\text{q}}$ pair. In higher-twist, this pair becomes a real pair, and then evolves into a **single** prompt meson, **without** further hadronization into a jet of particles (of course the prompt meson could decay but that is a physically distinct process from hadronization into a jet). Diagrams (c) (d) in the figure show the resolved-photon contribution to photoproduction of higher-twist: the $\overline{\text{q}}$ from the resolved photon interacts with a quark from the incoming nucleon in such a way as to form a prompt meson, balancing a jet formed by the hadronization of the beam remnant quark in $p_\perp$. The signature in both cases is similar–a prompt meson or its highly-collimated decay products balances a normal $p_\perp$ jet. Figure (6) shows the minimum-twist background to the higher-twist process. These consist of a direct photon interacting with an incoming quark from a nucleon in such a way as to form a single meson. This occasionally happens during the hadronization process; the quark-meson fragmentation function parameterizes these occurrences [3].

Bagger and Gunnion[3] have delineated the characteristics distinguishing higher-twist and minimum-twist photoproduction:

- a statistical dominance of higher-twist over minimum-twist processes at high $x_\perp$ ($x_\perp \equiv \frac{2p_\perp}{\sqrt{s}}$). As $x_\perp \rightarrow 1.0$: for minimum-twist, the greater multiplicity of the event correlates to a smaller allowance for the $p_\perp$ to be concentrated in a single particle. Due to the limited high $x_\perp$ statistics in E683, the $x_\perp$ dependence cannot be exploited effectively.

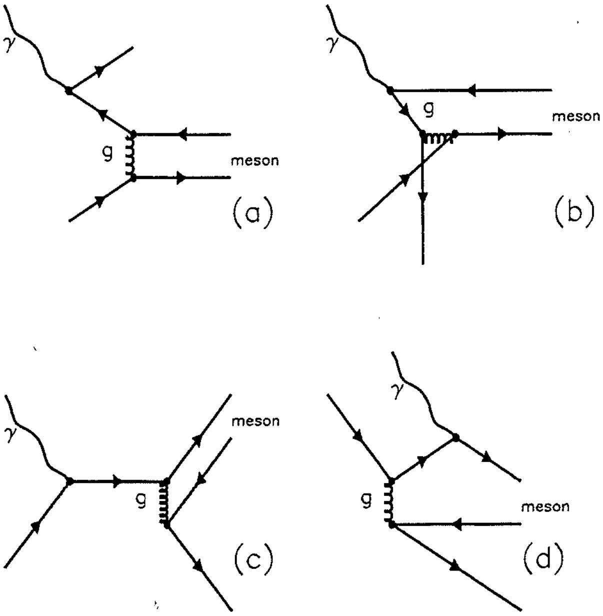

Figure 5: Higher Twist Feynman diagrams: (a), (b) are from resolved photons, (c), (d) are from direct photons

- a **relative** enhancement of higher-twist over minimum-twist as $p_\perp$ decreases, due to the extra power of α_s in the higher-twist processes. This is the obverse of the statements describing the power-suppression in $p_\perp$ earlier. As $p_\perp$ decreases, $\alpha_s \rightarrow 1.0$, and the suppression of the contributions of the higher-order diagrams due to multiple powers of α_s disappears, which explains why VMD predominates at low $p_\perp$ as well. Unfortunately, exactly where the suppression disappears, pQCD loses its validity! Due to the constraints imposed the data by the E683 trigger, $p_\perp \geq 2.0$ GeV/c forms the effective minimum for the spectral range. The power-suppression of higher-twist processes constrains the higher-twist **unsmeared** $p_\perp$ spectrum to fall off as $p_\perp^{-6}$ as opposed to the $p_\perp^{-4}$ minimum-twist $p_\perp$ falloff. The unsmeared spectrum is simply the $p_\perp$ before the resolution effects of the calorimeter smear the $p_\perp$ measurement. Even with calorimeter resolution, the higher-twist signal falls measurably faster (see Chapter 3). This relative falloff forms the basis of the cuurent attempts to observe a higher-twist signal.

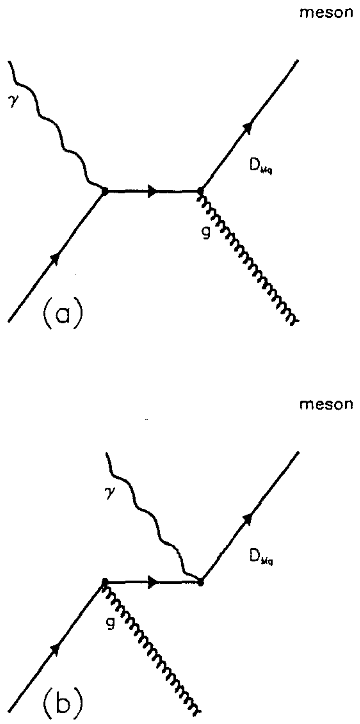

Figure 6: Dominant Minimum Twist Background Feynman diagrams (a) and (b) There are others as well, including gluons fragmenting into single mesons (D_{Mg})

1.3 Monte Carlos for Higher-Twist and Minimum-Twist

Ingelman has written two programs that are used extensively throughout this analysis: TWISTER[4] and LUCIFER[5]. TWISTER simulates all leading-order resolved photoproduction processes, and LUCIFER simulates all leading-order direct photoproduction processes. The main theoretical uncertainties associated with the higher-twist cross- section calculation in TWISTER and LUCIFER are the information on the q $\overline{\text{q}}$ and various meson wavefunctions at the origin of the interaction; this is related to uncertainties in the meson form factor [4]. In TWISTER, Ingelman uses educated guesses for the meson decay constants based on previously measured ones. He estimates the theoretical uncertainty in the normalization of the higher-twist cross-sections to be roughly a factor of two for mesons which have well-known decay constants. These mesons comprise the majority of the cross-section[4]. These simulations suggest that the higher-twist portion of our $p_\perp$ spectrum comprise $\approx$ 8.5% of the events recorded by E683. The direct process has a larger fraction of higher-twist events than the resolved process, but there is a smaller total direct cross-section.

LUCIFER models the following processes:

- **QED Compton** $\gamma + q \rightarrow \gamma + q$
- **QCD Compton** $\gamma + q \rightarrow g + q$
- **Photon-Gluon Fusion** $\gamma + g \rightarrow q + \overline{q}$
- **VDM interactions** modelling the photon as a ρ^0

TWISTER models the following:

leading-order resolved α_s^2:

- $q + q \rightarrow q + q$
- $q + \overline{q} \rightarrow q + \overline{q}$
- $q + \overline{q} \rightarrow g + g$
- $q + g \rightarrow q + g$
- $g + g \rightarrow q + \overline{q}$
- $g + g \rightarrow g + g$

direct photon emission:

- $q + \overline{q} \rightarrow \gamma + g$
- $q + g \rightarrow \gamma + q$
- $q + \overline{q} \rightarrow \gamma + \gamma$
- $g + g \rightarrow \gamma + \gamma$

higher-twist α_s^3:

- $q + \overline{q} \rightarrow g + M$ (M: meson)
- $q + g \rightarrow q' + M$
- $g + g \rightarrow g + M$

higher-twist $\alpha_s^2\alpha_{EM}$:

- $q + \overline{q} \rightarrow \gamma + M$
- **VDM interactions** modelling the photon as a ρ^0

Both Monte Carlos share a relatively common interface. The user has the ability to specify the number of events, the seed for random number generation, etc. In TWISTER and LUCIFER, the user has the choice of Monte Carloing the full set of resolved photoproduction processes, or any subset, including only higher-twist events, or only minimum-twist events. When the user specifies the full set of resolved processes, the Monte Carlo designates a flag that informs the user what subprocess was generated in a given event. The user has the choice of target (in this analysis, the target is always a proton), and the beam particle (always a photon). For TWISTER one can specify the distribution function for the photon. Since TWISTER uses resolved photons, the distribution function is relevant parameter, as it specifies the fraction of photon energy the interacting quark in the photon carries. TWISTER and LUCIFER also allow the user to specify the choice of proton distribution functions. The range of energies probed by E683 limit the data to relatively high values of fractional momentum. This is where the distribution functions are best known, so the calculation is relatively insensitive to the given distribution function.

The Monte Carlo also allows one to specify the choice of $q_{\perp_{min}}$: the perpendicular component of the momentum transfer between two partons, which specifies the minimum $q_\perp$ generated by any event in the Monte Carlo. Since the Monte Carlos are based on pQCD, an event with a momentum transfer less than a given energy would cause the α in the event to approach 1, and the event would become non-perturbative. Furthermore, if the experimental trigger is such that a significant region of momentum transfer is excluded from the trigger, by specifying a higher value of $q_{\perp_{min}}$, one can avoid simulating unneccessary events.

TWISTER and LUCIFER also allow the user to specify $k_\perp$. $k_\perp$ is the internal momentum transfer between the quarks in the target proton (or incoming photon for resolved photons). The importance of $k_\perp$ will be discussed in the Chapter 3. Briefly, $k_\perp$ via internal gluon exchange results in a significantly unbalanced momentum distribution in the q-$\overline{\text{q}}$ pair in the photon. This leads to a significantly altered $p_\perp$ measurement from what one would expect.

Finally, TWISTER and LUCIFER allow the choice of **fragmentation** (also called hadronization). Fragmentation is simply the process where the bare exiting quark (which cannot be observed under QCD) evolves into the particles and jets observable in the experiment. E683 uses the terms **naive** for the bare quark and the kinematic variables (θ, ϕ, $p_\perp$), and **post-virtual** for the kinematic variables attached to the post-fragmentation products of the naive quark.

There are three choices for the fragmentation process:

- **String fragmentation** is a popular model in e-$\overline{\text{e}}$ physics. The two quarks exiting the interaction are connected by a color string. As the quarks seperate from each other, the string tension increases, as well as the energy within the string. Eventually, the string snaps, with the broken ends attached to new quarks formed by the energy released as the tension on the formerly-connected string breaks. This process continues until the energy in the strings is no longer sufficient to produce more quarks. The difficulty with applying this process on E683 data is that this model does not reproduce the amount of **underlying event** sufficiently. Underlying event comprises the particles not included in the jets exiting the interaction. Energy flow plots from E683 show the string fragmentation model does not reproduce sufficently the energy distribution between the measured jets [15].

- In **cluster fragmentation**, the exiting parton has a high mass which is dissipated by emission of gluons that then form q-$\overline{\text{q}}$ pairs until the interactions energies are such that $\alpha_s \to 1$ The underlying event produced in this model is also insufficient for the underlying event between the jets as measured on E683.

- **Independent fragmentation** is the most difficult to justify theoretically, since it simply produces particles in accordance with empirical data on hadronic jets without a theoretical model, and does not explain how the naive quark evolves into a jet. However, since it is based on empirical data (especially at moderate center-of-mass energies in hadronic interactions), this model accurately reproduces the topology of the measured energy flow, including the underlying event. (**Energy flow** simply denotes the positional displacement of the energy in the interaction–since the

E683 calorimeter is granular, it measures the magnitude of energy deposited at various positions and therefore yields a position-energy correlation). Therefore, independent virturalization was the chosen fragmentation model in this analysis.

This analysis used the E683 default values for all the parameters except the $q_{\perp_{min}}$ value. The default values are:

- independent fragmentation.
- $k_\perp$ for the proton as specfied by the LUCIFER and TWISTER Monte Carlos.
- $k_\perp$ for the photon as specfied by the TWISTER Monte Carlos.
- EHLQ 1 proton structure function.
- Duke-Owens QCD photon structure function.
- Energy conservation by boosting event to COM of vector sum.
- GLOBAL trigger of 9.12 GeV.
- TWOHI trigger of 0.855 GeV.

E683 uses 2.0 GeV/c; this analysis will justify using a value of 1.0 GeV/c later.

To show the types of mesons that dominate higher-twist production, figures (7) and (8) show the relative amounts of the various mesons expected from the E683 spectrum as simulated by TWISTER and LUCIFER combined with the detector simulation. Figure (7) shows the contribution from TWISTER, and figure (8) shows the contribution from LUCIFER.

1.4 E683 and Higher Twist

E683 is primarily a calorimetry experiment. Therefore, the exploitation of the different $p_\perp$ falloff of minimum- and higher-twist events formed the basis of this analysis. The experimental layout, described in the next chapter, is optimized for the detection and measurement of high-$p_\perp$ photoproduced jets; 'high' in this case denoting a range of 2-7 GeV/c. To understand how an event appears in the calorimeter, figure (9) shows how a given higher-twist event would appear on the calorimeter face, and figure (10) shows how a given minimum-twist event would appear on the calorimeter face.

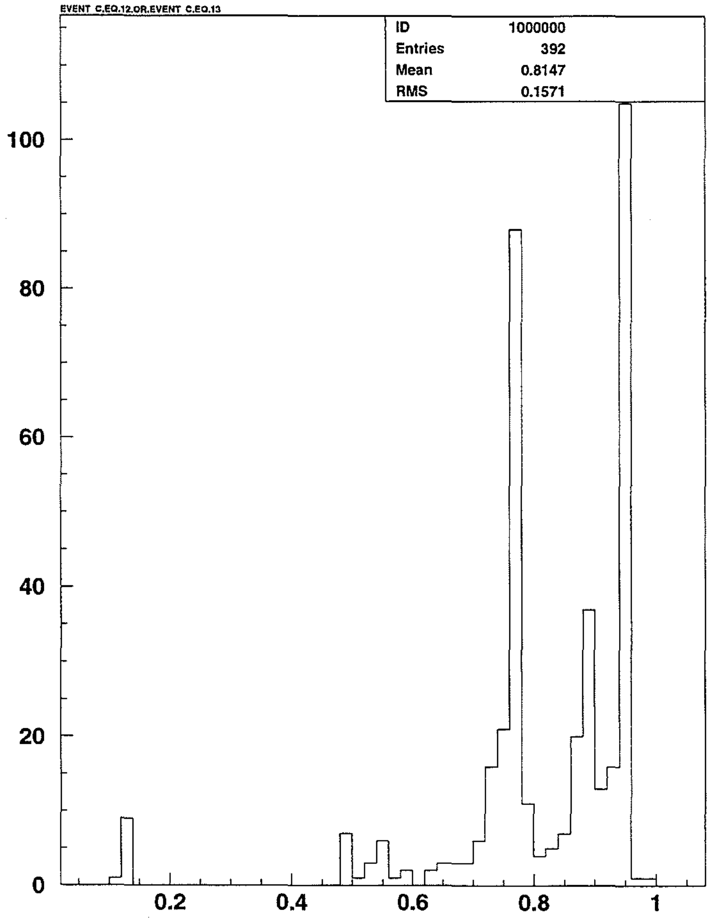

Figure 7: Monte Carlo: The mass spectrum of the initial mesons produced by higher-twist processes in resolved processes.

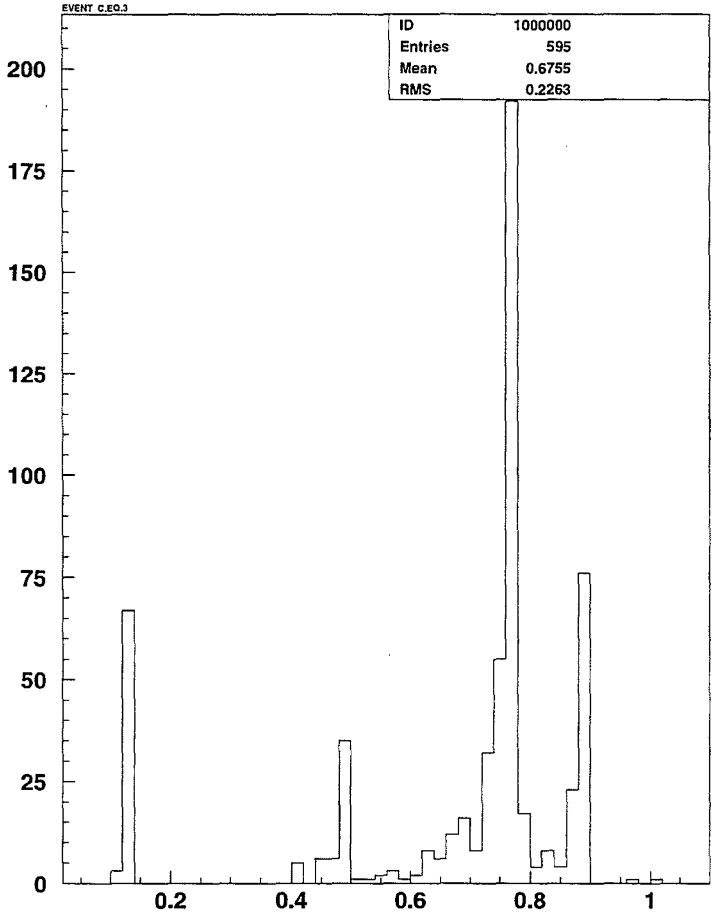

Figure 8: Monte Carlo: The mass spectrum of the initial mesons produced by higher-twist processes in direct processes.

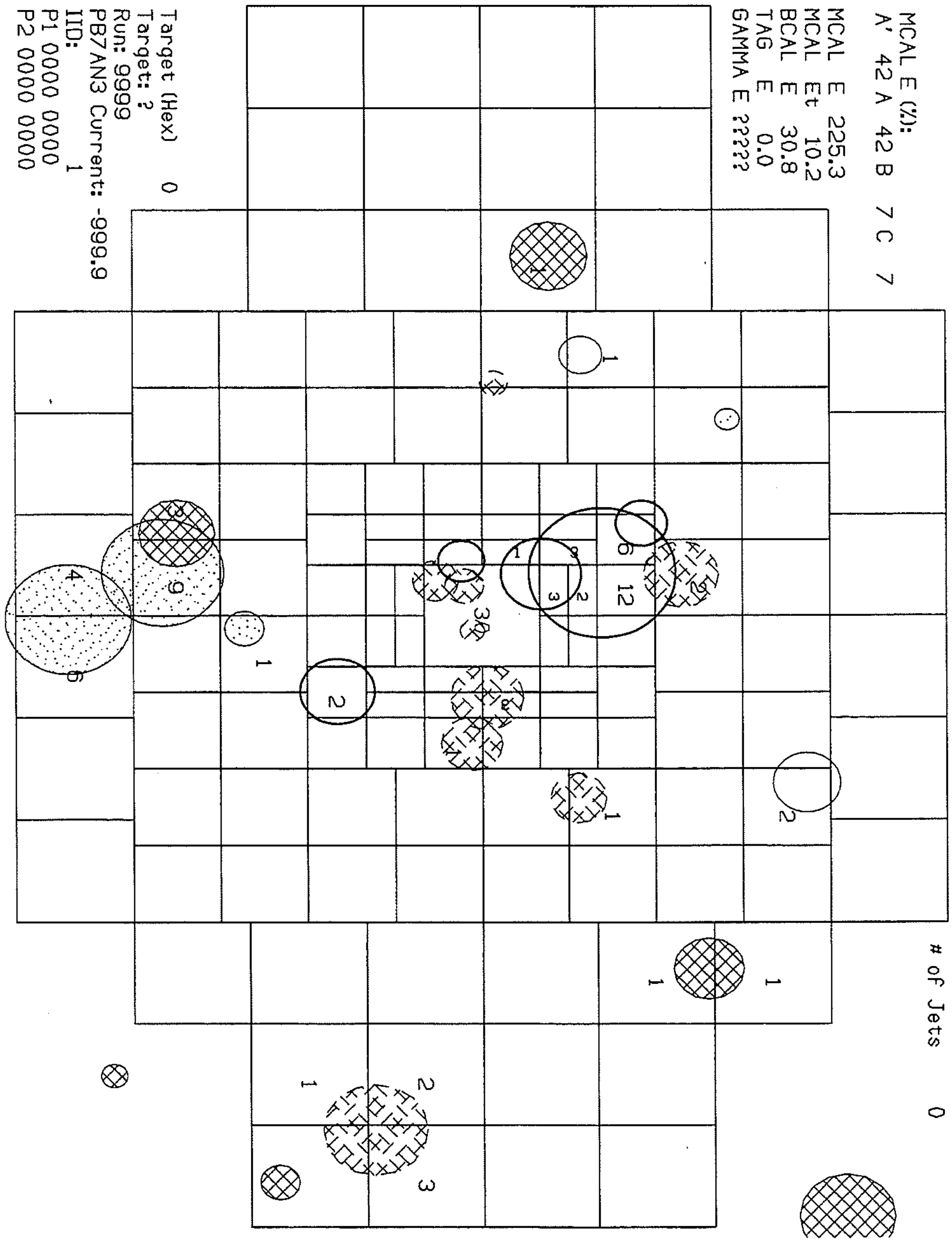

Figure 9: Monte Carlo: A typical higher-twist event displayed on the Main Calorimeter. The clear circles are particles from the prompt meson. The dotted circles are from the second exiting jet. The hatched circles are from the underlying event.

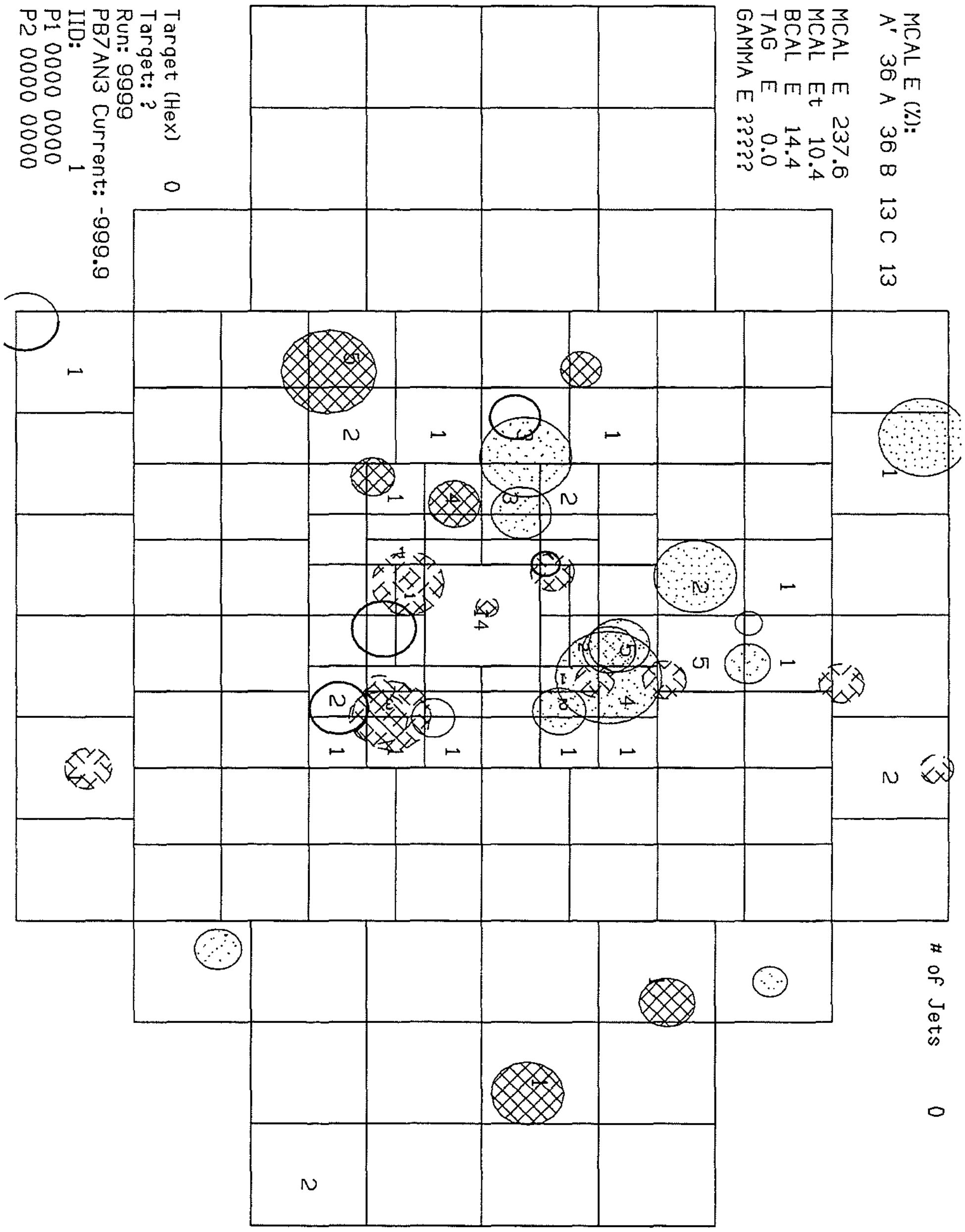

Figure 10: Monte Carlo: A typical minimum-twist event displayed on the Main Calorimeter. The clear circles are from the first jet. The dotted cirlces with dots are from the second jet. The hatched circles are from the underlying event.

Comparison of different $p_\perp$ spectra is of course is a statistical argument, in that no one event exhibits a higher-twist contribution. However, the basis of this analysis is that by exploiting topological differences between decay products of a meson vs the formation of a jet, one could make cuts based on those differences. Then one could enhance the higher-twist fraction of the ensuing $p_\perp$ spectrum. By enhancing the higher-twist contribution, the $p_\perp$ spectrum should fall more steeply. Then one could show that the $p_\perp$ spectrum is a mixture of a pure higher-twist and minimum-twist $p_\perp$ spectra, and argue in favor of the observation of a higher-twist signal.

2 Experimental Overview

2.1 Beamline Overview

Our experiment uses a tagged photon beam. The photon beam is produced via bremsstrahlung of electrons and positrons as they travel through a thin radiator. Reference [6] describes the details by which high-energy photons are produced at Fermilab. It uses a tertiary photon beam in order to minimize neutral contamination of the beamline. Figure (11) shows the beamline elements that brings photons down to our experimental area. High-energy (up to 900 GeV) protons are extracted from the Main Ring and hit a target to produce a shower of kaons, pions, protons, and neutrons. The charged particles are swept away by a bending magnet, leaving the neutral pions to decay into γ-rays, which pass through a converter (called PB4CON in the beamline)–a thin sheet of lead that provides the high-Z target needed for pair-production of electrons and positrons.

Neutral contaminant particles (the kaons and neutrons) are absorbed by the beam dump. Meanwhile the electrons and positrons are bent by dipole magnets to opposite sides, circumventing the beam dump. More magnets recombine the e and $\bar{\text{e}}$ into one beam again, which passes through a momentum-defining collimator. The dispersion of the momentum of the particles that pass through this collimator is limited to within 15% from a mean 340 GeV/c[6]. The energy of each e and $\bar{\text{e}}$ is measured via silicon detectors located on beam right and beam left. The counters have a resolution of ≈ 2 % of the electron energy.

The e and $\bar{\text{e}}$ then pass through PB6IC, an ionization counter that measures the electron (and positron) flux accurately on a spill by spill basis. This is needed to obtain an absolute flux normalizaton for our cross-section analyses. E683's readout of PB6IC also informed the experiment about the overall quality of our spills, and the readout was useful in optimizing the upstream beam tune. Finally, PB6IC informed the experiment about broken spills–spills when there was no beam delivered from the accelerator. Any events that occurred during these spills are discarded.

The e-$\bar{\text{e}}$ is focused into the thin radiator (called PB6RAD), a Pb square that varied between 0.05 X_0, 0.10 X_0, and 0.2 X_0. E683 normally used a 0.20 X_0 PB6RAD in order to optimize photon flux versus double bremsstrahlung. The e and $\bar{\text{e}}$ bremsstrahlung, and produce photons in the typical $k_\perp^{-1}$ spectrum trailing off at the maximum beamline energy of > 400 GeV/c.

The possibility of a double bremsstrahlung obviously exists, and this would pose serious problems. For example, if two 125 GeV photons were produced, and only one interacted, E683 would erroneously measure the interaction photon energy as 250 GeV.

However two factors mitigate against this phenomenon influencing our trigger. The first factor is that two photons of comparable energy would rarely each have enough energy to trigger an event. The second factor is that one of the photons (or one of any number of soft photons) has a possibility of producing pairs that would force a veto of the event by the hardware charge veto or by the energy conservation cuts discussed later in the analysis are made. The Beamline Monte Carlo produced by the author showed that for our triggered photon spectrum, the energy of all the photons in triggered events is almost identical to the energy of the leading-energy photon.

Afterwards the recoil electrons and positrons are swept out of the beam by sweeping magnets into a recoil electron shower hodoscope or RESH (the positrons are of course swept the opposite way by the magnets into the positron shower hodoscope or POSH), which measures the energies of the recoil electrons and positrons. From the knowledge of the electron's energies before and after the bremsstrahlung process, we can determine the energy of the photon, thereby "tagging" it :

$$\mathrm{E}_\gamma = \mathrm{E}_{e_{Si}} - \mathrm{E}_{e_{resh}}. \tag{3}$$

Although the energy of an individual photon varies within the bremsstrahlung spectrum, the energy of the photon is known to within the resolutions of the Silicon and RESH detectors. This produces a tagged broad band photon spectrum–or a wide band photon spectrum.

For the 1991-1992 Fixed Target Run, the $\bar{e}$ were not included in the beamline due to baryon contamination. The problem has been circumvented for the 1996 Fixed Target Run, however.

2.2 Experimental Detectors

2.2.1 Detector Overview

From the general layout of the experiment (12), we see as we look downstream the veto hodoscope, target (either nuclear, LH_2, or LD_2), interaction counter, PWC, small wire

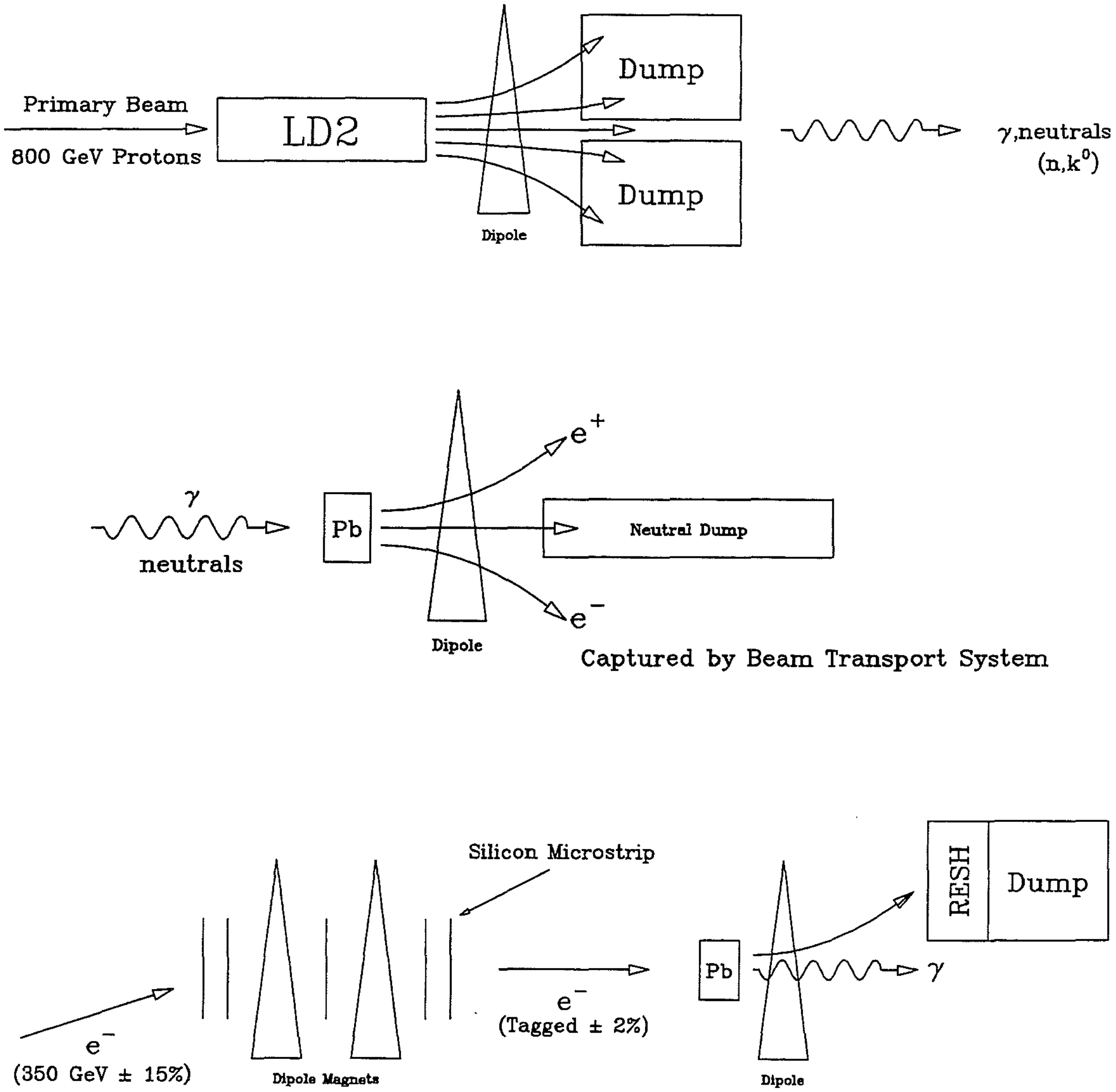

(Figure courtesy of Greg Morrow.)

Figure 11: FNAL Wide Band Beam Schematic.

C1	B1	B2	C2
.125″×9.0″×9.0″	.0625″×1.0″×1.0″	.0625″×8.0″×8.0″	.125″×4.0″×4.0″

Table 2: Physical dimensions of the E683 beam counters C1 being the most upstream, to C2 the most downstream. Note: before July 7, 1991 C1 was .0625″×9.0″×9.0″; before July 18, 1991 C2 was .25″×4.0″×4.0″

chambers, dipole magnet, large wire chambers, main calorimeter, and beam calorimeter. 6′ of battleship steel placed with an 8″×8″ square beam hole just upstream of our detectors shielded our experiment from the detritus produced by the upstream experiment, E687, running parasitically off the beamline during the run.

2.2.2 Beam Counters

E683 placed scintillators that measured the charge content of the beam and the beam position just upstream and downstream of our target. The author was in charge of the placement and maintenance of these beam counters during the run. For the sake of archival information, the physical dimensions of the counters are in table (2)[8]. C1 was the counter placed just upstream of the hadronic shielding, B1 was the beam position counter, B2 was just downstream of B1, before the target, and C2 was the charge requirement counter just downstream of the target. They are shown in figure (13).

2.2.3 Muon Veto Counters–the Hodoscope

A muon veto counter/hodoscope lay just downstream of the hadronic shielding and just upstream of the target. The author was responsible for the design, maintenance, and construction of the hodoscope, as well as its integration into the general E683 trigger setup.[9] (The author produced and distributed sketches of the MAIN, GAMMA, PAIR, BEAM, MUON, PEDESTAL, BCAL, and RESH triggers in an internal note.[10]) The hodoscope served two purposes:

- For a first-order calibration of Main Calorimeter voltages. There was a rough correspondence between an x-y coincidence of the hodoscope and groups of towers in the Main Calorimeter. The muon signal from the hodoscope would coincide with

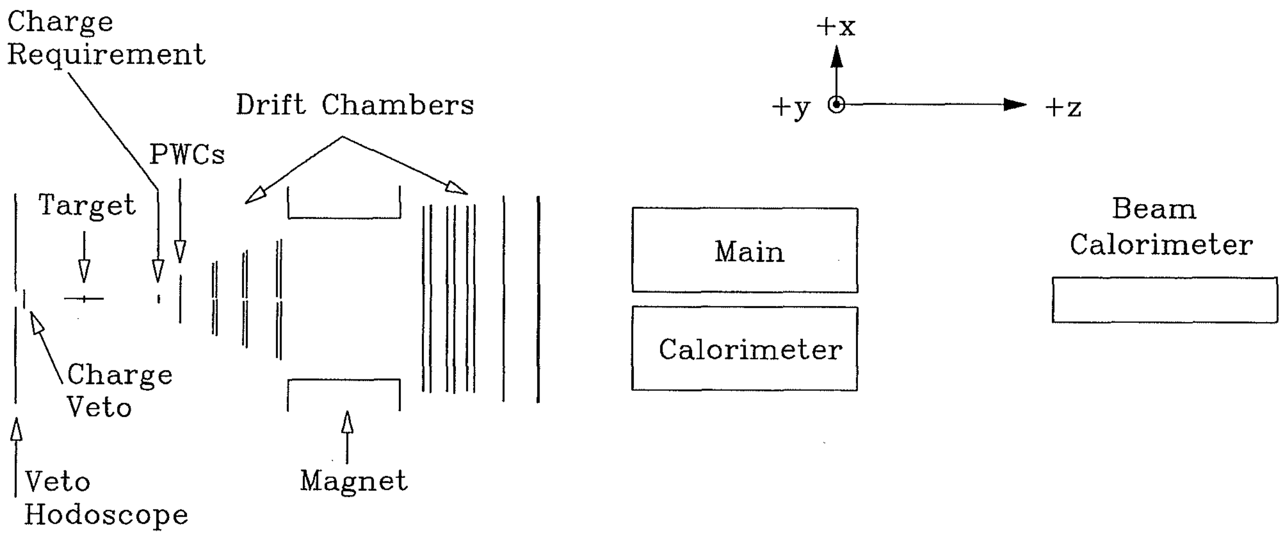

Figure 12: General layout of E683. From midpoint of target to face of Main Calorimeter is 300″.

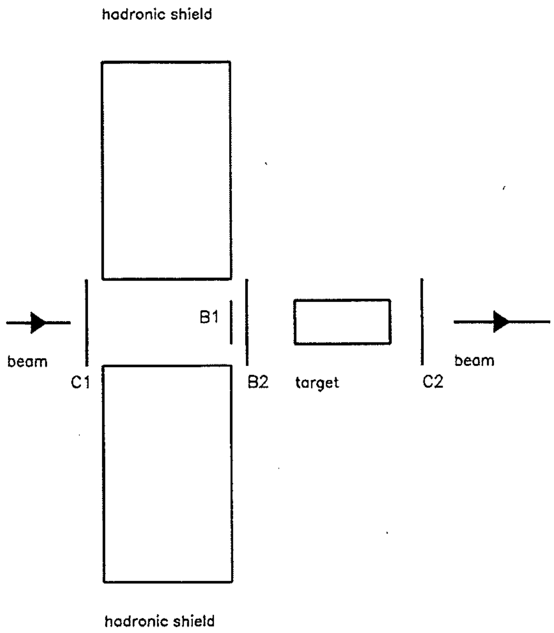

Figure 13: Closeup of figure (12) showing location of B1, B2, C1, C2

ADC signals from a group of four modules from a calorimeter tower. Using the signals from a muon run, E683 adjusted the voltages to equilibrate the signals from each module.

- For a second-order measurement of chamber wire position (the first-order measurement being the physical survey of the chamber position). Again, a muon hit would give rough x-y information on the location of the muon.

- Vetoing excess muon events. The author previously explained[9] how muons would occasionally deposit excessive energy in one or two towers of the calorimeter, deceiving our GLOBAL or TWOHI triggers into triggering. Since the muons would deposit energy in a highly-unbalanced manner in the calorimeter, offline examination of the events would (and did) by requiring a balance in energy in the calorimeter, effectively remove these spurious triggers. However, the muons could overwhelm our data stream. The hodoscope dramatically reduced these spurious hardware triggers.

Target	A, g/mol	t, cm	X_0, cm	ρ, g/cm^3
LH$_2$	1.01	50.8	865	0.0708
LD$_2$	2.01	50.8	757	0.162
Be	9.01	2.54	35.3	1.848
C	12.01	2.54	18.8	1.72
Al	26.98	2.07	8.9	2.7
Cu	63.55	0.612	1.43	8.96
Sn	118.69	0.504	1.21	7.31
Pb I	207.19	0.368	0.56	11.35
Pb II	207.19	0.127	0.56	11.35

Table 3: Atomic masses (A), thicknesses (t), radiation lengths (X_0), and densities (ρ)

The hodoscope effectively covered the face of the calorimeter. The vertical plane was 78″top to bottom, and the horizontal plane was 140″east to west, with an 6″by 6″ square hole centered on the beam. For comparison the calorimeter C-layer (the largest layer of the calorimeter) stretched 90″from top to bottom, and 115″east to west, with an 8″by 8″hole centered on the beamline[11]

2.2.4 Targets

The target consists of a cylinder filled with liquid hydrogen for our main studies, and a rotating wheel of targets of various atomic number for our A-dependence studies. This analysis is concerned solely with liquid hydrogen, however in the interest of archiving relevant experimental information, the dimensions and radiation lengths all targets used are in table (3):[12]

2.2.5 E683 Magnet

The E683 magnet was a weak dipole magnet that yielded a slight $p_\perp$ kick to the charged particles leaving the event. John Marraffino[13], has provided the relevant information on the magnet on E683 (no magnet or chamber data was used in this analysis). The magnet was referred to as PB7AN3 in the beamline nomenclature.

- x-aparature size (centered on the beam axis): 84″
- y-aparature size (centered on the beam axis): 40″

- z-aparature size (centered on the beam axis): 59″
- current draw: 800 Amperes
- $p_\perp$ kick: 0.072 GeV/c
- charge resolution limit (at the 3σ confidence level): 170 GeV/c

2.2.6 Wire Chambers

The wire chambers and magnet were meant to form a spectrometer on E683. The spectrometer did not constitute a relevant part of this analysis. However, for archival purposes, Greg Morrow has provided me with the information in Appendix A [7].

The tracking algorithm is in the final stages of completion at the time of writing. Due to the weak $p_\perp$ kick of the magnet and the low efficiency of the y-position measurement of the upstream chambers, the tracker's effectiveness is limited to verticing an event to determine whether the interaction occurred within the target region or otherwise. No charge, multiplicity, or momentum measurements for particles in an event were used in this analysis.

2.2.7 Beam Calorimeter

The beam calorimeter (BCAL) has been exhaustively described elsewhere[14][15]. Its design purpose was to measure the energy of the beam jet (for resolved and VDM events) and the spectator jet. In practice, the geometry of the events precluded the separation of the energy from the spectator jet and the event jets, as the spectator jet energy flow usually entered the part of the main calorimeter (MCAL) as well. Essentially, the BCAL served to measure any energy flow boosted forward enough to travel through the beam hole in the main calorimeter. In this analysis the BCAL served solely to impose an energy conservation requirement on the event ($[E_{BCAL}+E_{MCAL}]-[E_{Si}-E_{RESH}] \approx 0$), as the clustering algorithm described in Chapter 3 imposed a fiducial cut precluding the contribution of any event energy in the BCAL.

The BCAL physically consisted of a Fe-scintillator sandwich $2' \times 2'$ centered on the beamline, more than covering the beamhole of the MCAL[14]. The light was mixed from various scintillator combinations upstream and downstream into eight phototubes.

(There were also some wire chambers that were essentially extraneous).

The BCAL resolution has been cited[15] as:

Electromagnetic:

$$\frac{\sigma(E)}{E} = \frac{45\%}{\sqrt{E}} \tag{4}$$

Hadronic:

$$\frac{\sigma(E)}{E} = \frac{75\%}{\sqrt{E}} \oplus 4.6\% \tag{5}$$

where the Energy is measured in GeV/c.

2.2.8 Main Calorimeter

The main calorimeter (MCAL) has also been described in wonderfully precise detail.[16][7] The author has no intention of reproducing unnecessary detail here, but to remind the reader of facets of the MCAL relevant to the analysis.

The MCAL consists of 132 modules, with a phototube attached to each module, in each of four **layers**, **A′**, **A**, **B**, **C**, for a total of 528 modules. (see figures (15), (14)). A′ was optimized for the measurement of the electromagnetic component of the energy, and A, B, C for the hadronic component. The corresponding module from all four layers composes a **tower** (16) of the module (eg: A′1+A1+B1+C1 is tower 1).

Figure (14) shows the face of the calorimeter. If one counts outwards from the beamhole in the middle, one will traverse eight modules going towards beam left or right, and six modules going towards beam up or down. As one traverses the modules, calling the innermost module module one and the outermost module module eight, the radiation and absorption lengths are presented in table (4) for A′, (5) for A, B, and C [16].

The MCAL was ≈ 300″ from the center of the target. The fiducial acceptance of the MCAL is a function of the energy of the event, but a reasonable value for the acceptance

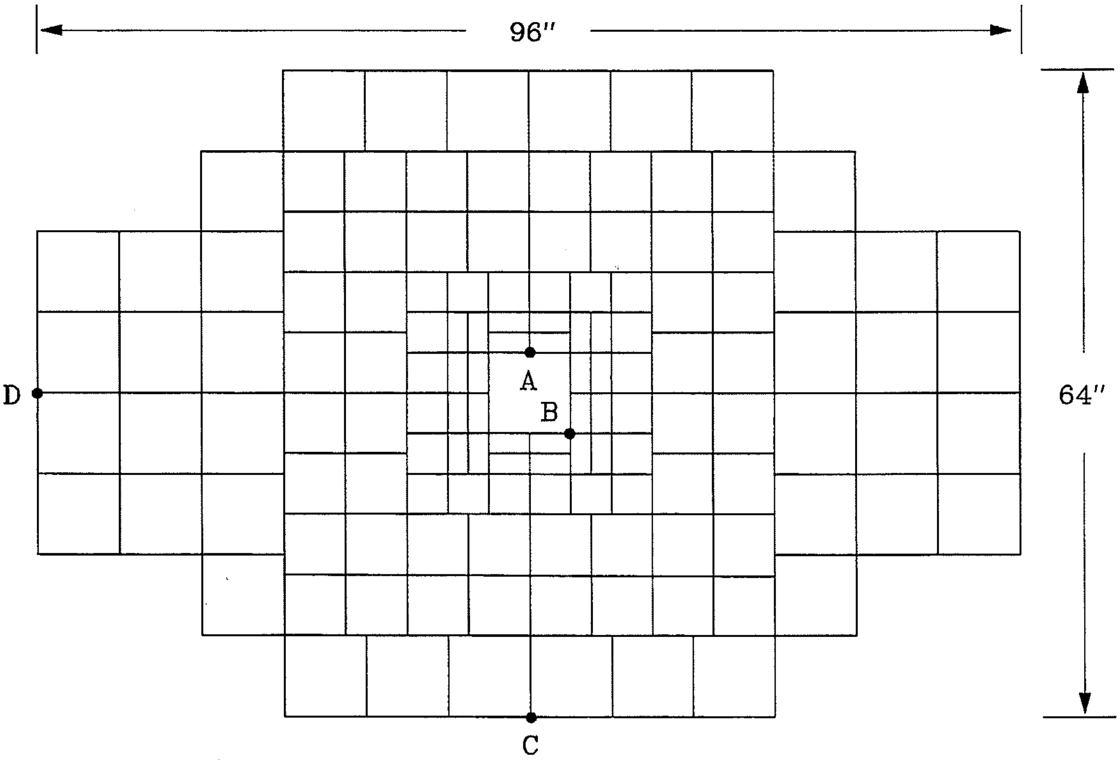

Figure 14: Depiction of the 132 segments of each calorimeter layer. The points A, B, C, and D have no special significance in this context.

module	size	X_{rad}	X_{abs}
one	$2'' \times 4''$	8.8	0.37
two	$2'' \times 4''$	8.8	0.37
three	$4'' \times 4''$	8.8	0.37
four	$6'' \times 6''$	5.37	0.24
five	$6'' \times 6''$	5.37	0.24
six	$8'' \times 8''$	5.37	0.24
seven	$8'' \times 8''$	5.37	0.24
eight	$8'' \times 8''$	5.37	0.24

Table 4: Size, radiation length, and absorption length for the A$'$ layer modules.

is $40^o \leq \theta^* \leq 100^o$, where θ^* denotes the angle from the beam axis (with the interaction point as the vertex) in the COM frame of the event.

The final resolution of the calorimeter is[7]:

Electromagnetic:

$$\frac{\sigma(E)}{E} = \frac{39\%}{\sqrt{E}} \oplus 1.8\% \tag{6}$$

Hadronic:

$$\frac{\sigma(E)}{E} = \frac{70\%}{\sqrt{E}} \oplus 6.0\% \tag{7}$$

with the $\frac{e}{h}$ ratio being 1.26.

2.2.9 Main Calorimeter Electronics

The Main Calorimeter Electronics are shown in figure (17). The output of the phototubes from each module is fed in to a calorimeter amplifier (or calamp for short). Every module signal was amplified by a factor of five for our run (or by twenty for calibration with muons). The signals then travelled from the detector area into the counting room, where each signal entered a summing and weighting module. A passthrough from the summing and weighting module continued the amplified signal from each module

module	size	X_{rad}	X_{abs}
one	$2'' \times 4''$	23.08	2.54
two	$2'' \times 4''$	23.08	2.54
three	$4'' \times 4''$	23.08	2.54
four	$6'' \times 6''$	17.89	2.11
five	$6'' \times 6''$	17.89	2.11
six	$8'' \times 8''$	15.35	1.93
seven	$8'' \times 8''$	15.35	1.93
eight	$8'' \times 8''$	15.35	1.93

Table 5: Size, radiation length, and absorption length for the A, B, and C layer modules.

into ADCs, where the signals were digitized. For triggering, the summing and weighting modules summed the signal from each module in a tower (weighting the electromagnetic and hadronic layers differently to compensate for different responses to energy deposition), and then the **tower's** signal is sent to the sinθ attenuators. The sinθ attenuators compensated for the different angles covered by different towers so that the GLOBAL and TWOHI trigger electronics receive a signal corresponding to the $E_\perp$ of the tower. The GLOBAL and TWOHI triggers then fed into the gamma trigger such that if the aformentioned minimum GLOBAL or TWOHI signals were observed, the event would be logged onto tape. (There was also a trigger matrix that triggered on various tower topologies–it was not used in this analysis).

2.3 Trigger

The tower scheme of the MCAL is relevant due to its contribution to our event trigger for photons.

The **GAMMA** trigger was comprised of the following conditions:

- No charge in counters C1 or B2, the counters upstream of the target. This veto precluded pairs produced by material upstream of the target along the beam axis (recall that E687 was upstream of our target consisting of a total radiation length of $\approx 0.22\ X_o$).
  and
- Charge in counter C2, just downstream of the target. This informed the trigger

that an event happened.
and

- No charge traversing the veto hodoscope.
  and

- The computer was not processing another trigger (i.e., the **BUSY** veto).

Our event trigger consisted of the following physical occurrences:

- GAMMA trigger **and**

- The computer was able to accept a trigger (i.e., it was not processing a previous trigger). This prevented one trigger interfering with another during the computer deadtime
  and either of the following:

- $\geq \approx 6.8$ GeV/c deposited in all of the MCAL (this is called the GLOBAL trigger)
  or

- $\geq \approx 0.86$ GeV/c deposited in each of at least two towers of the MCAL (this is called the TWOHI trigger)

When the main trigger was processing data, a 10 ms signal was generated representing the computer processing the data (the **BUSY** veto). During that time the BCAL and other devices was still able to read out energy, although their readouts could not effect the trigger logic. In order to effectively measure computer deadtime, the BCAL triggers for various energy thresholds were sent to parallel scalers for each spill: one scaler denoted all BCAL triggers over an energy threshold that occurred while the computer was not busy (the **gated** BCAL triggers), and the other simply accepted all BCAL triggers over an energy threshold (the ungated BCAL triggers).

In practice, in order to circumvent hardware efficiency effects (i.e., the rollover area in the global $E_{\perp}$ spectrum, the GLOBAL trigger was moved up to ≈ 9.1 GeV/c in the analysis software.

The GLOBAL and TWOHI triggers (with housekeeping cuts described later) formed the data sample for the analysis.

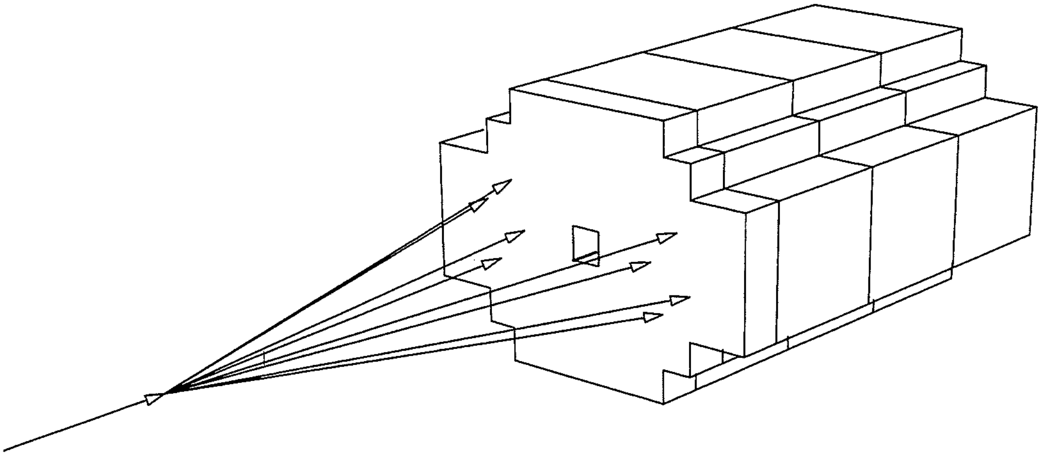

Figure 15: Three dimensional view of the MCAL in the lab frame.

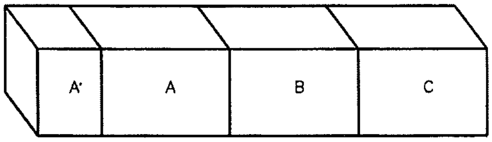

Figure 16: Depiction of a given tower in the calorimeter composed of four layers of the same numbered segment.

2.4 DAQ

Our data acquisition system consisted of a μVAX II that collected a digital datastream from CAMAC modules and passed the datastream to 6250 bpi 9 track tapes. The event rate varied according to the target, but generally ran at about 20 Hz. The master tapes are stored at FNAL Computing under the QN series. Copies of the masters are on 8 mm exabytes under the QME series 1-95.

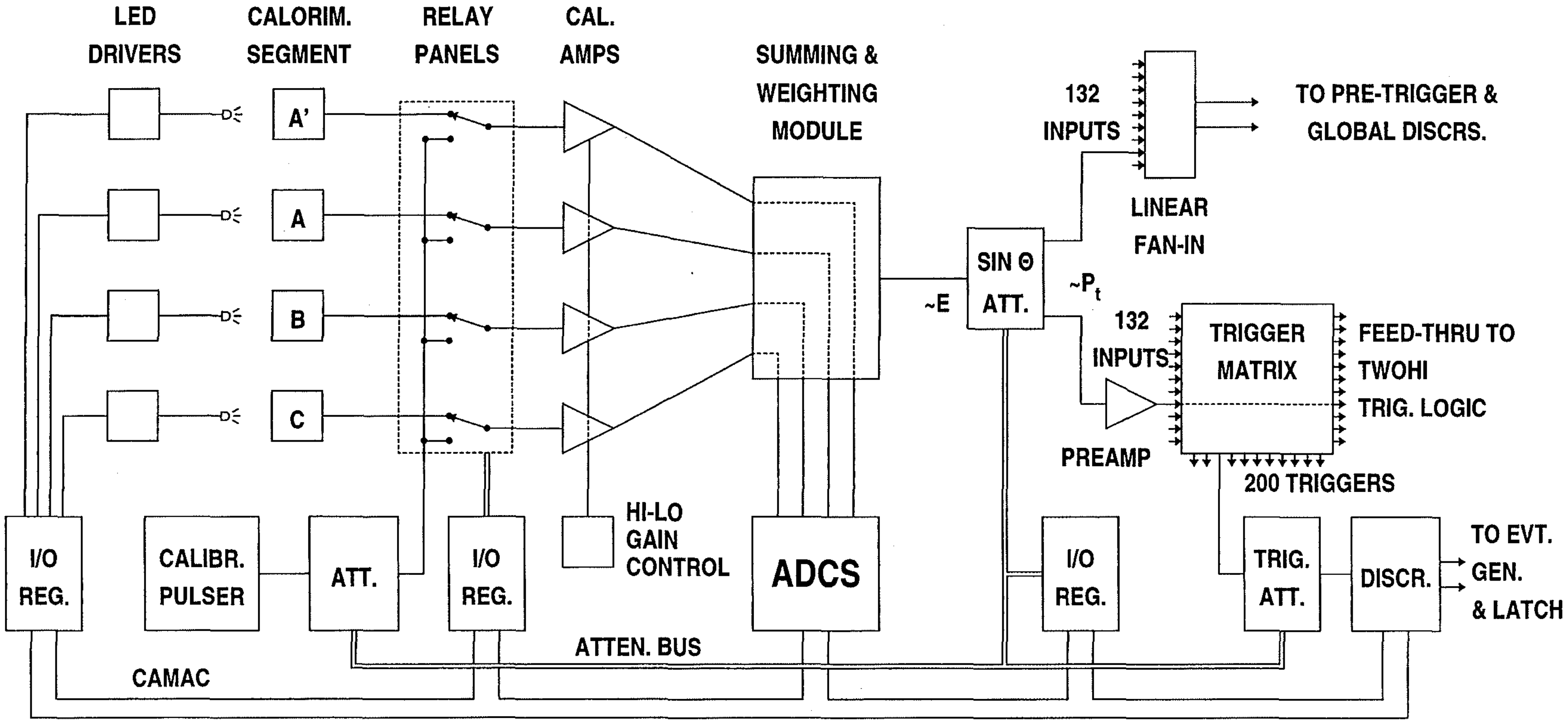

Figure 17: The Main Calorimenter triggering and signal-readout schematic.

3 Data Analysis

3.1 Overview

The argument of the present analysis' rests on one signal: the $p_\perp^{-6}$ falloff of higher-twist events vs the $p_\perp^{-4}$ falloff for minimum-twist events. Naturally, the **smearing** imposed by the calorimeter resolution will blur this distinction to some extent. Suppose that the calorimeter had a Gaussian energy resolution. For a $p_\perp^{-6}$ falloff, the smearing imposed on the $p_\perp$ spectrum due to the energy resolution would shift the spectrum outward. This is readily explainable. A Gaussian smearing applied to an ensemble of events with identical $p_\perp$ will increase the measured $p_\perp$ from its original value and decrease some others, leaving the mean unchanged. However, since the spectrum falls off with $p_\perp$, there are more events at lower $p_\perp$ than at higher $p_\perp$. Furthermore, there is a minimum $p_\perp$ of zero measured (actually, due to the trigger requirements, somewhat greater than zero), so the asymmetry of the smearing combines with the asymmetry of the distribution to shift the mean toward larger $p_\perp$ and to harden the measured $p_\perp$ dependence to a lower value, say $p_\perp^{-4.2}$. The same Gaussian smearing applied to a $p_\perp^{-4}$, spectrum will have also shift the mean out and harden its spectrum, but since the $p_\perp^{-4}$ spectrum has a lower asymmetry than the $p_\perp^{-6}$ spectrum (there are relatively more events at a higher $p_\perp$ in a $p_\perp^{-4}$ spectrum than a $p_\perp^{-6}$ spectrum for the same number of events), the effect will be relatively smaller for the harder $p_\perp^{-4}$ spectrum than the softer $p_\perp^{-6}$ spectrum. This in turn makes the two spectra more difficult to differentiate than would be the case for a calorimeter with perfect resolution.

However, the $p_\perp$ spectrum and the difference between the higher-twist and minimum-twist spectra still form the central result of the analysis. What one must do is somehow find a way of separating higher-twist and minimum-twist events. The central detector to this analysis is the Main Calorimeter, and it must be in the energy flow measured by the Main Calorimeter (MCAL) that one must look for a difference between higher-twist and minimum-twist events. It turns out that the difference lies in the energy-flow topology between the higher-twist (HT) prompt meson→decay products having a greater energy density relative to the initial axis then a corresponding minimum-twist (MT) jet. This will be discussed in more detail further on: first, however, one must discuss preliminary cuts made to ensure the integrity of our photoproduction data.

3.2 Preliminary Cuts

The collaborators on E683 arrived at a series of preliminary cuts to the data that effectively ensured the quality of the photoproduction data. These cuts were generally applied to the data before the analysis began. They consist of the following:

The following cuts ensured the quality of the Si measurement of the e as it passed through the beamline:

- 100 GeV/c $\leq E_{e_{Si}} \leq$ 350 GeV/c.
- χ^2/d.o.f reconstructed track from the Si tagging ≤ 12.0
- $N_{e_{Si}} = 1$ for an event.

This cut ensured that we knew the e recoil energy reasonably well:

- $N_{e_{RESH}}$ =1 for an event.

These cuts ensured that we did not have a large energy mismatch between what the E683 detector measured vs what the beamline measured:

- $E_{MCAL} \leq E_\gamma$ + 50 GeV/c
- $E_{BCAL} \leq E_\gamma$ + 50 GeV/c
- $E_{MCAL} + E_{BCAL} \leq E_\gamma$ + 75 GeV/c

The following cuts vetoed events triggered by μ that passed the hodoscope veto (as said before, the μ would produce a very unbalanced event in the MCAL):

- $N_{towers}(E_{tower} > .25GeV/c) \geq 30$
- $N_{towers}(E_{tower} > .50GeV/c) \geq 15$
- $\Sigma(E_{\perp_{MCAL_{+y}}} - E_{\perp_{MCAL_{-y}}})/E_{\perp_{MCAL}} \leq 0.8$ AND
- $\Sigma(E_{\perp_{MCAL_{+x}}} - E_{\perp_{MCAL_{-x}}})/E_{\perp_{MCAL}} \leq 0.8$
- $E_\perp$(highest-E tower)$/\Sigma E_\perp(MCAL) \leq 0.5$

3.3 Datastream Conversion to Kinematic Variables

In order to obtain the proper kinematic variables used in the present analysis, the digital numbers on data tapes have to be converted into physical quantities (E, $p_x, p_y, p_z, \theta, \phi$), and these primary physical quantities then manipulated to produce the kinematic variables relevant to the present analysis. The kinematic quantities further had to be boosted from the laboratory frame to the center-of-mass (COM) frame in order to simplify the analysis of the system.

For the relevant quantities:

- In order to obtain γ_L and β_L, the energy of the photon had to be measured. This was discussed earlier, it is obtained by measuring the energy of the electron before and after the bremsstrahlung of the photon. With the known E_γ, and the target mass (m_p), one can readily calculate γ_L and β_L, :

$$\gamma_L = \frac{m_p + E_\gamma}{\sqrt{2m_pE_\gamma + m_p^2}} \tag{8}$$

$$\beta_L = \sqrt{1 - \frac{1}{\gamma_L^2}} \tag{9}$$

- The calibration of the calorimeter, performed by Greg Morrow [7], transformed the ADC readouts from each module into the energies of the towers. First, the pedestal readouts for each module were subtracted from the ADC readouts. Then a weight factor multiplied the new ADC readouts. This weight factor compensated for the fact that the electromagnetic showers would deposit their energies primarily in the A′ layer and have a different signal than the hadronic showers, which would deposit their energies in all four layers. However, the A layer includes energy from both electromagnetic and hadronic showers. Therefore, to properly renormalize the output of the calorimeter to the energy of an event on average, one needs a additional energy scale factor, and obtains it from studying the energy deposition in the MCAL and determining the factor needed to multiply the aggregate response of the towers in order to arrive at the proper energy. Finally one has factors that take into accounts discrepancies for given towers from the norm–pathological towers, etc. Therefore the energy of a tower is computed by:

$$E_{tower} = \sum_{layers} (ADC-pedestal)\times(layerweight)\times(energyscale)\times(discrepancy factor) \quad (10)$$

The θ and ϕ for the center each tower are known in the lab. E683 assumes that all the energy for each tower is concentrated at the center of each tower (and that the towers are massless) for subsequent calculations of momentum and for the boosts into the COM frame.

The momentum components for the towers p_x, p_y, and p_z are obtained by simply multiplying the energies of the towers by the appropriate θ and ϕ combination. The boosted kinematic variables θ^*, E^* for each tower are obtained by the proper Lorentz boosts. These variables were used in the **clustering algorithm** and the **collimation variable** described below.

3.4 Clustering Algorithm

The clustering algorithm was a rather straightforward algorithm that determined the $p_\perp$ of a high-energy localized energy deposition in each event by obtaining clusters of towers in the main calorimeter. The algorithm had the following sequence:

- Find the highest energy tower in the main calorimeter (MCAL). The θ and ϕ of that tower form the seed coordinates of the cluster. The tower's energy forms the initial energy of the cluster.

- Using a circle from the seed axis with an opening angle of 0.4 from the seed axis (this opening angle radius is called the **mid radius**) add in the energies of all the towers whose centers lie within that radius.

- Use energy-weighted θ and ϕ of all the towers in this new collection of towers to recalculate θ and ϕ for the cluster as in equations (11) and (12) where the sums are over all the towers with an opening angle of less than 0.4 radians from the axis.

$$\theta_{cluster} = \frac{\sum \theta_{\mathrm{tower}} \times \mathrm{E}_{\mathrm{tower}}}{\sum \mathrm{E}_{\mathrm{tower}}} \quad (11)$$

$$\phi_{cluster} = \frac{\sum \phi_{\mathrm{tower}} \times \mathrm{E}_{\mathrm{tower}}}{\sum \mathrm{E}_{\mathrm{tower}}} \tag{12}$$

- Iterate the process starting from the second step until one of the following conditions has occurred:

  The latest axis has wandered farther than 0.3 from the seed axis

  The latest cluster energy is within ± 2.5% of the previous cluster energy. (**cluster stability factor**)

  The total number of iterations exceeds ten.

- Add the final cluster energies along the axis and multiply by the θ of the final cluster axis to obtain a $p_\perp$ for the cluster. The jet mass is small here by definition and does not effect the final result substantially.

Investigation of the clusters in the Monte Carlo showed that with a stability factor of 10% the algorithm converged at the seed values or after a single iteration at most. 5% had fewer difficulties, and 2.5% required the clusterer to perform at least one or two iterations. The imposition of the radius of 0.3 for the wandering limit stems from the fact that for higher-twist events, the event signal is mostly contained within a tower and its neighbors, and largely within a single tower (see figure (32)). The mid radius of 0.4 was optimized from Monte Carlo studies of both direct and resolved higher-twist processes. The towers are spaced $\approx$ 0.25 radians in the COM theta-phi space, the exact spacing varies with the position and size of the tower as well as the COM energy of the event. Finally, the limit of ten iterations for a cluster was very rarely used, but prevented the algorithm from crashing the analysis run for pathological events.

The difference in $p_\perp$ between the found cluster and the true initial meson/decay products for various inner radii is shown in (Tables (6) and (7)). These results show that the opening angle of 0.4 yielded the best resolution in the measured $p_\perp$ vs the true $p_\perp$.

The opening angles are illustrated in figure (18). Note that an outer radius of 1.4 was imposed from the axis of the cluster. The outer radius was a zone of exclusion between the first cluster and any tower that may be used as a seed for the second cluster found in each event. Studies were made to determine the utility of the second cluster

inner radius	μ	σ
0.3	.5479	.6061
0.4	.0761	.5751
0.5	.0020	.6126

Table 6: $\mid p_{\perp}^{cluster} - p_{\perp}^{true} \mid$ for Direct HT clusters. A cut $\mid \mathrm{cluster}_{foundaxis} - \mathrm{cluster}_{trueaxis} \mid < 0.3$ was made to ensure the cluster was not misidentified.

for enhancing the higher-twist signal. In practice, using a pure higher-twist sample in the Monte Carlo, arbitration schemes between the two clusters failed to improve on the 70% effectiveness in assuming the first cluster contained the higher-twist axis.

One may at first think it would be useful to add the **vector sum** of the momentum components in each tower of the cluster to obtain a proper θ and ϕ. Ideally, this is true, but the vector sum neglects the particle's showering in the MCAL. The showers deposit energy in other towers and therefore would distort the $p_{\perp}$ considerably if measured by the vector sum. Therefore, the total energy from the cluster was simply scaled along the θ and ϕ of the cluster to obtain the measured $p_{\perp}$. This $p_{\perp}$ neglects the **jet mass**, which is the momentum component lateral to the jet axis, but for the higher-twist events on which the present analysis concentrated, the jet mass was, by the nature of the event, small.

3.5 Collimation Variable

Collimation is a variable that measures the energy flow near the axis of the meson (or jet) relative to the integrated energy flow from the axis of the initial meson (or jet in the minimum-twist case) to an opening angle of 0.8 radians in the COM frame. Figure (19) illustrates this. Formally:

$$\mathrm{collimation}_{x8} \equiv \frac{\sum_{0.0}^{\mathrm{x}} \text{energy flow from meson or jet axis}}{\sum_{0.0}^{0.8} \text{energy flow from meson or jet axis}} \tag{13}$$

where the limits in equation (13) are the opening angle to x and to 0.8 radians. In practice, the definition was followed with the following important detail:

- The collimation variable (as well as the clusterer itself) calculated the distance from

inner radius	μ	σ
0.3	.6096	.7623
0.4	.1490	.7343
0.5	-.1277	.7491

Table 7: $\mid p_\perp^{cluster} - p_\perp^{true} \mid$ for Resolved HT clusters. A cut $\mid \text{cluster}_{foundaxis} - \text{cluster}_{trueaxis} \mid < 0.3$ was made to ensure the cluster was not misidentified.

the cluster axis to the **centers** of towers. If the center of the tower was within the relevant opening angle, the **entire** energy of the tower was included in the variable, if the center of the tower was outside of the relevant opening angle, **none** of the energy of the tower was included in the variable.

The opening angles were examined at 0.3, 0.4, 0.5, 0.6, and 0.7 radians. Tower granularity prevented any meaningful measurement below 0.3 radians. The resolving power of this variable was limited to 0.3 radians, so only collimation$_{38}$ was used for the final result (see figure (19)).

3.6 Empty Target Subtraction

The data sample was composed entirely of LH_2. The LH_2 was enclosed in a cryogenic pressure vessel, with the LH_2 consisting of $\approx 0.06\ X_o$. In order to compensate properly, the analysis used a process of **empty target subtraction**. Target-empty runs were used to subtract out the effect of the containment vessel. The flux for the E683 LH_2 data, runs from run 2097-3044, and for the empty target runs 1695-2949 were calculated: the time period embracing the data and the empty target is approximately September-December 1991. The following calculation was used:

$$\phi_{run} = (PB6IC - 21.0) \times \frac{BCAL^{gated}_{250GeV/c}}{BCAL^{ungated}_{250GeV/c}} \tag{14}$$

imposing the following cuts on the flux measurement in order to obtain good-quality data:

- PB6IC $\geq$ 100

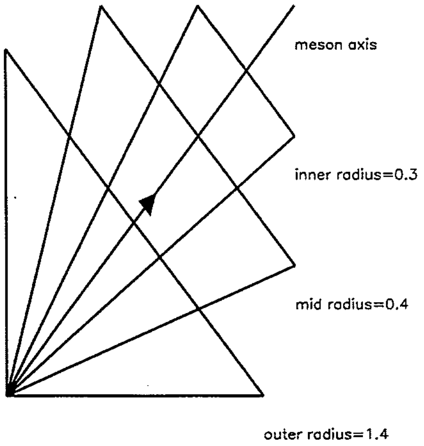

Figure 18: The clustering algorithm's opening angles from the cluster axis illustrated.

- PB6IC $\leq$ 2500

The factor 21.0 was the average pedestal per spill, and 100.0 and 2500.0 were loose cuts allowing for a wide range of good spills while vetoing pathological spills. $\frac{BCAL^{gated}_{250GeV/c}}{BCAL^{ungated}_{250GeV/c}}$ is the deadtime correction to the flux for energy readouts in the BCAL above 250 GeV/c.

The LH_2 data and the empty target data were normalized to the same flux, and the empty target data was subtracted bin-by-bin from the LH_2 data to obtain our kinematic values for collimation and our $p_\perp$ spectrum. In no case in the analysis did the empty-target subtraction affect the final values of our data to a significant degree. Figure (20) shows the LH_2 data $p_\perp$ spectrum, and figure (23) shows the the empty-target data spectrum. The 'bump' at $p_\perp \approx 3.0$ GeV/c is an artifact of the melding of the GLOBAL and TWOHI triggers together. The GLOBAL data, as shown in figure (21) does not have that 'bump', and the TWOHI data as shown in figure (22) has it to a lesser extent.

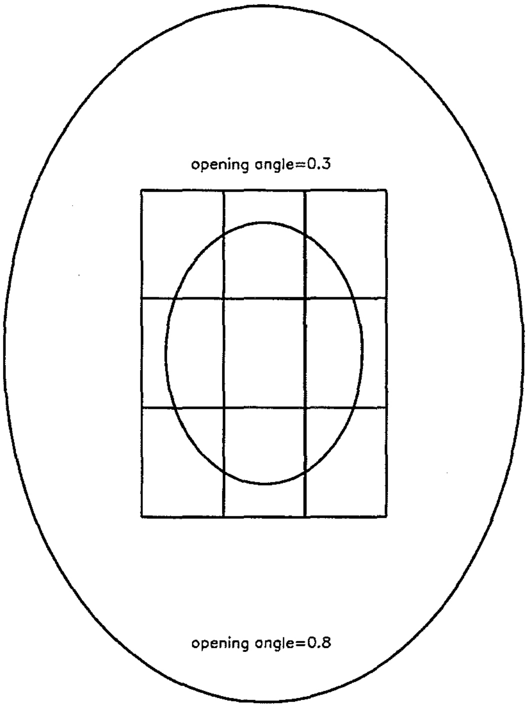

Figure 19: Collimation$_{38}$ illustrated: the energy inside the opening angle of 0.3 from the axis (inner circle) relative to the energy inside the opening angle of 0.8 from the axis (outer circle). Tower faces are shown with an opening angle of 0.25 from center-to-center.

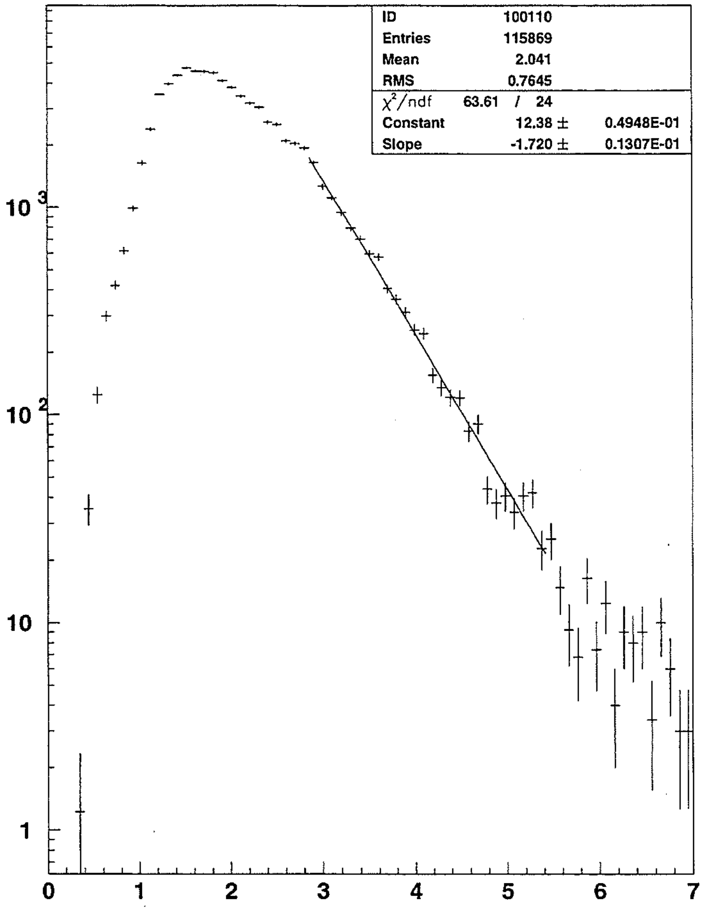

Figure 20: Data: LH_2 $p_\perp$ spectrum.

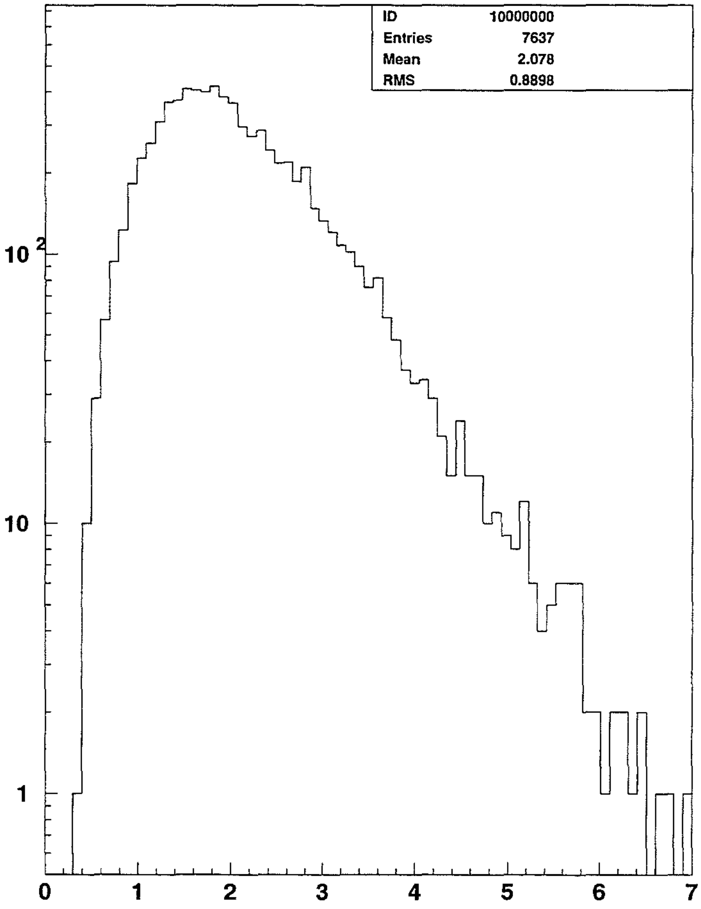

Figure 21: Data: GLOBAL LH_2 $p_\perp$ spectrum.

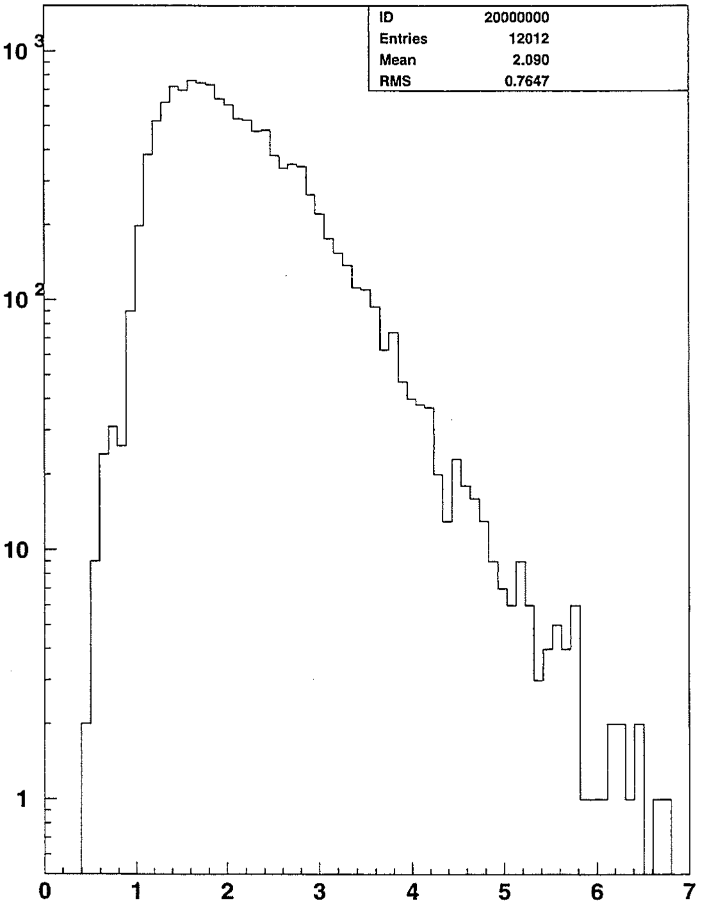

Figure 22: Data: TWOHI LH_2 $p_\perp$ spectrum.

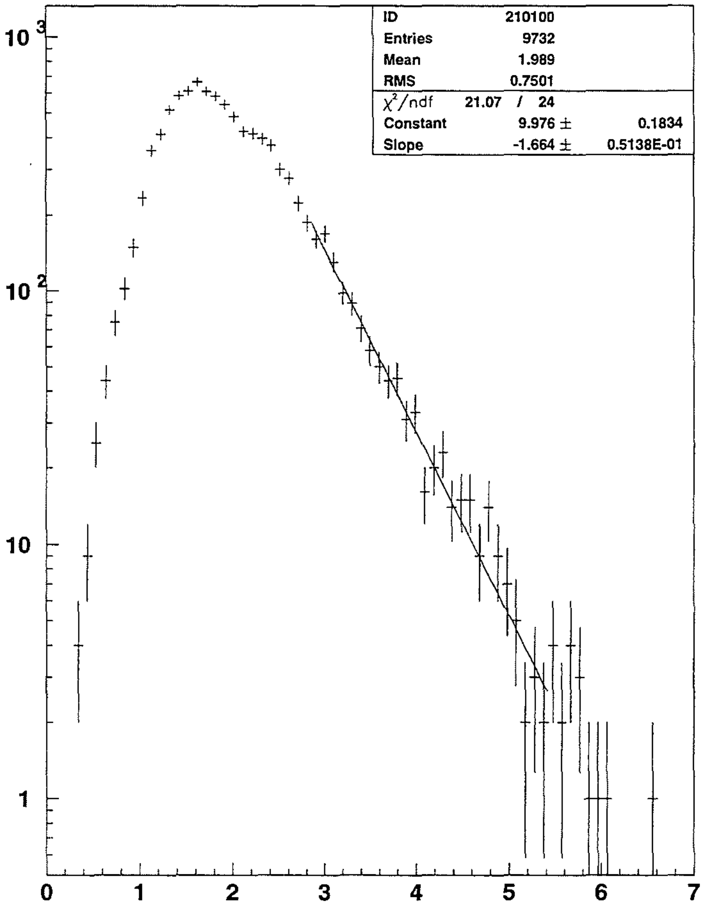

Figure 23: Data: Empty-target $p_\perp$ spectrum.

3.7 Data vs Beamline Monte Carlo for Triggered Photon Spectrum

As discussed above, there are three processes that compliment each other in photoproduction: direct, resolved, and VDM. The analysis must not only determine how to optimize higher-twist in each process, but the composite of the processes, since obtaining a separation of the event set unique to each class is not currently available for this experiment's data set.

Therefore, one must be able to arrive at the relative amounts of each process in the data sample. One can then mix the direct and resolved Monte Carlos in such a way as to obtain an accurate composite mix of the relevant kinematic variables (in this case the *collimation*$_{38}$ variable and the $p_\perp$ spectrum). As the $p_\perp$ spectra of the processes differ measurably from each other, and the higher-twist fraction in each spectrum is different, one must construct as accurate a mix as possible.

However as said before, the separation of the data types is not yet feasible in the experiment. The analysis opted for a mixture based on simulation of the events and detector effects as well as the simulation of the relative photon flux reaching our target ($\phi_\gamma(E)$), developed by the author in a beamline Monte Carlo [18] [19]. The function that determined the weighting was:

$$N_{trigger_\gamma}(E_\gamma) = \sum_{p=direct,resolved,VMD} \phi_\gamma(E_\gamma) \times \sigma_{theory}(p, E_\gamma) \times \epsilon_T(p, E_\gamma) \times \epsilon_{RESH}(E_\gamma) \tag{15}$$

where:

- $N_{trigger_\gamma}(E_\gamma)$ denotes the number of triggers that the experiment should observe as a function of the incoming photon energy (E_γ).
- p is simply the process (direct, resolved, VMD) to be summed over.
- $\phi_\gamma(E_\gamma)$ is the photon flux (as a function of E_γ) that reaches our target and pass the E683 gamma trigger. This is simulated by the beamline Monte Carlo.
- $\sigma_{theory}(p, E_\gamma)$ is the theoretically predicted cross-section at each photon energy for each process.

- $\epsilon_T(p, E_\gamma)$ is the probability that an event will trigger based on the incoming photon energy and the process.

- $\epsilon_{RESH}(E_\gamma)$ is the RESH efficiency for a incoming photon of a given energy. Note that the numbers used do **not** include the hardware efficiency of the RESH elements. The beamline Monte Carlo calculates the efficiency solely as a function of geometric acceptance at this point. A good hit is defined as the primary electron hitting RESH elements 1-10. The efficiency is only calculated for photons that pass the E683 gamma trigger.

The photon flux $\phi_\gamma(E_\gamma)$ has been simulated in the beam Monte Carlo (see fig (24)) in bins of 20 GeV/c width from 40-60 GeV/c to an upper limit of 440-460 GeV/c. The theoretical cross-section for each process $\sigma_{theory}(p, E_\gamma)$ is calculated in the same bin widths during the LUCIFER and TWISTER Monte Carlos. Finally, through generating large numbers of events and printing how many of those events generated by a given process and energy pass our GLOBAL and TWOHI triggers, the trigger efficiency $\epsilon_T(p, E_\gamma)$ can be extracted from the detector simulator. Multiplying the theoretical cross-sections by the trigger efficiencies and the photon cross-sections yield the relative number of events in Table (8).

The results of the simulated $N_{trigger_\gamma}(E_\gamma)$ spectrum are compared to the data's $N_{trigger_\gamma}(E_\gamma)$ spectrum in Figure (26). There appears to be a discrepancy for the low-E_γ spectrum. In order to circumvent the discrepancy, the author made a cut for $E_\gamma >$ 140.0 GeV/c for both the data and the beamline Monte Carlo and the following spectrum resulted (figure 27). The figures were normalized to the same area. At this point, the agreement between data and direct and resolved Monte Carlo mixture was deemed acceptable for the simulated spectrum to be used.

The production of the Monte Carloed kinematic variables of interest was attained by properly weighting the events from each process by the size of the cross-section of each process relative to the others at a given $E_\gamma > 140.0$ GeV/c as well as the energy-dependence of the cross-sections.

Note that the above comparison of the $N_{trigger_\gamma}(E_\gamma)$ spectrum doesn't truly prove that the Monte Carlo mixes of the processes are correct. One could come up with a different set of the relevant mixing parameters such that the Monte Carlo and data would

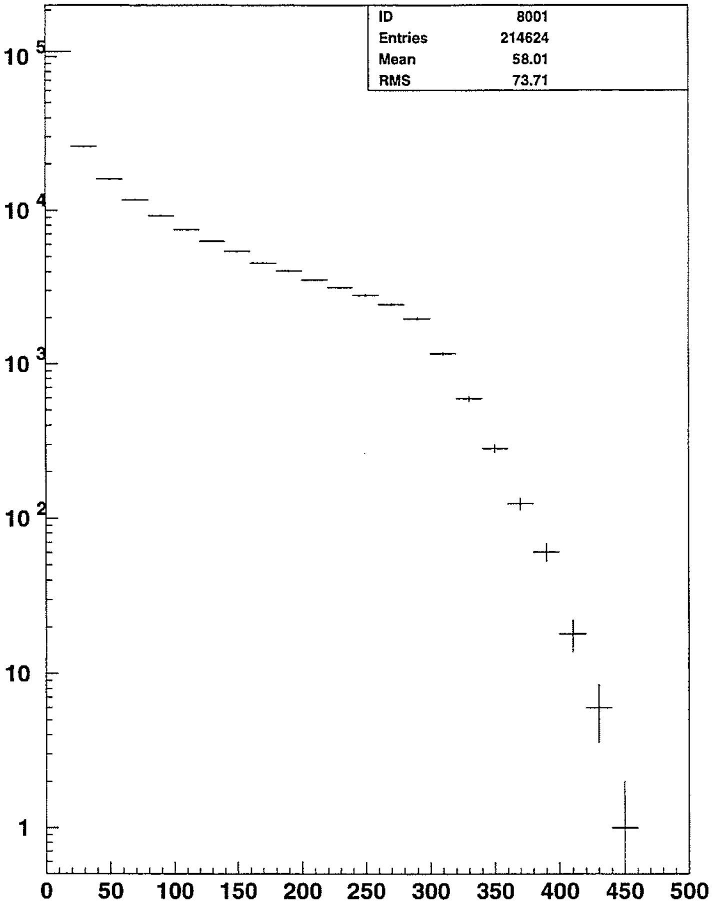

Figure 24: Monte Carlo: E683 beam Monte Carlo E_γ spectrum.

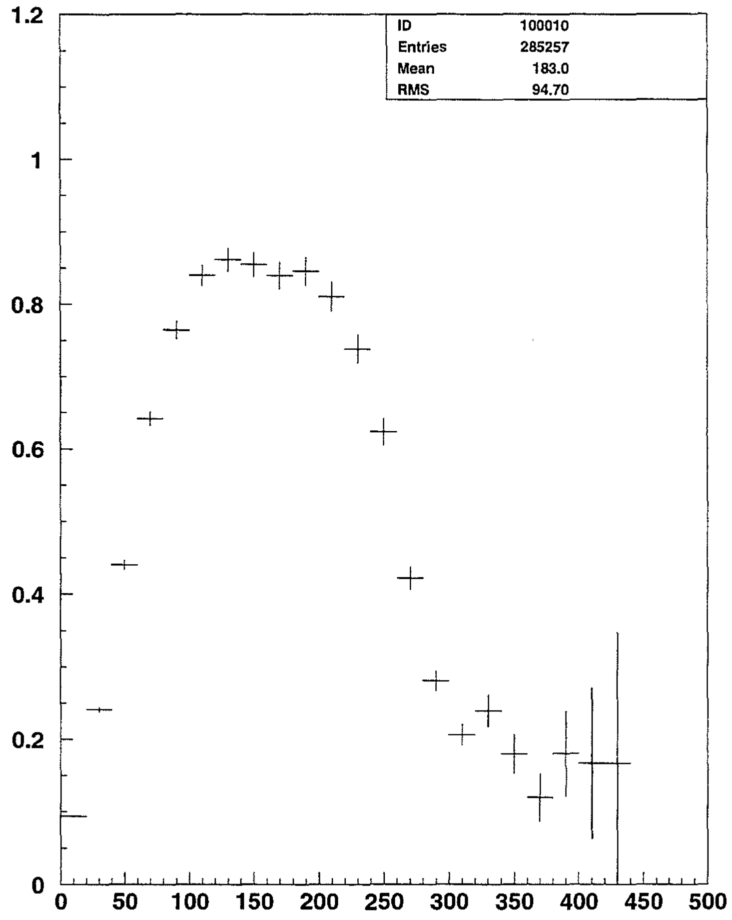

Figure 25: Monte Carlo: E683 beam Monte Carlo RESH efficiency as a function of E_γ. This excludes RESH elements 11, 12. The efficiency is calculated only for events that pass the E683 gamma trigger.

E_γ	VDM	Direct	Resolved	Total
50	38.2	229.2	286.5	553.9
70	39.0	442.0	481.0	962.0
90	84.6	404.2	498.2	987.0
110	80.3	386.9	737.3	1204.5
130	78.0	372.0	828.0	1278.0
150	74.3	356.4	891.0	1321.7
170	106.6	266.5	930.7	1303.8
190	103.6	333.0	1110.0	1546.6
210	96.0	342.4	1302.4	1740.8
230	118.8	313.2	1576.8	2008.8
250	175.0	315.0	1742.5	2232.5
270	230.0	331.2	2026.3	2587.5
290	228.0	324.9	2185.0	2737.9
310	148.8	206.4	1618.8	1974.0
330	119.4	100.1	856.4	1075.8
350	52.3	48.0	405.5	505.8
370	15.1	28.6	265.3	309.0
390	7.0	9.0	59.3	75.2
410	4.8	5.2	32.4	42.4
430	4.5	2.7	41.7	48.9
450	1.6	0.6	15.6	17.9

Table 8: Monte Carlo/detector simulations' prediction of relative number of events E683 observes ($N_{trigger_\gamma}(E_\gamma)$). These numbers are numbers of triggers relative to each process and incoming photon energy. The Monte Carlo set comprised 75K events. The numbers follow from the equation (15) and the photon flux from fig (24). $q_{\perp_{min}} = 1.0$ for all processes.

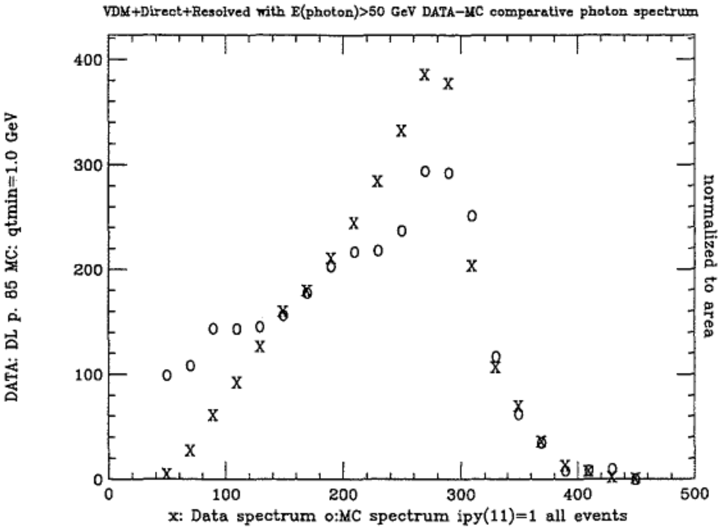

Figure 26: Data and Monte Carlo triggered photon spectra.

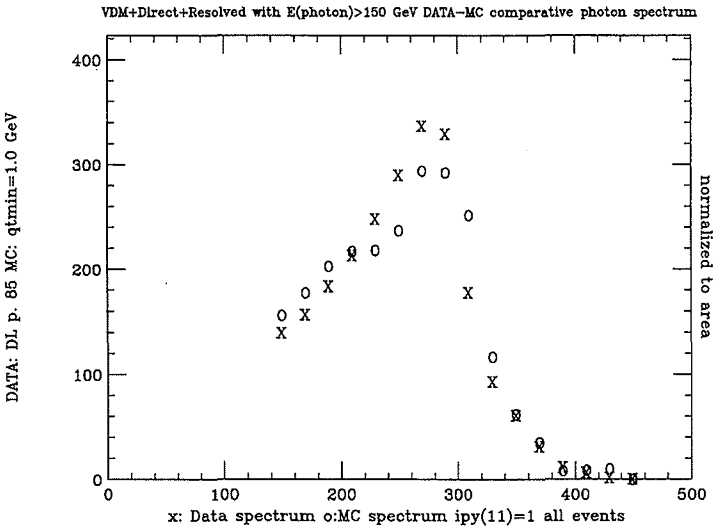

Figure 27: Data and Monte Carlo triggered photon spectra with $E_\gamma > 140$ GeV/c.

be consistent, for example, varying the trigger efficiency and the other two factors in a consistent way could also provide a consistent agreement. However, in lieu of a credible separation (and measurement) of each type of process in the data, this consistency check was deemed the optimal alternative.

3.8 Analysis-Specific Cuts

As previously mentioned, there were a number of cuts applicable to most analyses. In addition to those cuts, the cuts to the data and the Monte Carlo specific to the present analysis are:

- $E_\gamma = E_{e_{Si}} - E_{e_{resh}} \geq 140$ GeV/c. As said above, this cut was made in order to optimize agreement between our Monte Carlo and data $N_{trigger_\gamma}(E_\gamma)$ spectrum.
- The GLOBAL trigger for an event had to equal or surpass 9.12 GeV/c in energy. This cut circumvented the rollover for the GLOBAL trigger spectrum.
- OR
- The two hottest towers for an event (the TWOHI trigger) had to equal or surpass 0.855 GeV/c in energy.

From those cuts, the kinematic variables ($\text{collimation}_{38}, p_\perp$) were obtained for both the data and Monte Carlo sets.

4 Monte Carlo Analysis and Comparison to the Data

As said earlier, the analysis rests on two fundamental points:

- What higher-twist signal can be observed?
- How can this signal be enhanced?

The possible higher-twist signal was constrained by the detector, which is primarily a segmented calorimeter. Our segmented calorimeter can measure energy flow in space. From this one can measure $E_\perp$, and construct $p_\perp$. The most readily observable higher-twist signal is the different $p_\perp$ spectra for higher-twist events as opposed to minimum-twist events; higher-twist events have a $p_\perp^{-6}$ dependence as opposed to a pure minimum-twist spectrum falling off as $p_\perp^{-4}$. One can observe the different dependencies of the spectra in figures (28) and (29). An important caveat here is that the resolution of the calorimeter is not precise in measuring the energy or position for the jet or prompt meson.

Figures (28) and (29) show the **true** $p_\perp$ spectrum, that is the $p_\perp$ that we would be able to determine if we had a an exact measurement of the energy and angle of the initital meson and its decay products. It is **post-fragmentation**, meaning that the initial bare quarks have properly hadronized into observable particles, or in the case of a higher-twist initial meson, the meson has decayed into its observable constituents.

As stated earlier a Gaussian smearing of the $p_\perp$ spectrum (i.e., what happens after the true $p_\perp$ undergoes the detector resolution effects) will exacerbate the difficulties inherent in observing a signal. One of the primary goals of this analysis was to be able to distinguish a $p_\perp^{-6}$ higher-twist spectrum from a $p_\perp^{-4}$ minimum-twist spectrum, even after smearing effects due to calorimetry resolution. Figures (30) and (31) show that the goal of distinguishing post-smearing spectra was accomplished. The slope for an exponential fit for a pure higher-twist direct sample (figure (30)) being -1.28 vs the direct minimum-twist sample slope of -1.24 for the range of 3.0 GeV/c $< p_\perp <$ 5.5 GeV/c.

The Monte Carlos predict that in a pure direct-photon data set, after detector and trigger effects are accounted for, higher-twist events would comprise about 12% of the entire direct data set. For resolved photons, that figure is 7.5%, and for VDM photons,

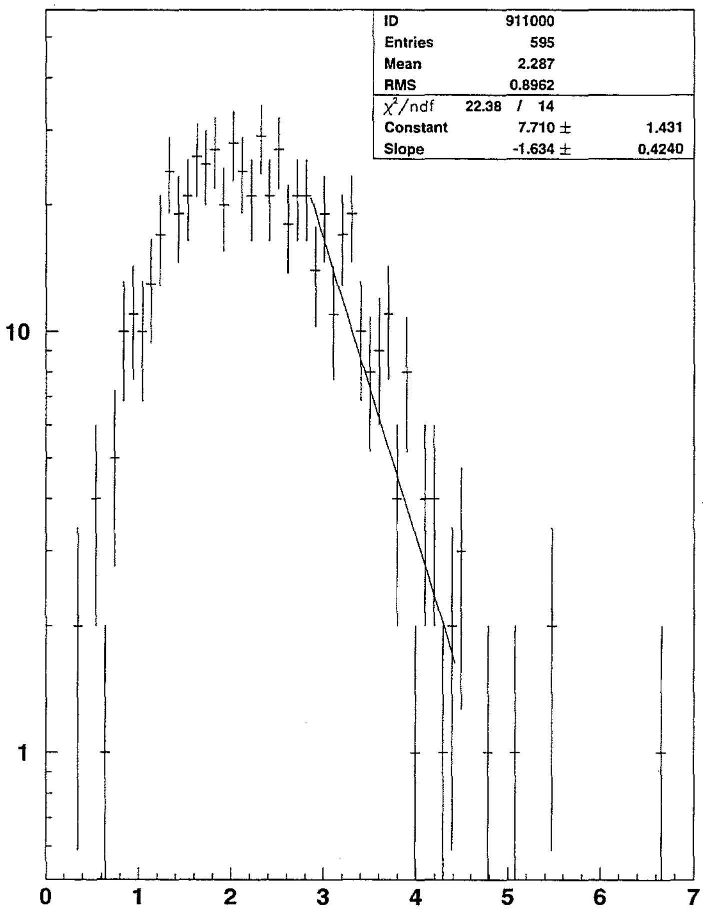

Figure 28: Monte Carlo: γ_{direct} higher-twist post-fragmentation $p_\perp$ spectrum.

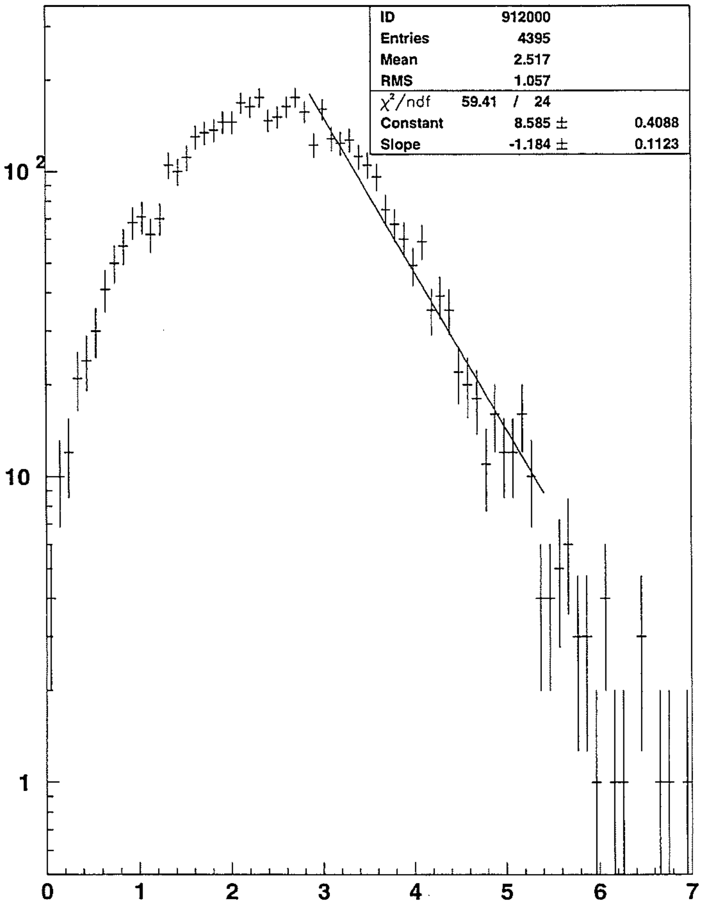

Figure 29: Monte Carlo: γ_{direct} minimum-twist post-fragmentation $p_\perp$ spectrum.

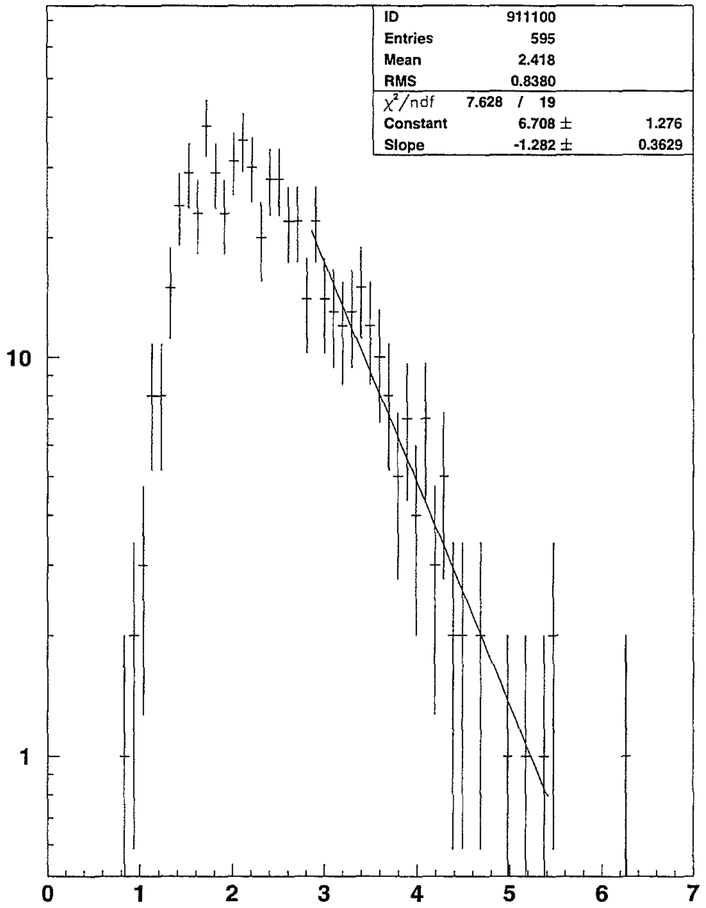

Figure 30: Monte Carlo: γ_{direct} higher-twist $p_\perp$ spectrum, including calorimetery resolution.

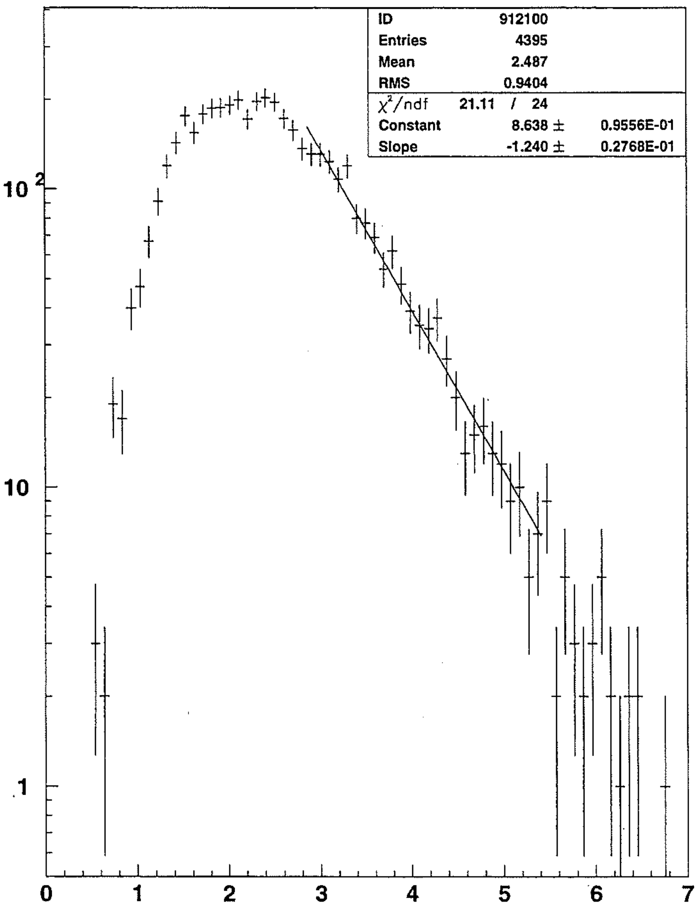

Figure 31: Monte Carlo: γ_{direct} minimum-twist $p_\perp$ spectrum, including calorimetry resolution.

higher-twist comprises 11% of a pure VDM data set. As will be discussed later, our final data signal is predicted to be about 8:1:1 resolved to direct to VDM ; this results in a prediction that about 8.8% of the data consists of higher-twist events. As was stated earlier, the uncertainty in the higher-twist cross section is about a factor of two either way. Therefore, the expected range of higher-twist signal fraction is anywhere from 4-17%.

Once the analysis settled on what exactly to look for, and ensured the ability to see it (at least in pure form), the question of how to enhance the signal/background ratio arose. A way to exploit the calorimeter's measurement of energy flow localized in space stems from the different nature of a higher-twist event relative to a minimum-twist event. Recall that in the higher-twist diagrams, a jet is balanced in $p_\perp$ by a single meson. This meson generally has a short lifetime, and promptly decays into two or three decay products. However, as opposed to a jet of many particles formed during the hadronization process, the higher-twist decay mesons are relatively tightly collimated around the initial axis of the prompt meson. This means that the energy deposited in the calorimeter should consitute a larger fraction of the total energy around the initial meson axis then the corresponding fraction of a minimum-twist jet's energy in a tight circle around its axis.

Figures (32) and (33) show the energy flows in a series of events for the higher-twist and minimum-twist samples. The plots have entries in the center-of-mass (COM) frame. For each event the fraction of the energy in a given tower divided by the energy in the entire calorimeter is calculated and added to the corresponding angle bin. Thus the y-axis is the sum of these fractions summed over all towers and all events.

A standard opening angle for jet measurement of 0.8 radians in the COM frame is used for the jet measurements. From the figure, one can plainly see that most of the higher-twist axis' energy is concentrated to a greater extent at angles less than 0.8 as opposed to the minimum-twist jet-axis.

A cautionary note: the figures (32) and (33) used perfect axis spatial resolution for the plot. In reality, calorimetry resolution and the inherent granularity of the towers in space tend to blur this distinction. However, one can perceive the motivation behind the kinematic investigations of collimation as a cut, and the construction of the clustering algorithm.

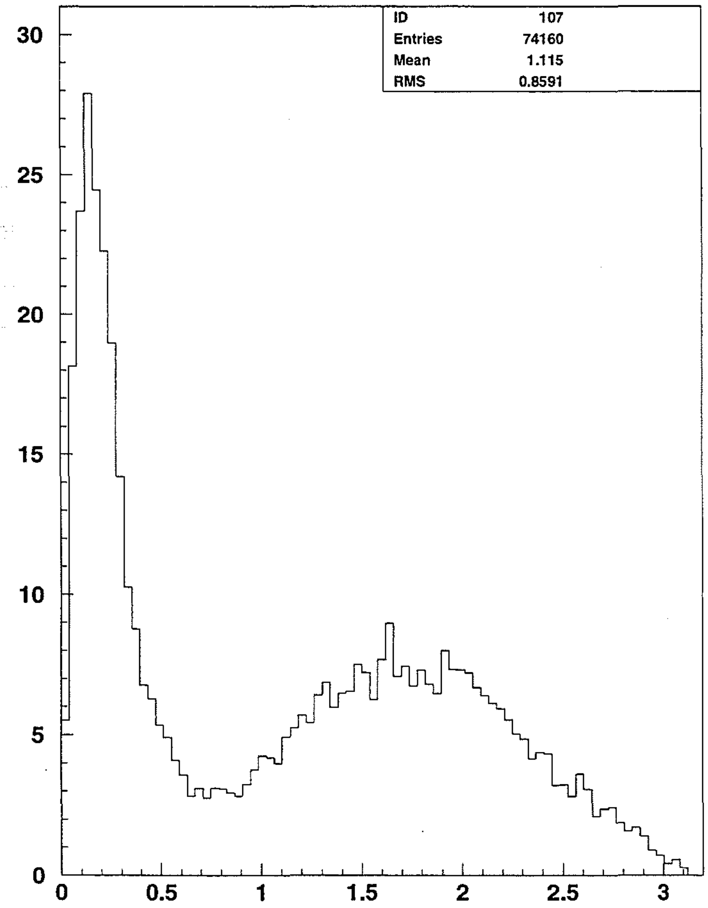

Figure 32: Monte Carlo: γ_{direct} energy flow from higher-twist naive initial-meson axis. The naive axis is the axis of the initial higher-twist meson.

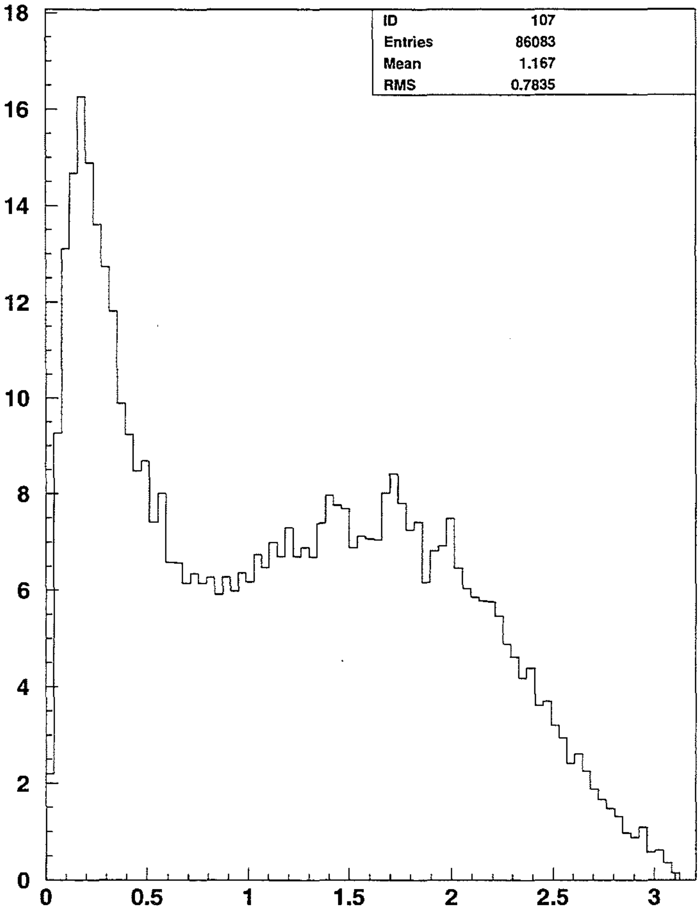

Figure 33: Monte Carlo: γ_{direct} energy flow from the minimum-twist naive jet axis. The naive axis is the axis of one of the bare quarks from the $\gamma \rightarrow$ q interaction.

4.1 Determining the $p_\perp$ Spectrum: The $q_{\perp_{min}}$ Factor

The $q_{\perp_{min}}$ factor is the minimum $q_\perp$ with which the Monte Carlos LUCIFER and TWISTER will generate events. $q_\perp$ is the transverse component of the q^2 of the exchanged gluon between the interacting particles. This component (in the ideal case) translates into the $p_\perp$ of the outgoing parton (or initial meson). For the resolved process however, the $k_\perp$ of the γ, which is the $q_\perp$ internal to the q $\overline{\text{q}}$ produced by a gluon exchange between the pair, complicates this correlation to such a degree that it critically affects the results of the analysis. This will be discussed in more detail below.

The present analysis is especially concerned with the behavior of the $p_\perp$ spectrum at low $p_\perp$; the region where higher-twist events are predicted to be in greatest concentration. Therefore, obtaining the most accurate $p_\perp$ possible using the simulations is critical to this analysis.

To obtain the low-$p_\perp$ spectrum as accurately as possible, one must use a $q_{\perp_{min}}$ as low as possible. Figures (34) and (35) show the $p_\perp$ spectrum for an example of direct photons using $q_{\perp_{min}}$ of 2.0 GeV/c and 1.0 GeV/c; these should be compared to figure (20). The critical areas affected by the $q_{\perp_{min}}$ selection are the $p_\perp$ rollover point in the spectrum. Related to that is where the $p_\perp$ begins a flat descent as the rollover point is past. The rollover point comes from the fact that the hardware trigger is not strictly correlated to the $p_\perp$ of a cluster. Instead it is determented by a smeared value of the $E_\perp$ either in the entire calorimeter or the $E_\perp$ of the two highest-$E_\perp$ towers in the calorimeter.

At the lower $q_{\perp_{min}}$, the triggering efficiency (ϵ_T) for all processes decreases markedly, but far more so for direct photons than for resolved photons. To use the example E_γ of 250 GeV/c again, the resolved ϵ_T at $q_{\perp_{min}}$ of 2.0 is $\approx$ 0.136, and for $q_{\perp_{min}}$ of 1.0 it is $\approx$ 0.024. For direct photons, the ϵ_T at $q_{\perp_{min}}$ of 2.0 is $\approx$ .113, while $q_{\perp_{min}}$ of 1.0 it is $\approx$ 0.015. This can be explained by the phenomenon of the $k_\perp$ of the photon. $k_\perp$ only occurs in resolved and VDM photons. The reason lies in the characterization of $k_\perp$. Recall that the distinction between the resolved and VMD models is an artifice, and that they essentially merge as $\alpha_s \rightarrow\approx 1$. This is because as $\alpha_s \rightarrow\approx 1$, the gluon-q coupling increases (after all, the field strengthens, so the field-carrying bosons should increase in intensity). At this point, the normal $p_\perp$ of a quark is increased measurably.

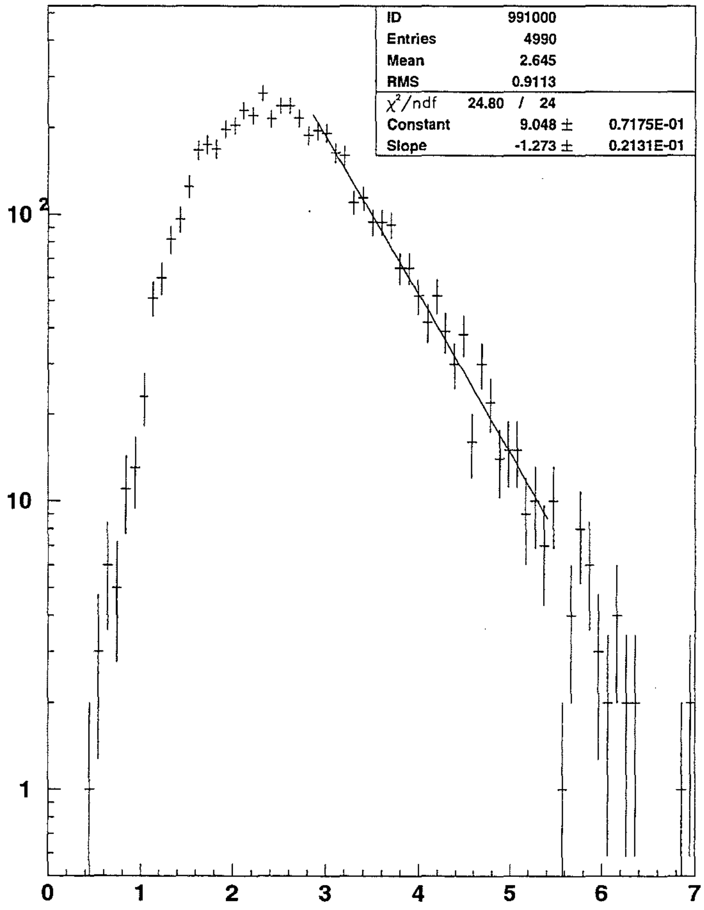

Figure 34: Monte Carlo: γ_{direct} $p_\perp$ spectrum at a $q_{\perp_{min}} = 2.0$ GeV/c.

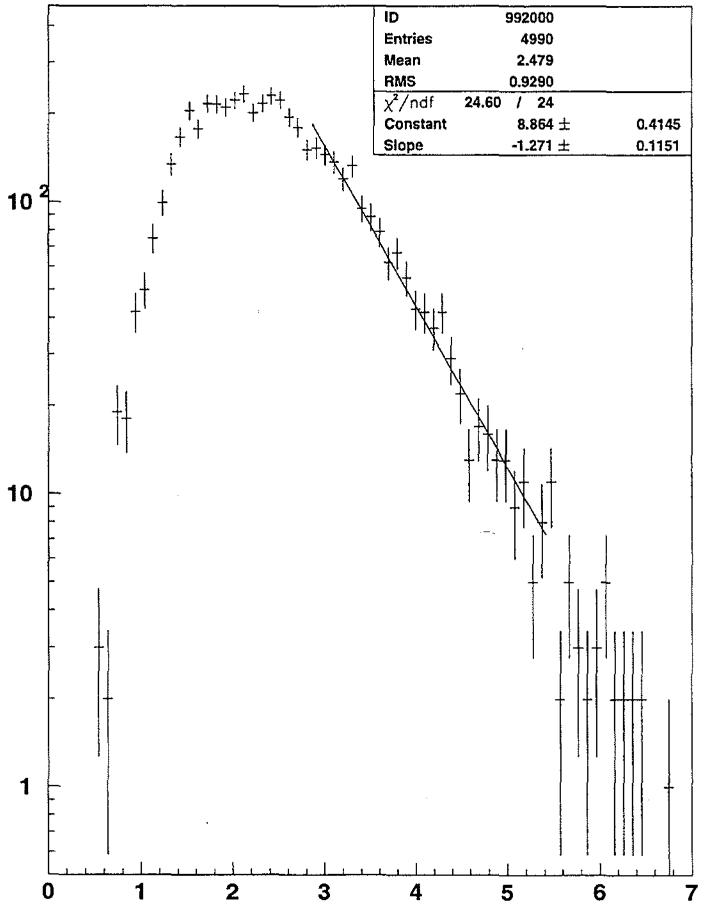

Figure 35: Monte Carlo: γ_{direct} $p_\perp$ spectrum at a $q_{\perp_{min}} = 1.0$ GeV/c.

A typical $k_\perp$ for a photon is ≈ 1.0 GeV/c. This can increase the apparent $p_\perp$ of an outgoing parton by that amount, if the $k_\perp$ is in the same direction as the $p_\perp$. Therefore, $k_\perp$ can have a much greater relative effect on allowing a low-$p_\perp$ parton passing a threshold than a higher-$p_\perp$ parton. Hence the relative increase in ϵ_T for resolved as opposed to direct for low $q_{\perp_{min}}$. Further, the resolved theoretical photoproduction cross-section falls sharply with $q_{\perp_{min}}$ relative to the direct. For example, for an E_γ of 250 GeV/c, the resolved cross-section for a $q_{\perp_{min}}$ of 1.0 is $\approx$ 29000 nb; for a $q_{\perp_{min}}$ of 2.0 it is $\approx$ 1000 nb. The direct cross-section for a $q_{\perp_{min}}$ of 1.0 is $\approx$ 8400 nb; for the $q_{\perp_{min}}$ of 1.0 it is $\approx$ 1100 nb. This is explainable due to the fact that as $q^2 \rightarrow\approx 0$, $\alpha_s \rightarrow\approx 1$. Leading-order resolved process are of $O(\alpha_s^2)$ as opposed to leading-order direct process being $O(\alpha_s)$. VMD is of even a higher-order of $O(\alpha_s)$. When these effects are added together, the observed cross-section of the resolved photon for E_γ of 250 GeV/c and a $q_{\perp_{min}}$ of 1.0 is $\approx$ 700 nb, for a $q_{\perp_{min}}$ of 2.0 it is $\approx$ 130 nb. For the direct photons, the numbers are 126 and 125 nb respectively.

It should be noted that there are various ways of parameterizing the $q^2 \leftrightarrow q_\perp$ correlation in the Monte Carlos[4]:

$$q^2 = \frac{\hat{\mathrm{s}}\hat{\mathrm{t}}\hat{\mathrm{u}}}{\hat{\mathrm{s}}^2 + \hat{\mathrm{t}}^2 + \hat{\mathrm{u}}^2} \tag{16}$$

$$q^2 = -\hat{\mathrm{t}} \tag{17}$$

$$q^2 = \mathrm{a} \cdot q_\perp^2 (\text{a is variable but usually 0.25}) \tag{18}$$

$$q^2 = \mathrm{b} \cdot (1 - x_\perp) \cdot q_\perp^2 (\text{b is variable but usually 0.5}) \tag{19}$$

The first choice is just a symmetrized combination of the s,t and u channels proportional to $p_\perp^2$. The second choice is the Mandelstam variable proportional to $p_\perp$. The third choice is simply an explicit tie in between the q^2 of the interaction to its $q_\perp$, justifiable as a loose correlation that occurs between the full component of momentum and its transverse component. The last one accounts for the fact that the third one doesn't necessarily account for all the kinematic factors in the correlation, and that there should be some dependence on $(1 - x_\perp)$ as $x_\perp \rightarrow 1$. [17]. For very low $q_{\perp_{min}}$ (such as the $q_{\perp_{min}}$

of 1.0 Gev/c used in the present analysis) the first choice is the only one that allows perturbative calculations to converge.

The $k_\perp$ of the photon returns to critically affect the results of the analysis via the blurring of the $p_\perp$ spectrum in a related process called $k_\perp$ **promotion** to be described later.

$q_{\perp_{min}} = 1.0$ GeV/c was the lowest $q_{\perp_{min}}$ that could be achieved in the Monte Carlo. The limit on $q_{\perp_{min}}$ stems from the limits of pQCD, and especially the simulations' calculation using pQCD. As described above, as $q^2 \rightarrow\approx 0$, $\alpha_s \rightarrow\approx 1$. As $\alpha_s \rightarrow\approx 1$, pQCD (as well as any perturbative calculation) fails. Not only do the calculations become more and more suspect for the low q^2, but indeed, the calculation may fail entirely, crashing the simulation. Furthermore, as the trigger efficiency plummets, the amount of CPU time required to generate a given trigger amount soars to the point of unfeasability. Effectively, a $q_{\perp_{min}}$ of 1.0 is the absolute minimum that the Monte Carlo is capable of handling with any degree of effectiveness. This is a artificial barrier to the analysis imposed by the limits of the simulation's ability to simulate low q^2 events that significantly affects the results of the analysis.

4.2 Determining the Higher-Twist Mixture in the Data

At this point, the present analysis can use the weighting factors on an event-by-event basis in a steering program to transform the separate Monte Carlos into a properly weighted combined result, and compare the result to data in order to determine the amount of higher-twist signal in the data. Using the kinematic variable collimation$_{38}$ for the properly weighted mixture of Monte Carlo events and data events, one can compare the distributions and make the optimal cut suggested by the Monte Carlo results that maximizes the higher-twist component of the $p_\perp$ spectrum. This is done by obtaining the collimation$_{38}$ for the higher-twist distribution and the minimum-twist distribution in the Monte Carlo and comparing the two distributions as shown in Figures (36) and (37). The algorithm for this is to make progressively harder cuts in the collimation$_{38}$ distribution and calculate the fraction of higher-twist events remaining multiplied by the fraction of minimum-twist events rejected.

This distribution has a peak as the collimation$_{38}$ varies from 0.0 to 1.0. The peak of the distribution indicates the factor for the collimation$_{38}$ cut to be made in the

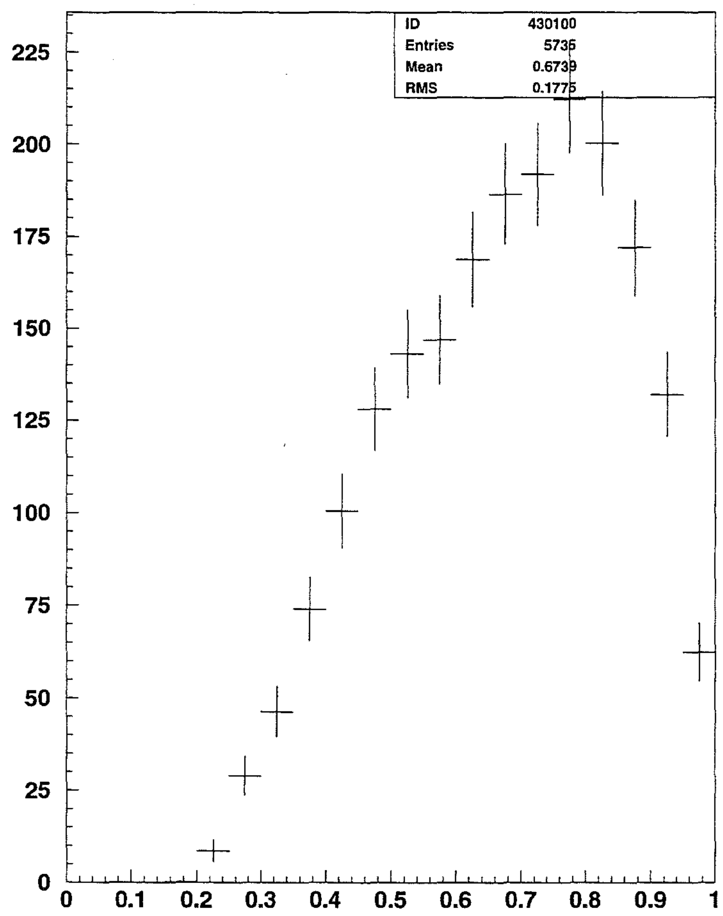

Figure 36: Monte Carlo: collimation$_{38}$ distribution for higher-twist events.

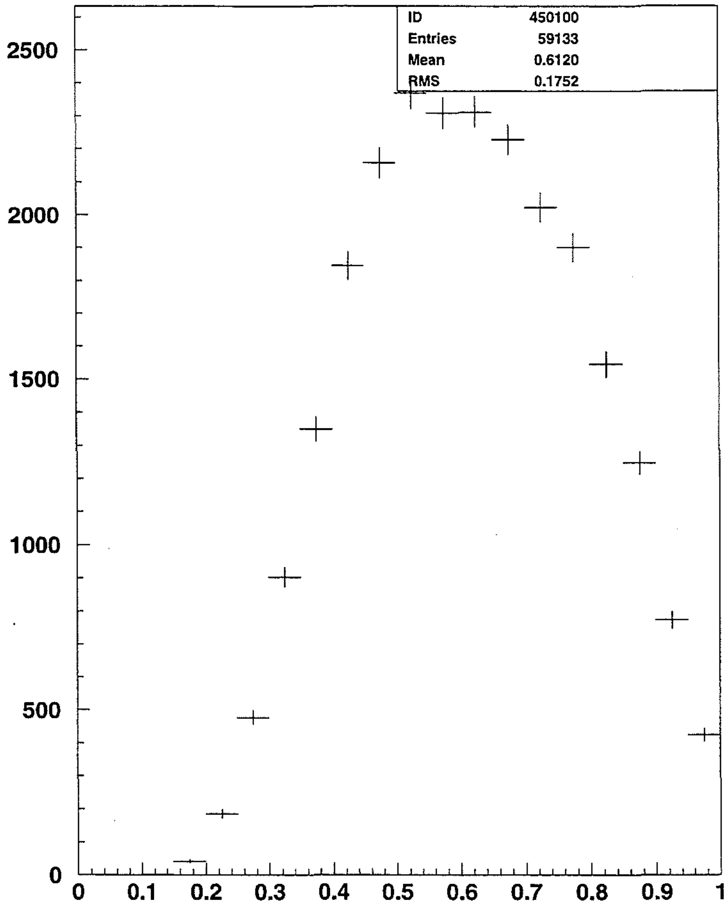

Figure 37: Monte Carlo: collimation$_{38}$ distribution for minimum-twist events.

$p_{\perp_{min}}$	HT μ	HT σ	MT μ	MT σ	MC μ	MC σ	Data μ	Data σ
2.0	.74	.14	.69	.15	.69	.15	.67	.15
2.5	.78	.13	.72	.14	.73	.14	.72	.13
3.0	.80	.12	.74	.14	.74	.14	.74	.13
3.5	.81	.11	.77	.13	.77	.13	.75	.12
4.0	.82	.09	.78	.13	.78	.13	.77	.12

Table 9: collimation$_{38}$ means and sigmas for higher-twist, minimum-twist, combination Monte Carlo, and the LH$_2$ data sample. The ranges of the $p_\perp$ is from $p_{\perp_{min}}$ given in the first column, to ∞.

combined Monte Carlo set and the data set to obtain a resultant $p_\perp$ spectrum. From the resultant pure higher-twist and pure minimum-twist $p_\perp$ spectrum from the Monte Carlo the resultant mixtures of the two spectra necessary to produce the $p_\perp$ spectrum from the data can then be calculated

Table (9) compares the collimation$_{38}$ variables μ and σ for higher-twist, minimum-twist, Monte Carlo composite, and the data. The analysis was concerned about the accuracy of the simulation's modeling of the low-$p_\perp$ region. Therefore, the final analysis was parallelized into the analysis of various $p_\perp$ regions in table (9).

Figure (38) shows the relationship of higher-twist fraction remaining multiplied by minimum-twist fraction rejected for the entire $p_\perp$ spectrum. Table (10) lists the optimized collimation$_{38}$ values for each of the $p_\perp$ ranges. The final **uncut**, or pre-collimation cut LH$_2$ $p_\perp$ spectrum is shown in (39). The final Monte Carlo $p_\perp$ combined spectrum is shown in (40).

The final Monte Carlo higher-twist $p_\perp$ spectrum is shown in (41). The final Monte Carlo minimum-twist $p_\perp$ spectrum is shown in (42).

The various contributing processes to the final spectrum are also of interest. Figure (43) shows the higher-twist $p_\perp$ spectra from direct photons. Figure (44) shows the minimum-twist $p_\perp$ spectra from direct photons. Figure (45) shows the higher-twist $p_\perp$ spectra from resolved photons. Figure (46) shows the minimum-twist $p_\perp$ spectra from resolved photons. Figure (47) shows the higher-twist $p_\perp$ spectra from VMD photons. Figure (48) shows the minimum-twist $p_\perp$ spectra from VMD photons.

After making the collimation cut, the final **optimized** (post-cut) data spectrum is

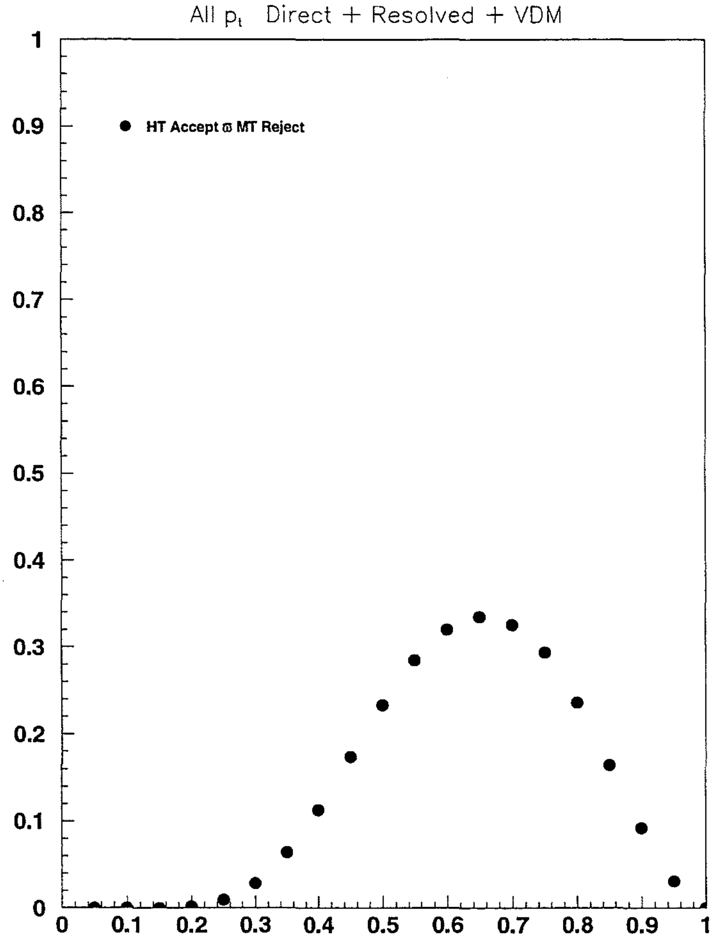

Figure 38: Monte Carlo: Illustration of the fraction of higher-twist events remaining multiplied by the fraction of minimum-twist amounts rejected as one varies collimation$_{38}$ from 0.0 to 1.0 for the full $p_\perp$ spectrum.

$p_\perp$ min	optimal collimation$_{38}$ value
2.0	0.72
2.5	0.75
3.0	0.79
3.5	0.80
4.0	0.80

Table 10: Optimized collimation$_{38}$ for the various $p_\perp$ ranges used in obtaining the final results.

shown in figure (49). The final combined Monte Carlo $p_\perp$ spectrum is shown in figure (50). The final optimized Monte Carlo higher-twist $p_\perp$ spectrum is shown in (51). The final optimized Monte Carlo minimum-twist $p_\perp$ spectrum is shown in (52).

After obtaining the optimized higher-twist and minimum-twist Monte Carlo $p_\perp$ spectra, an HBOOK subroutine HMCMLL was used to obtain the relative mixtures of the higher-twist and minimum-twist $p_\perp$ spectra that best reproduced the data. HMCMLL uses a MINUIT distribution-fit routine to fit the Monte Carlo distributions to the data distribution, using a binned maximum likelihood fit that includes the effect of both data and Monte Carlo statistics. The best estimate of the fraction of each Monte Carlo distribution present in the data is returned, with an error estimate [20].

Table (11) shows the resultant fractions for the optimized spectra. Recall that the theoretical estimate of higher-twist was from 3% to 12% of the uncut sample. Obviously, for $p_\perp$ below 3.0 GeV/c. the mixtures are unphysical. Even in the region where $p_\perp$ is greater than 3.0 GeV/c, the mixture is far in excess of prediction.

4.3 Discussion of Results and Physical Explanation

There are a number of factors that distort the mixtures of higher-twist and minimum-twist in the final $p_\perp$ spectrum.

- The $q_{\perp_{min}}$ is a significant and artificial barrier towards properly modelling the $p_\perp$ accurately at low $p_\perp$. At this time, the calculability of the kinematics in QCD is limited to the region where pQCD is valid. As aforementioned, at such a low $q_{\perp_{min}}$, pQCD becomes ever more suspect in accurately determining the cross-sections for various processes. Yet the present analysis was constrained to using a low $q_{\perp_{min}}$ in order to reconcile the data and Monte Carlo $p_\perp$ spectrum as accurately as possible. This is a strong reason to be suspicious of the low $p_\perp$ results. However, higher-twist by its nature is a low $p_\perp$ phenomenon, at least in theory. Therefore the present analysis was constrained to analyze using different $p_\perp$ ranges in order to determine the point in the $p_\perp$ the analysis could begin to hold credible the comparison.

- Especially at the low $p_\perp$ region of the data, the hardware effects are the most poorly understood. Hardware inefficiencies begin to show up (especially in the GLOBAL and TWOHI triggers) in the lower regions of the triggers. The cuts imposed on the

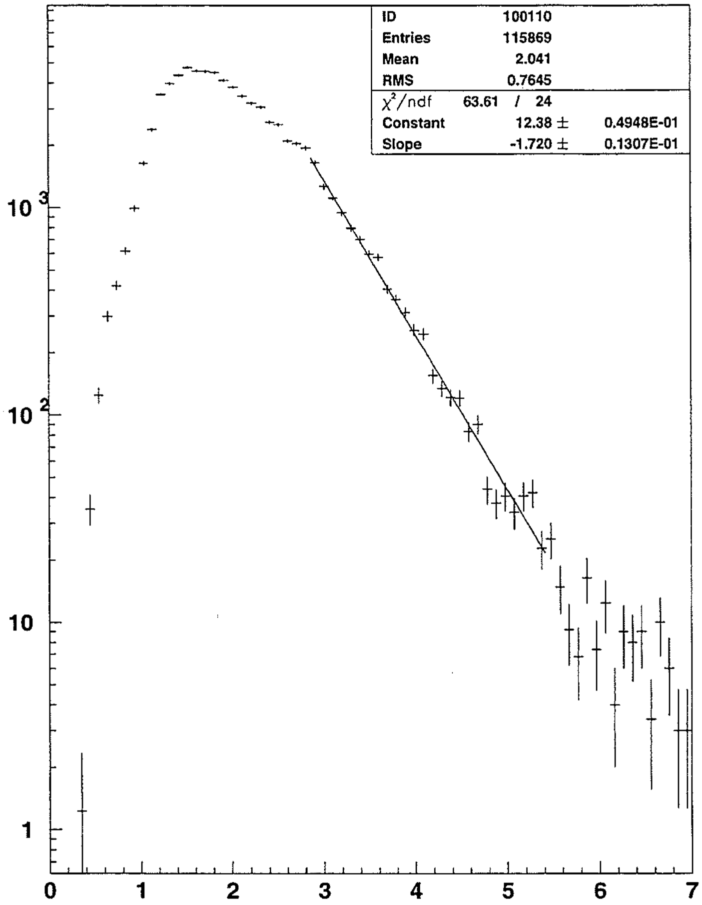

Figure 39: Data: The final uncut data $p_\perp$ spectrum.

$p_\perp$ min	HT Frac	HT error	MT frac	MT error	Monte Carlo HT predict
2.0	0.29E+01	0.54E+00	-.19E+01	0.53E+00	0.126E+00
2.5	0.26E+01	0.59E+00	-.16E+01	0.58E+00	0.122E+00
3.0	0.19E+01	0.74E+00	-.87E+00	0.72E+00	0.129E+00
3.5	0.98E+00	0.47E+00	0.33-01	0.45E+00	0.129E+00
4.0	0.73E+00	0.17E+00	0.29E+00	0.14E+00	0.119E+00

Table 11: Optimized higher-twist and minimum-twist fractions and errors with Monte Carlò predictions.

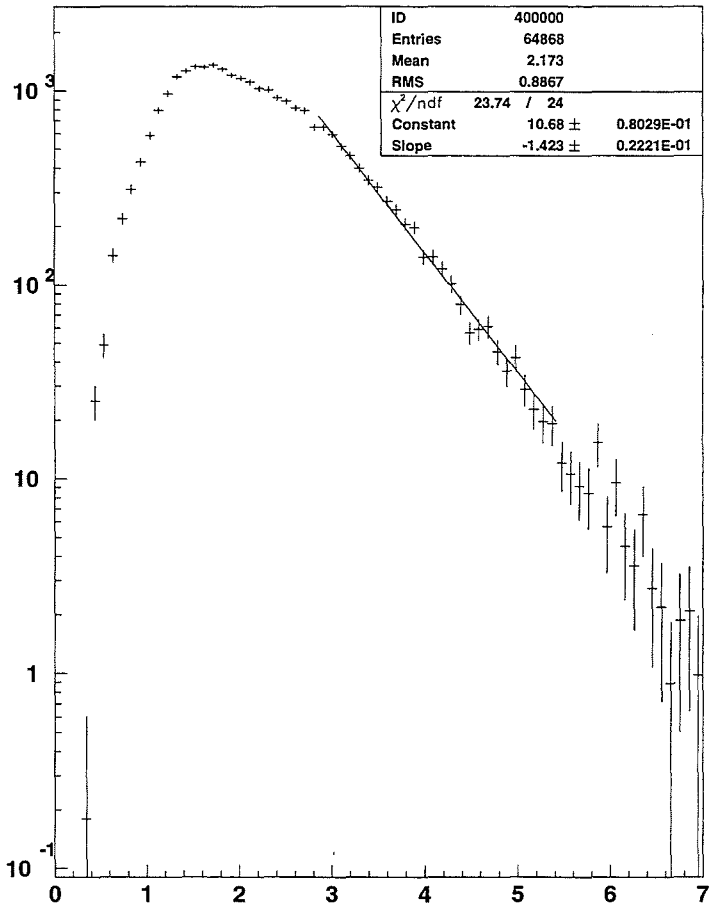

Figure 40: Monte Carlo: The final uncut Monte Carlo $p_\perp$ spectrum.

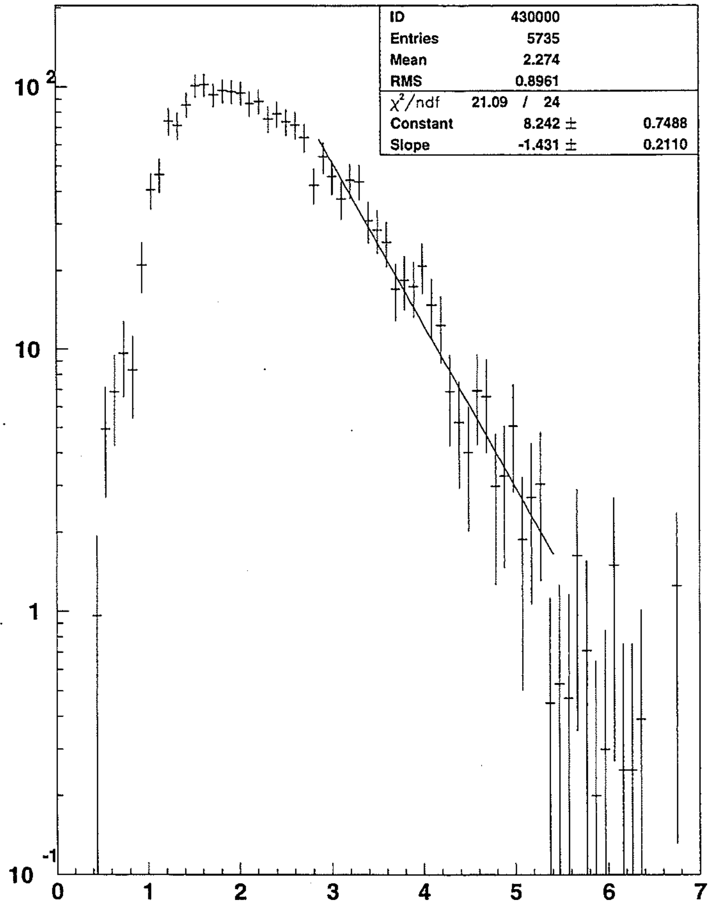

Figure 41: Monte Carlo: The final uncut Monte Carlo higher-twist $p_\perp$ spectrum.

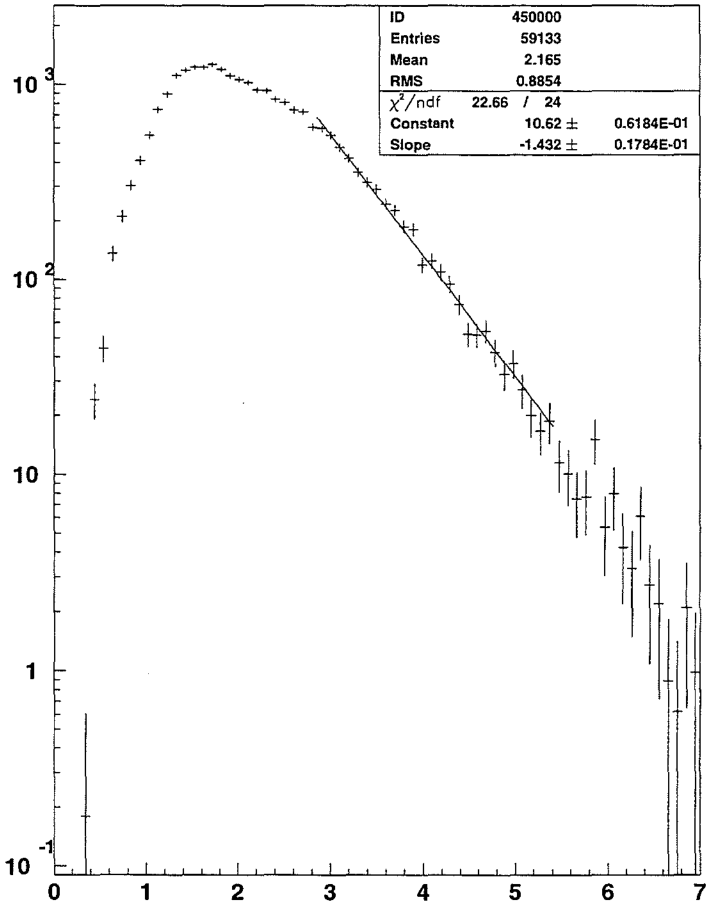

Figure 42: Monte Carlo: The final uncut Monte Carlo minimum-twist $p_\perp$ spectrum.

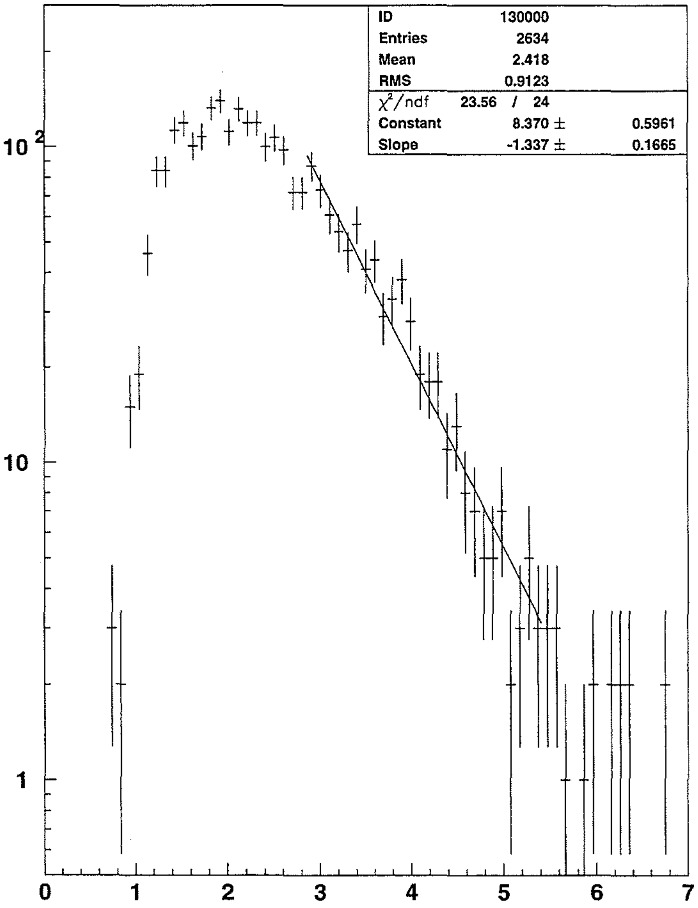

Figure 43: Monte Carlo: γ_{direct} uncut Monte Carlo higher-twist $p_\perp$ spectrum.

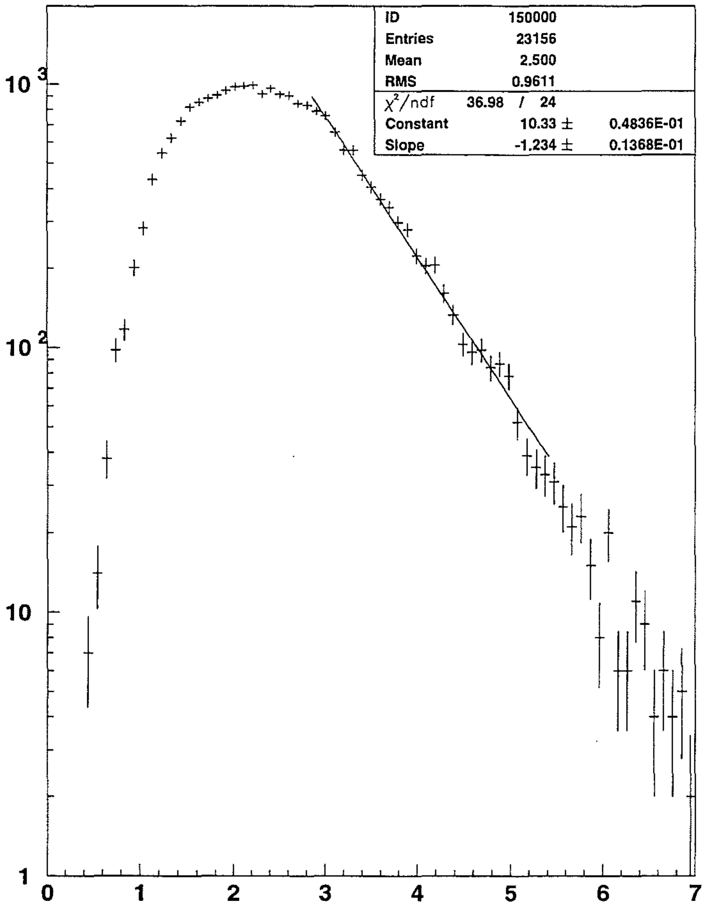

Figure 44: Monte Carlo: γ_{direct} uncut Monte Carlo minimum-twist $p_\perp$ spectrum.

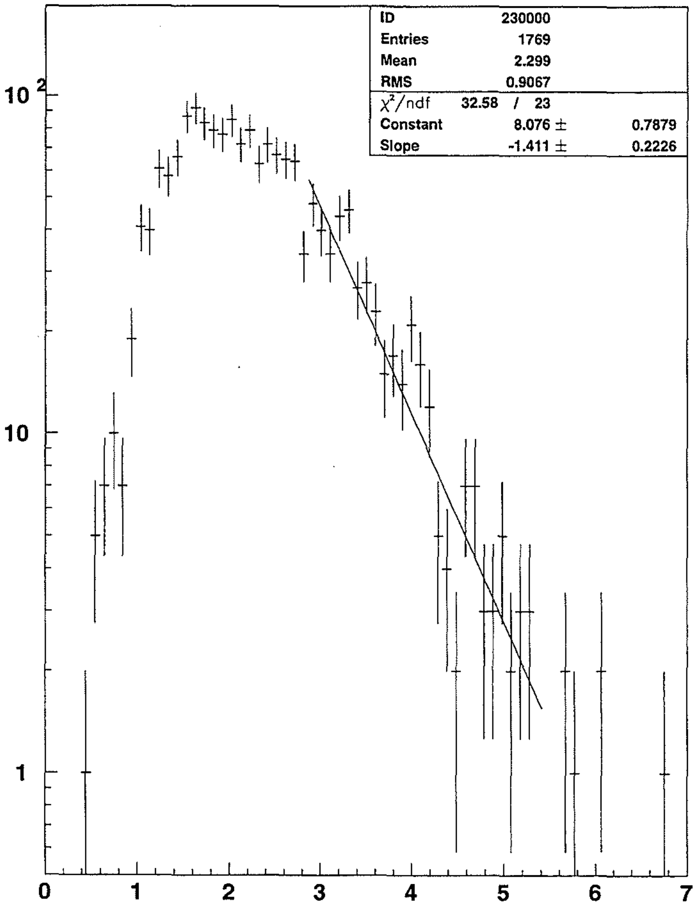

Figure 45: Monte Carlo: $\gamma_{resolved}$ uncut Monte Carlo higher-twist $p_\perp$ spectrum.

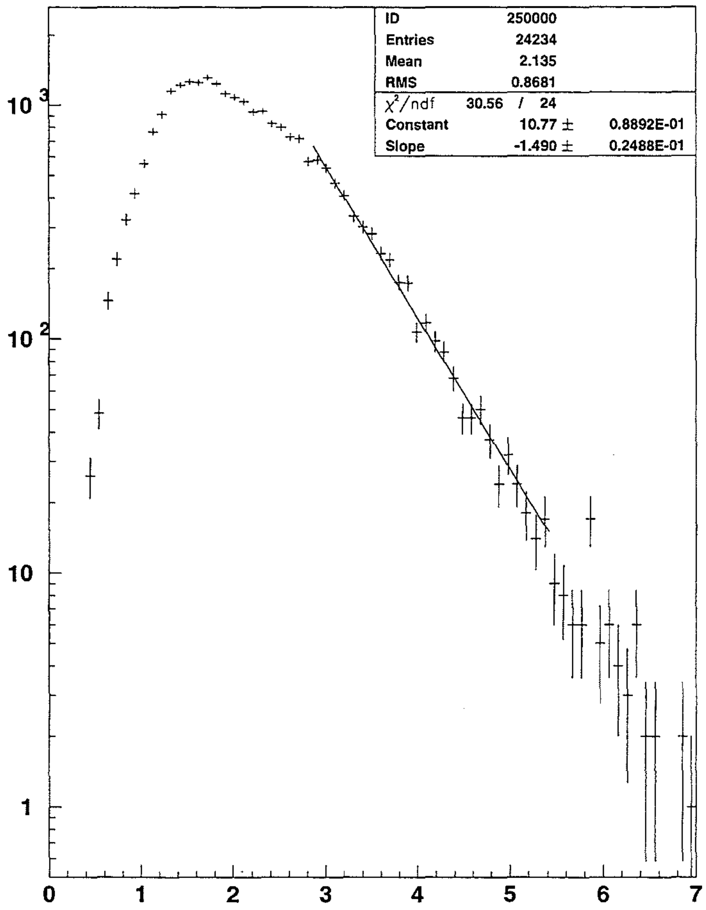

Figure 46: Monte Carlo: $\gamma_{resolved}$ uncut Monte Carlo minimum-twist $p_\perp$ spectrum.

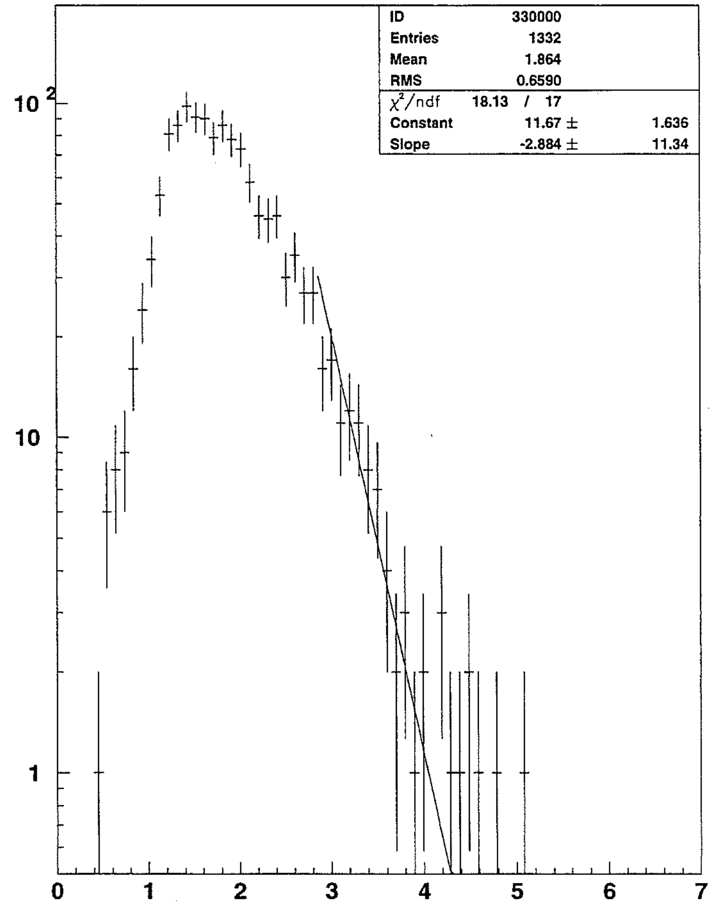

Figure 47: Monte Carlo: γ_{VMD} uncut Monte Carlo higher-twist $p_\perp$ spectrum.

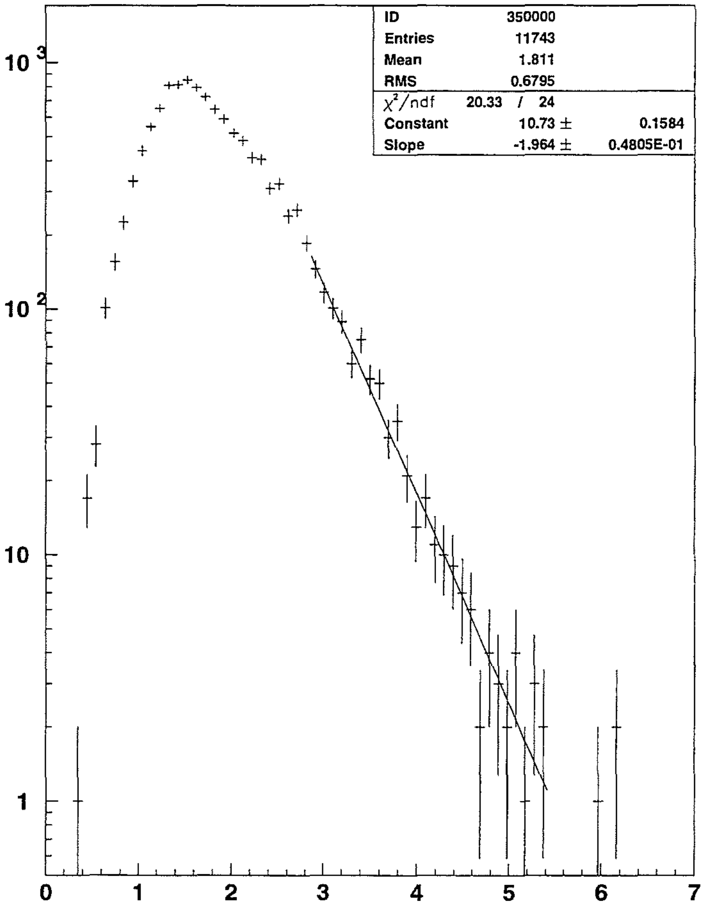

Figure 48: Monte Carlo: γ_{VMD} uncut Monte Carlo minimum-twist $p_\perp$ spectrum.

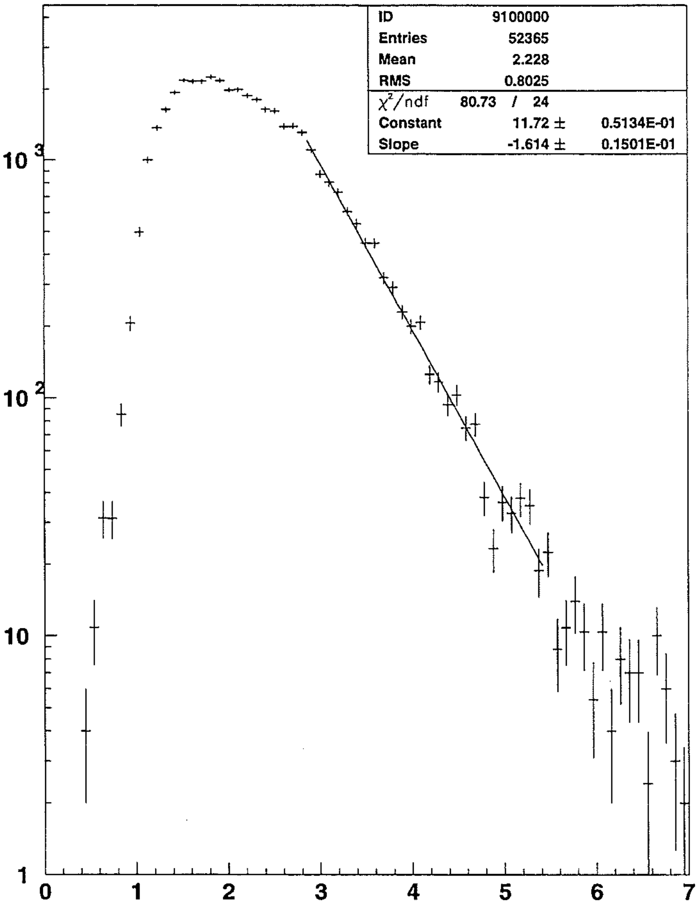

Figure 49: Data: The final optimized data $p_\perp$ spectrum.

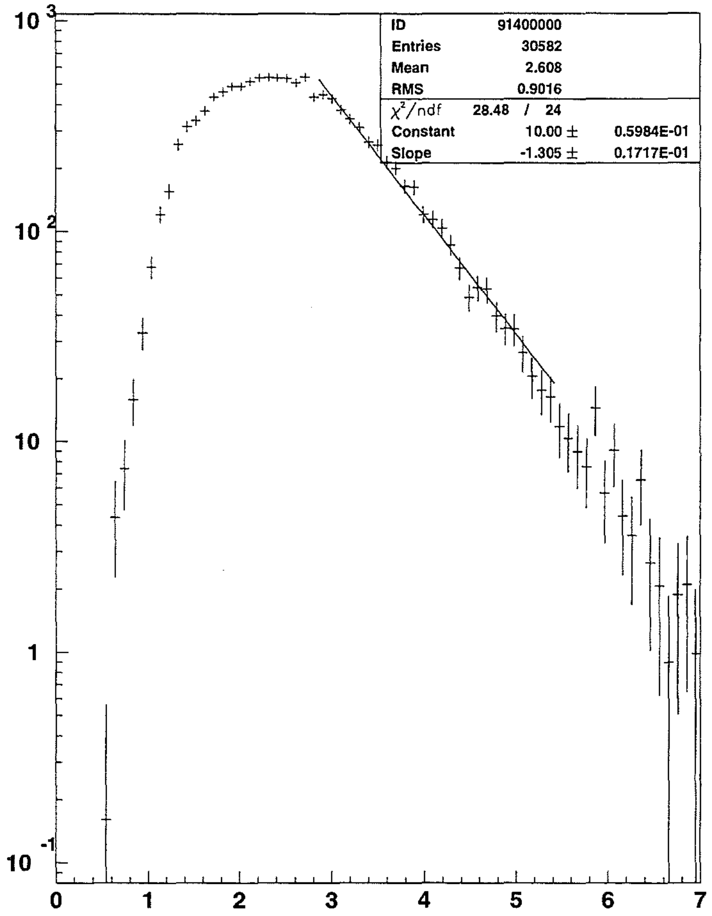

Figure 50: Monte Carlo: The final optimized Monte Carlo $p_\perp$ spectrum.

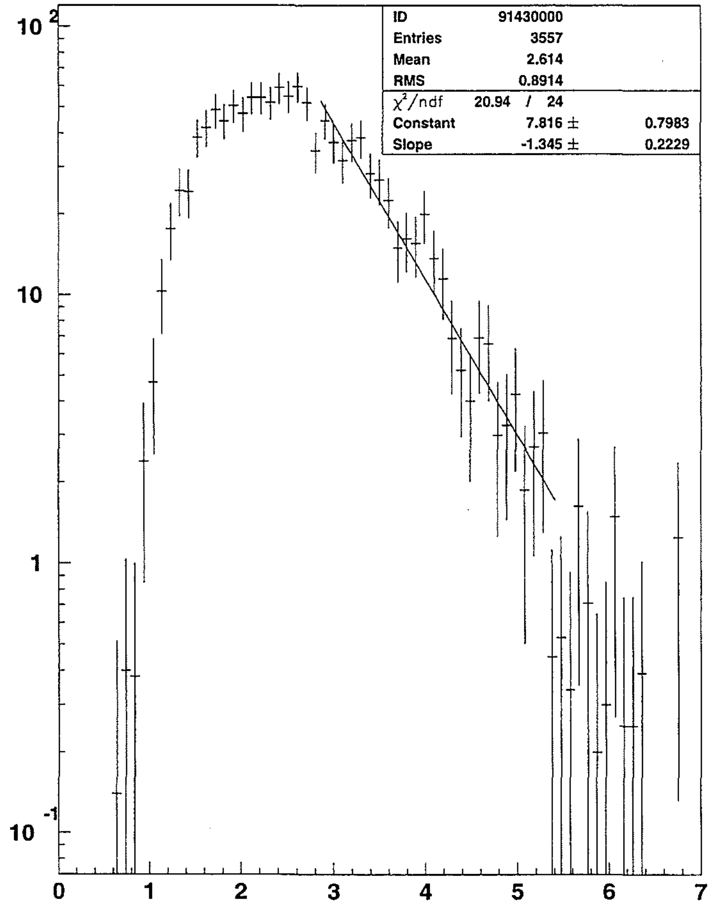

Figure 51: Monte Carlo: The final optimized Monte Carlo higher-twist $p_\perp$ spectrum.

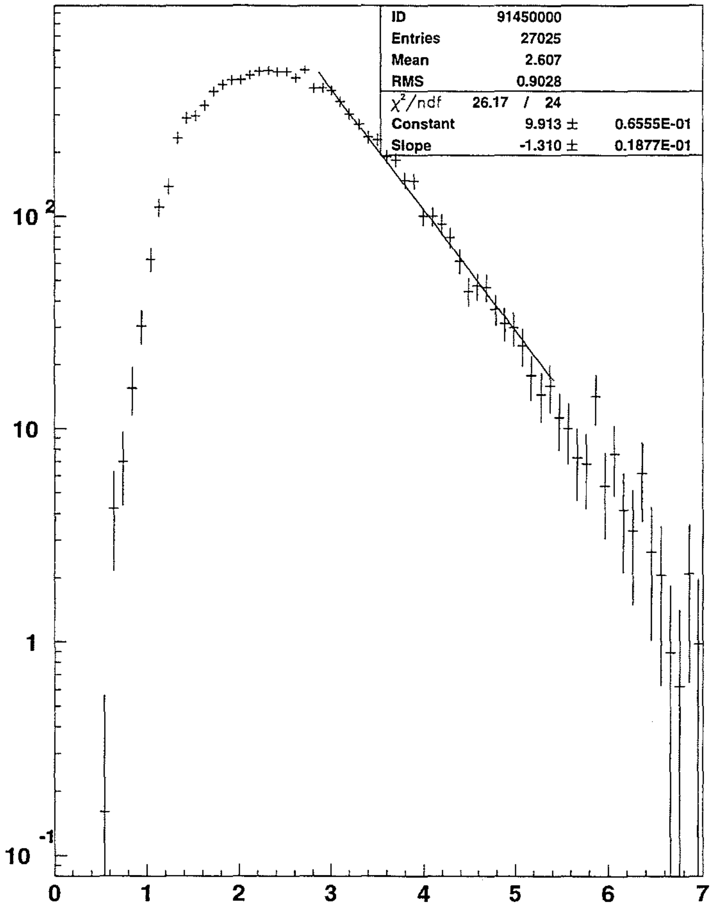

Figure 52: Monte Carlo: The final optimized Monte Carlo minimum-twist $p_\perp$ spectrum.

triggers are meant to exclude those regions.

- The detector simulator in the collimation$_{38}$ results shows it can reasonably reproduce this important kinematic variable, which is sensitive to calorimeter response, resolution effects, etc. The author believes that the detector simulation performs reasonably with respect to the two important kinematic variables to the present analysis.

- Upon examining the direct higher-twist and minimum-twist $p_\perp$ spectra, and comparing it to the resolved higher-twist and minimum-twist $p_\perp$ spectra, one can see from figures (53) and (54) how much $k_\perp$ can affect the measured $p_\perp$ spectrum. This can be explained by **$k_\perp$ promotion.** Figures (53) and (54) contrast the smearing caused by the $k_\perp$ for the direct and resolved cases, plotting the $q_\perp$ of triggered events vs the naive $p_\perp$ of those events. One is struck by how badly $k_\perp$ can affect the $p_\perp$ of a jet or initial meson **even in the ideal case.** Figures (55) and (56) show the smearing that occurs when the effects of the clusterer are added. In the resolved case, the smearing of the resultant $p_\perp$ spectrum is such as to make the higher-twist and minimum-twist $p_\perp$ spectra almost indistinguishable. Since the $q_{\perp_{min}} = 1.0$ GeV/c choice constrains the present analysis to use a large fraction of resolved photons in the $p_\perp$ spectrum, this essentially nullifies the ability to resolve minimum-twist and higher-twist at the $p_\perp$ region where resolved photons dominate–again at the lower $p_\perp$ region. Furthermore, the $k_\perp$ promotion has the ability to promote resolved events from a $q_\perp$ of the 1.0 minimum all the way to $p_\perp$ of 3.5 to 4.0 GeV/c. This means that the artifical constraints imposed by the limitations of the $q_{\perp_{min}}$ in the Monte Carlo on the $p_\perp$ spectrum affects the $p_\perp$ spectrum to a $p_\perp$ of 3.5 to 4.0 GeV/c. As one can see from the results, that is exactly where the mixture of higher-twist and minimum-twist events become at least physical.

- But what of the region past 3.5 GeV/c? The result is still beyond any plausible theoretical prediction of higher-twist fraction. Recall that the Monte Carlos used in the analysis are **Leading Order** photoproduction Monte Carlos. Obviously, QCD has contributions from more than the leading order diagrams. The extra vertices in these diagrams should also contribute something to the $p_\perp$ spectra that the leading order Monte Carlos are unable to simulate. Indeed, higher-twist photoproduction

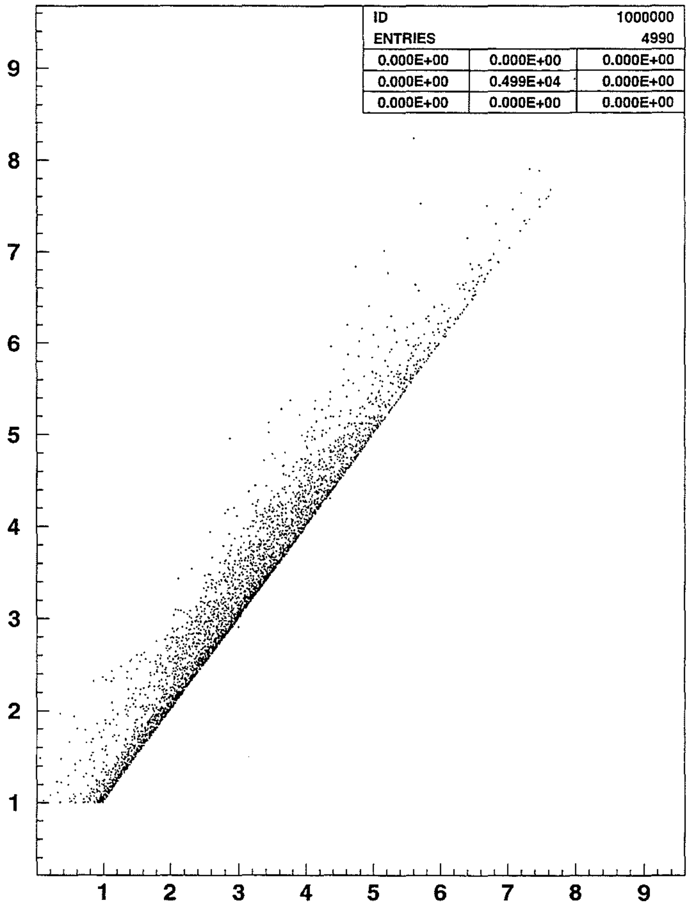

Figure 53: Monte Carlo: γ_{direct} plot of the triggered $q_\perp$ vs $p_{\perp_{naive}}$

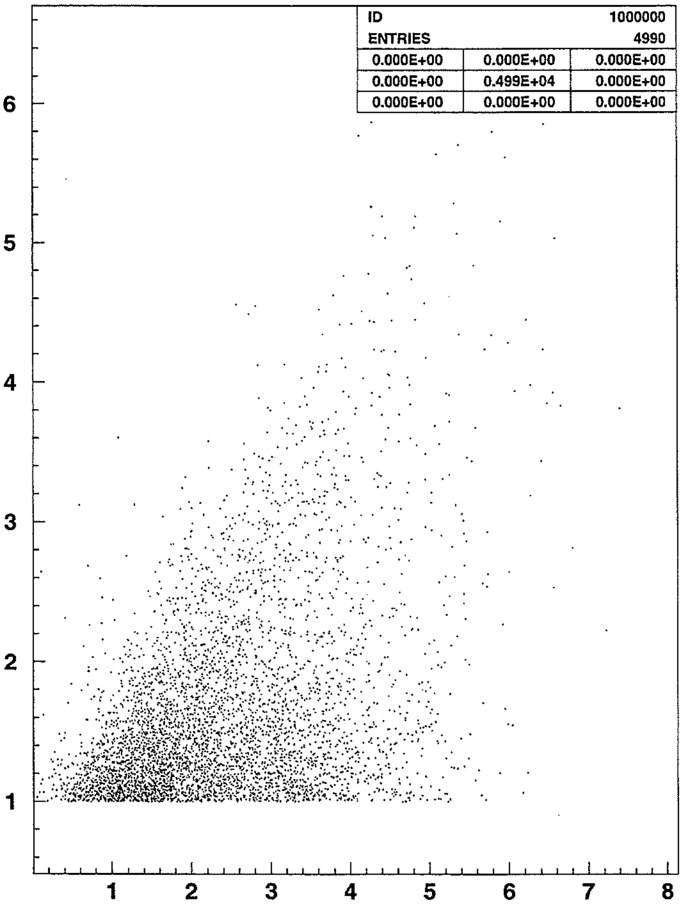

Figure 54: Monte Carlo: $\gamma_{resolved}$ plot of the triggered $q_\perp$ vs $p_{\perp_{naive}}$

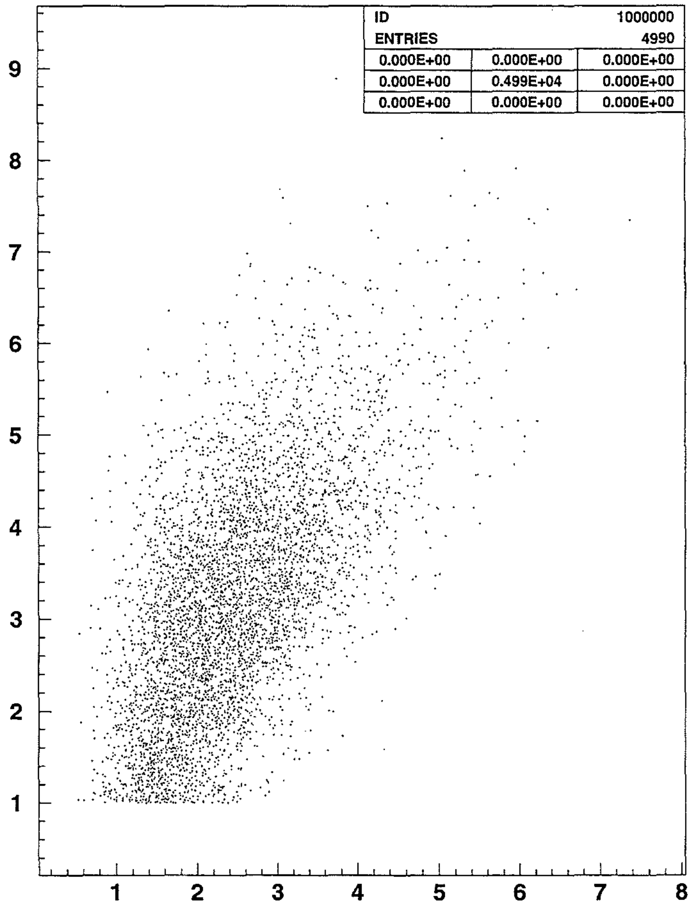

Figure 55: Monte Carlo: γ_{direct} plot of the triggered $q_\perp$ vs $p_{\perp_{cluster}}$

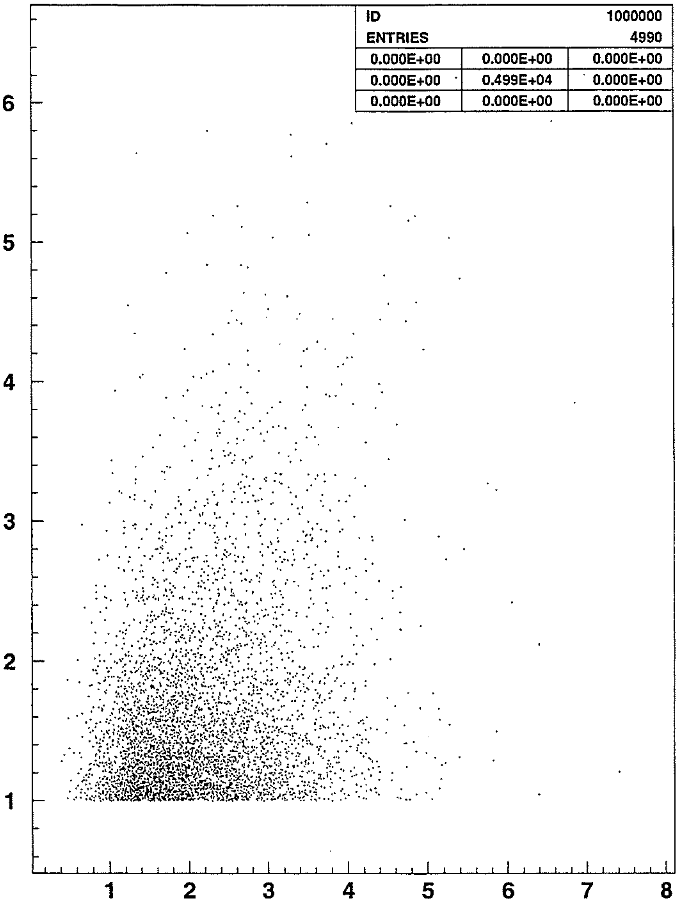

Figure 56: Monte Carlo: $\gamma_{resolved}$ plot of the triggered $q_\perp$ vs $p_{\perp_{cluster}}$

is merely a subset of the NLO set of diagrams. The NLO vertices should yield the same $p_\perp$ dependence as higher-twist events.

At this time, there are no NLO Monte Carlos that can be integrated in the detector simulator to produce a triggered $p_\perp$ spectrum to compare to our LO Monte Carlos and data. However, Jeff Owens has recently developed a NLO calculation that produces a naive $p_\perp$ spectrum. Figure (57) shows this spectrum. A simple comparison to the LO naive $p_\perp$ spectrum for triggered events is misleading due to the different trigger efficiencies of the NLO events, but if one is willing to make the assumption that the NLO behaves similarly to the LO resolved spectrum, one can infer from this figure a measurable contribution to the photoproduction $p_\perp$ spectrum, although one is not able to quantify this contribution with a reasonable degree of confidence. Also NLO, since it does fall of steeply with $p_\perp$, is yet another contributing factor to our predicament at low $p_\perp$.

4.4 Conclusions

After utilizing the proper weighting factors and kinematic cuts to obtain a $p_\perp$ spectrum, one obtains the mixtures of higher-twist and minimum-twist to the data set shown in Table (11). These mixtures indicate contributions from the artificial $q_{\perp_{min}}$ involved in pQCD as well as from the $k_\perp$ promotion effect such as to nullify the resolution of higher-twist and minimum-twist at low $p_\perp$. At higher-$p_\perp$, the resolution improves such that the prediction of the mixture becomes physical. The results at higher-$p_\perp$ suggest NLO contributions to the $p_\perp$ spectrum that would be quantifiable with a true NLO photoproduction Monte Carlo.

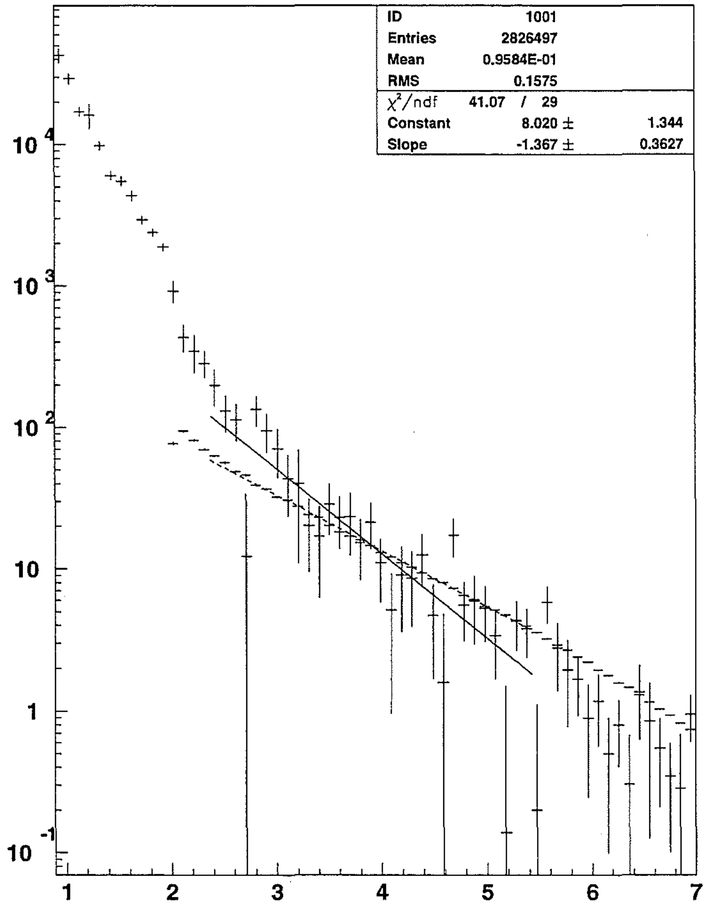

Figure 57: The NLO calculation's $p_\perp$ spectrum. The LO spectrum is dashed, while the NLO spectrum is solid. Note that in the region 3 GeV/c $< p_\perp <$ 5 GeV/c , the contributions from both spectra are comparable.

A Wire Chamber Information

The Tables (12)–(14) give some characteristics of the E683 chambers. In the E683 standard coordinate system, the beam always heads north, which is +z To keep the right-handed system, +y is up, and +x is west .

The three upstream boxes are proportional wire chambers (PWCs) as opposed to drift chambers (DCs). PWCs simply yield information that a particle registered a hit near a given wire in the PWC, as opposed to drift chambers, which yield the distance from the track to the wire.

Note that the three PWC boxes were given the names "Erin", "Colleen", and "Molly" from upstream to downstream, containing 1, 1, and 3 planes respectively. The three upstream drift chamber boxes, containing two planes each, are the "Zhu" chambers, after Qiuan Zhu, who was responsible for their maintenance. The three boxes immediately downstream of the magnet, which contained two planes each, are called the "Iowa" chambers for the University of Iowa personnel who rebuilt and maintained them. The two boxes upstream of the MCAL are the "monster" chambers, so-called for their great size.

Chamber planes which measure X have wires running in the Y direction and vice versa. U and V planes have wires running in a direction at an angle to the vertical. The E683 convention defines U planes as those with wires running from lower left to upper right looking along the beam (or Z) axis. V planes are those with wires running from lower right to upper left. It is often difficult to design chambers with both X and Y planes, and U and V planes in conjunction with X planes are a compromise design permitting hit location in both directions.

Resolutions:

Preliminary numbers:

- PWC: Wire spacing is 1.9538 mm.
- DC 1-6: Approx 1 mm
- DC 7-12: Approx 800 μ
- DC 13-19: Approx 700 μ

Box	Plane	Direction of Measurement	Active Area	Number of Wires
Erin	PWC 1	Y	18″×15″	192
Colleen	PWC 2	Y	18″×15″	192
Molly	PWC 3	X	26.25″×13″	320
Molly	PWC 4	U	26.25″×13″	352
Molly	PWC 5	V	26.25″×13″	352

Table 12: PWC Characteristics: Some characteristics of E683 proportional wire chambers. U and V planes have wires running at an angle with the vertical. The cant of the wires in PWC 4 and 5 is ±15°.

Box	Plane	Direction of Measurement	Active Area	Number of Wires
Zhu 1	DC 1	X	38.5″×17.5″	40
Zhu 1	DC 2	X and Y	38.5″×17.5″	40
Zhu 2	DC 3	X	53.5″×30.5″	46
Zhu 2	DC 4	X	53.5″×30.5″	48
Zhu 3	DC 5	X	63.5″×38.5″	44
Zhu 3	DC 6	X and Y	63.5″×38.5″	44

Table 13: Upstream DC Characteristics: Some characteristics of E683 upstream drift chambers. All upstream DC planes had small inactive areas centered on the beam line. DC 2 and 6 are delay line planes with wires that measure x directly and measure y by measuring the time difference between readouts at the top and bottom of the plane.

Box	Plane	Direction of Measurement	Active Area	Number of Wires
Iowa 1	DC 7	X	$104'' \times 76''$	84
Iowa 1	DC 8	X	$104'' \times 76''$	85
Iowa 2	DC 9	X	$104'' \times 76''$	85
Iowa 2	DC 10	X	$104'' \times 76''$	84
Iowa 3	DC 11	X	$104'' \times 76''$	85
Iowa 3	DC 12	X and Y	$104'' \times 76''$	84
Monster 1	DC 13	X	$132'' \times 68''$	144
Monster 1	DC 14	U	$132'' \times 68''$	192
Monster 1	DC 15	V	$132'' \times 68''$	192
Monster 2	DC 16	X	$132'' \times 68''$	144
Monster 2	DC 17	X	$132'' \times 68''$	144
Monster 2	DC 18	U	$132'' \times 68''$	144
Monster 2	DC 19	V	$132'' \times 68''$	144

Table 14: Downstream DC Characteristics: Some characteristics of E683 downstream drift chambers. DC 12 is a delay line plane. In the monster chambers, the cant in the U and V planes is $\pm 16.7^o$. One X plane in Monster 1 was uninstrumented.

Greg further points out that "...rough results for the resolutions of the drift chambers are dissapointingly high: the resolutions **should** be on the order of $\approx$ 100-200 μ."[7] (emphasis added).

B Beam Monte Carlo

B.1 Overview and History

The E683 Beam Monte Carlo was written during 1992-1993 by the author. It has been subsequently modified by Chafiq Halli and Phillip Birmingham, as well as maintained and enhanced by the author through November 1995. Only the version developed by the author is discussed here.

B.2 Motivation

The reasons for developing a Beamline Monte Carlo were twofold:

- As a diagnostic tool in order to understand beam behavior. In a photon beam, any diagnostics used (scintillators, etc), will degrade the beam quality simply because devices read charge output. In order to read charge output, radiation lengths must be inserted in the beamline, forcing the creation of electron-positron pairs not in the beam otherwise. Therfore the diagnostics for the beam were very limited. The Beam Monte Carlo used simple geometric arguments and known inputs in order to simulate the production of photons along PB6 and PB7. Once E683 was confident that the Monte Carlo was accurately simulating known quantities (RESH recoil values, magnet on/off pair ratios, RESH efficiency, beam movement, etc.), the beam behavior in areas where there was limited information from the data could be inferred from the Monte Carlo outputs. As a quick example, the Monte Carlo predicted that the problem of double bremsstrahlung was not significant for the photon energies relevant to our experiment that passed our trigger.

- As a front end for event generation Monte Carlos. Recall that the photoproduction cross-section is strongly coupled to incoming photon energy. Therfore, the shape of the triggered photon spectrum must be used as an input. However, the experiment observed triggered events, which consist of the triggered photon spectrum convolved with the photoproduction cross-section and the triggering efficiency. The Beam Monte Carlo is used to predict the triggered photon spectrum.

B.3 Input

The inputs are from an E687 electron run during the 1991-1992 Fixed Target Run. They consist of the incoming energy of electrons at PB6RAD, as well as their projection angles and positions. Figure (58) shows the input energy spectrum for the electrons. The other defining parameters of the Monte Carlo are the Si tagging resolution, the BCAL resolution, the $p_\perp$ kick of the magnets in PB6 and E687, the geometry of the upstream beamline (i.e., the placement of the charge counters along the beamline as well as the limiting aperatures at various sections of the beamline where the particles are either acted upon, evaluated, or both, called **stations**), the radiation length at the stations, and the geometry of the RESH. Minor parameters included various hardware effects such as the BCAL offset, and various minor physical processes such as multiple scattering.

The stations used in the author's version of the Beam Monte Carlo are:

- Before PB6RAD (for input data from electrons).
- At PB6RAD.
- At PB6SW bend point.
- At the RESH
- At the E687 target.
- At the PB7AN1 bendpoint.
- between PB7AN1 and PB7AN2.
- At the PB7AN2 bendpoint.
- At the E687 IE and pair counters.
- At the E683 target.

Table (15) shows the position of each station as well as its aperature size, magnetic $p_\perp$ kick (for magnets), and radiation length in the author's original version of the Beamline Monte Carlo.

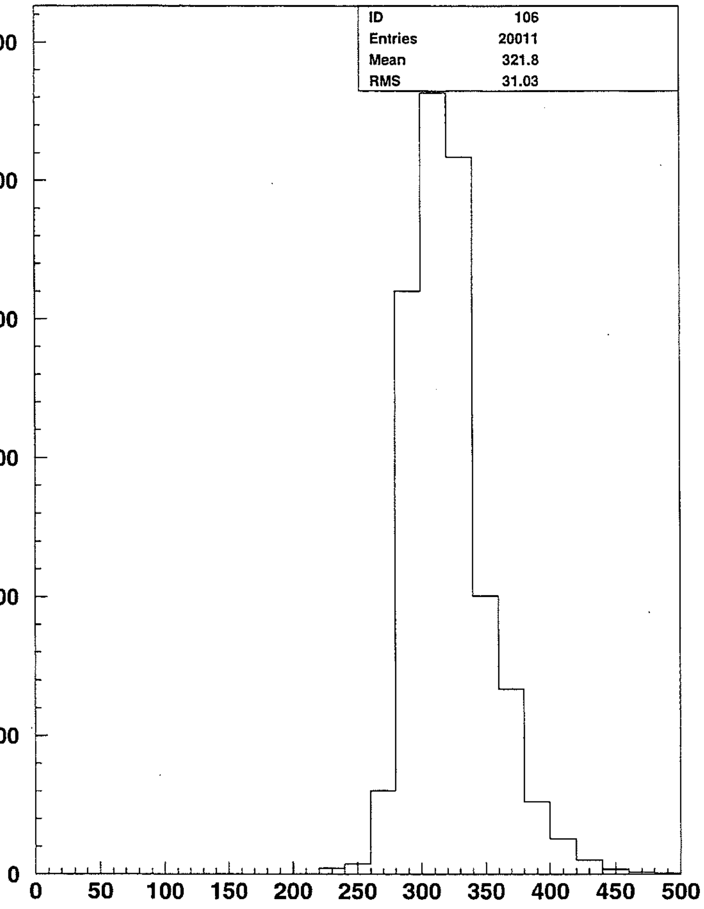

Figure 58: The incoming electron energy spectrum at PB6RAD

Station	Position	Aperature size (x,y)	$p_\perp$ kick	X_0
PB6RAD	0.0	(0.075,0.070)	n.a.	0.27
PB6SW bendpoint	5.62	(0.065,0.045)	2.47 +x	n.a.
RESH	20.10	n.a.	n.a.	n.a.
E687 target	40.94	(0.127,0.127)	n.a.	0.15
PB7AN1 bendpoint	44.02	(0.127,0.127)	0.4 +y	n.a.
between PB7AN1 and PB7AN2	49.11	(0.127,0.127)	n.a.	0.07
PB7AN2 bendpoint	54.19	(0.127,0.127)	0.85 -y	n.a.
E687 IE	65.00	(0.051,0.051)	n.a.	0.03
E683 target	68.22	(0.102,0.102)	n.a.	n.a.

Table 15: Positions, aperature sizes, $p_\perp$ kick for magnets, and radiation lengths for each station in the Beamline Monte Carlo. Note: n.a. means not applicable for this type of station. All positions and sizes are in m. All $p_\perp$ kicks are given in GeV/c, with the direction of the $p_\perp$ noted where applicable. All radiation lengths are given in X_0.

B.4 Algorithmic Overview

The actual transport algorithm is rather straightforward, but tedious. Essentially, the particles are transported at each station through the fraction of a radiation length that exists for the station . At this point, electrons and positrons can bremsstrahlung photons, and photons can pair produce. Multiple scattering can also take place. At each station, the position of each particle is checked to see if it would hit the limiting aperature for that station. If it does, that particle and its energy are lost. For each station with a magnet, the particle receives a $p_\perp$ kick consistent with the magnetic field. The particle's projection angle is then changed accordingly. Also, at each charge counter, the charged particles' positions are checked to see if they would be detected by the counter. At the RESH, the recoil electrons follow their projection angle to a RESH counter. Showering takes place such that a neighboring counter may also be included in the signal from that particle interacting with the RESH.

B.5 Output Examples

The output of the Monte Carlo is a series of histograms, including, but by no means limited to the following:

- Position of each particle at each station.
- Energy of each particle at each station.
- Projection angles of each particle at each station.
- Energy spectrum of the RESH under various conditions.
- Multiplicity of each type of particle at each station.
- Various photon kinematics for photons that pass the E683 trigger.

The photon flux and geometric RESH efficiency were previously shown. Figure (59) shows the energy spectrum for recoil electrons from RESH element 1 for all events. Figure (60) shows the energy spectrum for recoil electrons from RESH element 1 for all events with the beam loss added to the measured RESH energy. Figure (61) shows the energy spectrum for recoil electrons from RESH element 1 for all events with the beam loss added to the measured RESH energy, with cuts used by another collaborator in her study of RESH energies in the data.

Figure (62) shows the electron energy spectrum at the E683 target for all events. Figure (63) shows the electron multiplicity at the E683 target for all events. Figure (64) shows the photon energy spectrum at the E683 target for all events. Figure (65) shows the photon x-position at the E683 target for all events. Figure (66) shows the photon y-position at the E683 target for all events. Figure (67) shows the photon multiplicity at the E683 target for all events.

B.6 User Parameters

The user is able to vary the following parameters:

- The resolution of the Si Tagging system (default: 0.0225).
- PB7AN1/2 on or off (default: on).
- BCAL resolution (default: 0.45).
- PB6RAD length (default: 0.2 radiation lengths).
- Estimated beam movement.

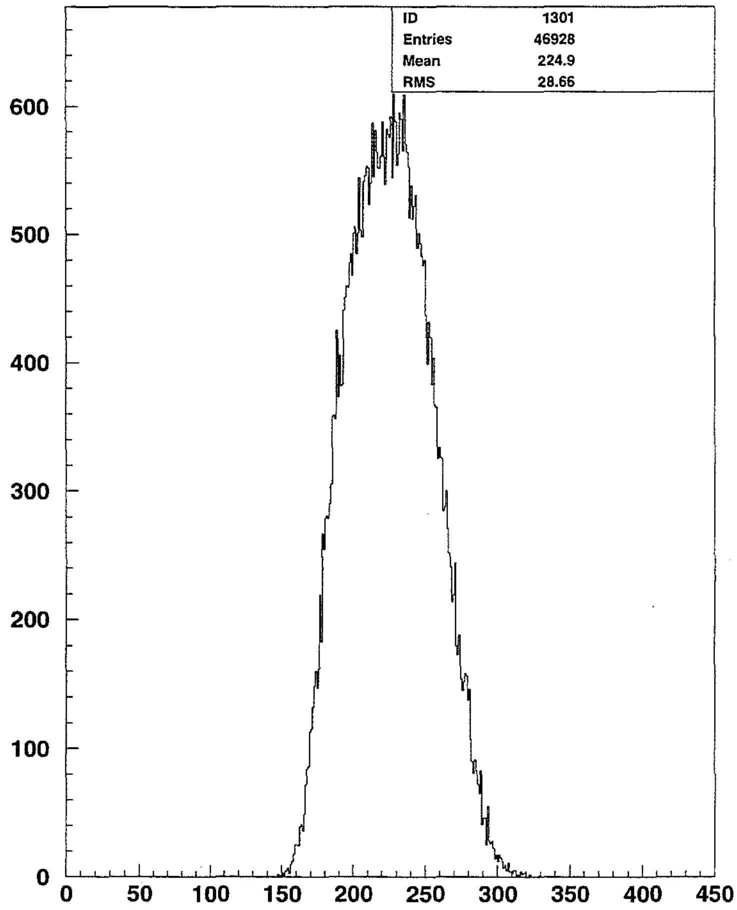

Figure 59: The recoil electron energy spectrum at RESH 1.

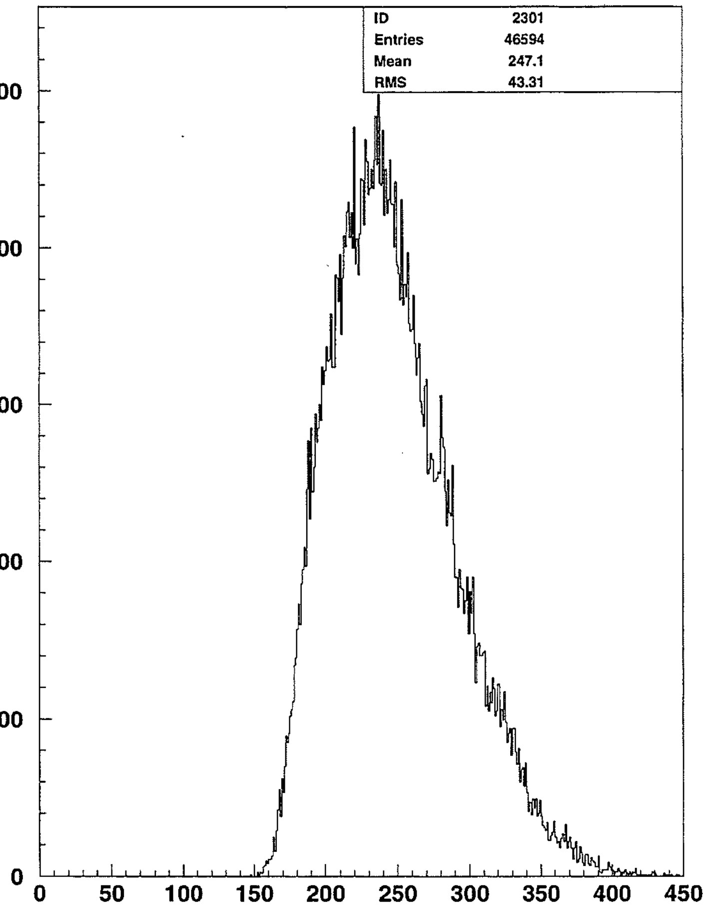

Figure 60: The recoil electron energy spectrum at RESH 1 with beam loss added to the spectrum.

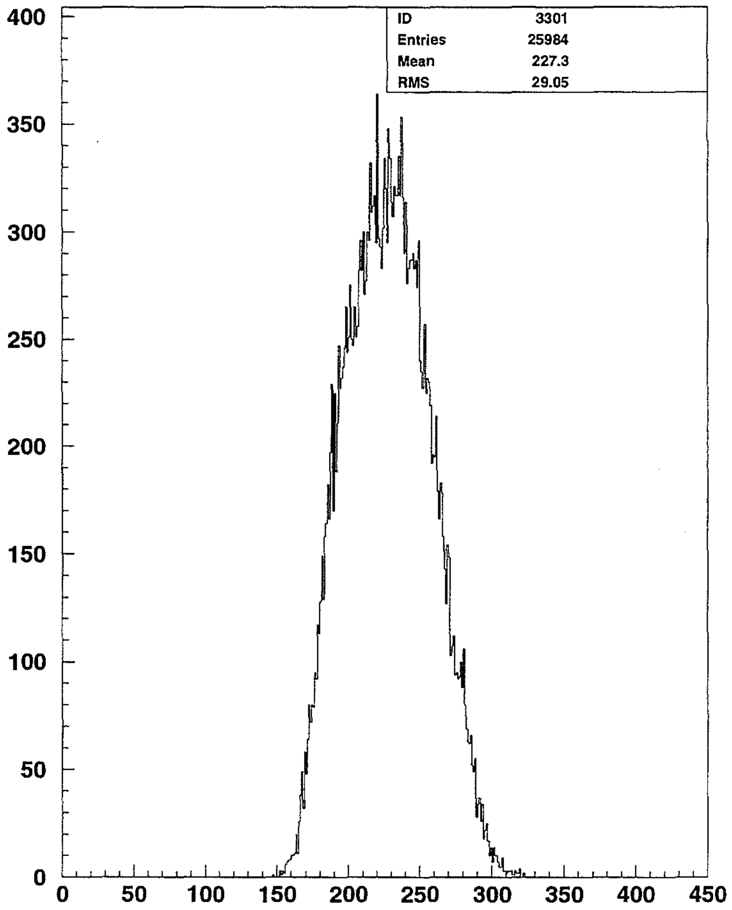

Figure 61: The recoil electron energy spectrum at RESH 1 with beam loss added and simulated DLN cuts imposed on the spectrum.

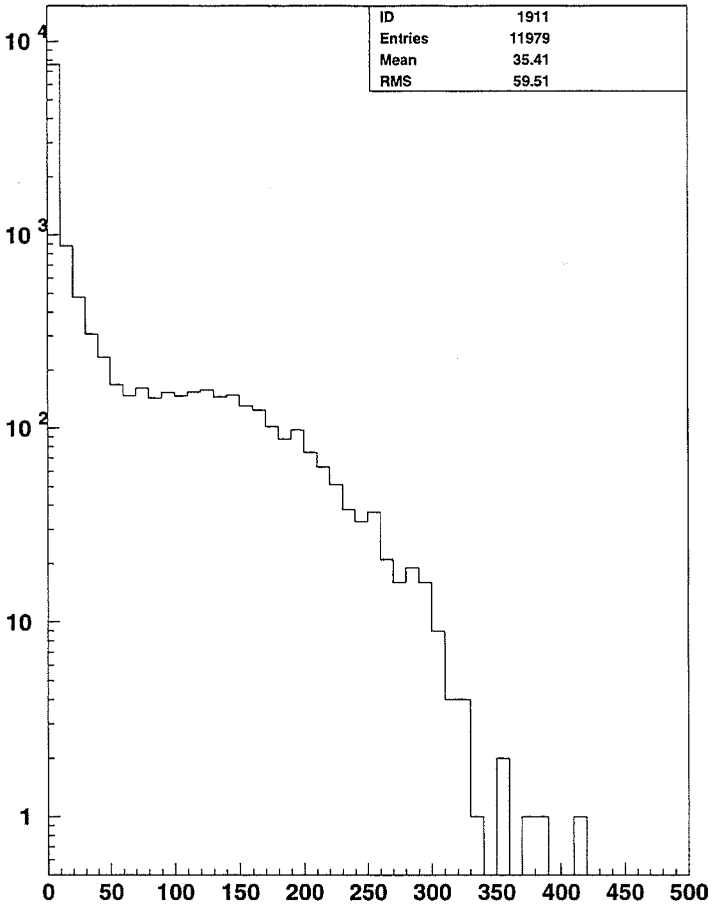

Figure 62: The electron energy spectrum at the E683 target.

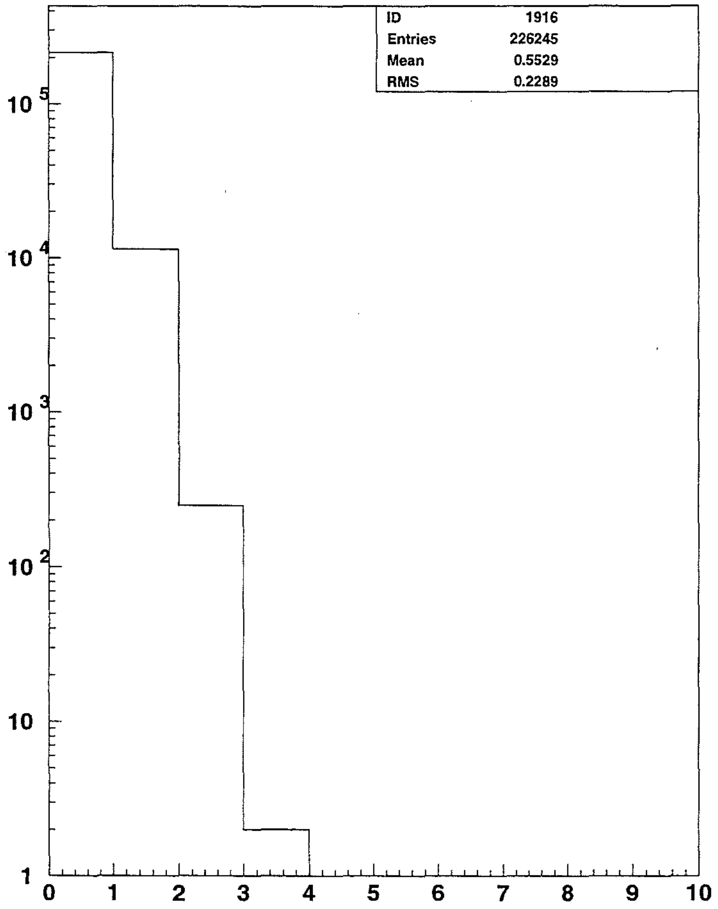

Figure 63: The electron multiplicity at the E683 target.

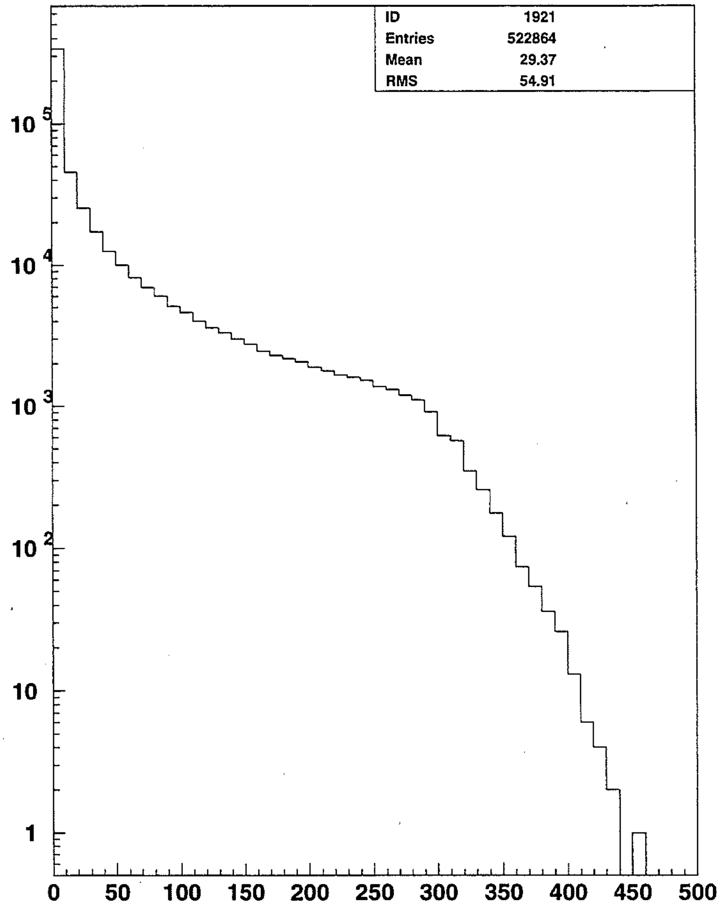

Figure 64: The photon energy spectrum at the E683 target.

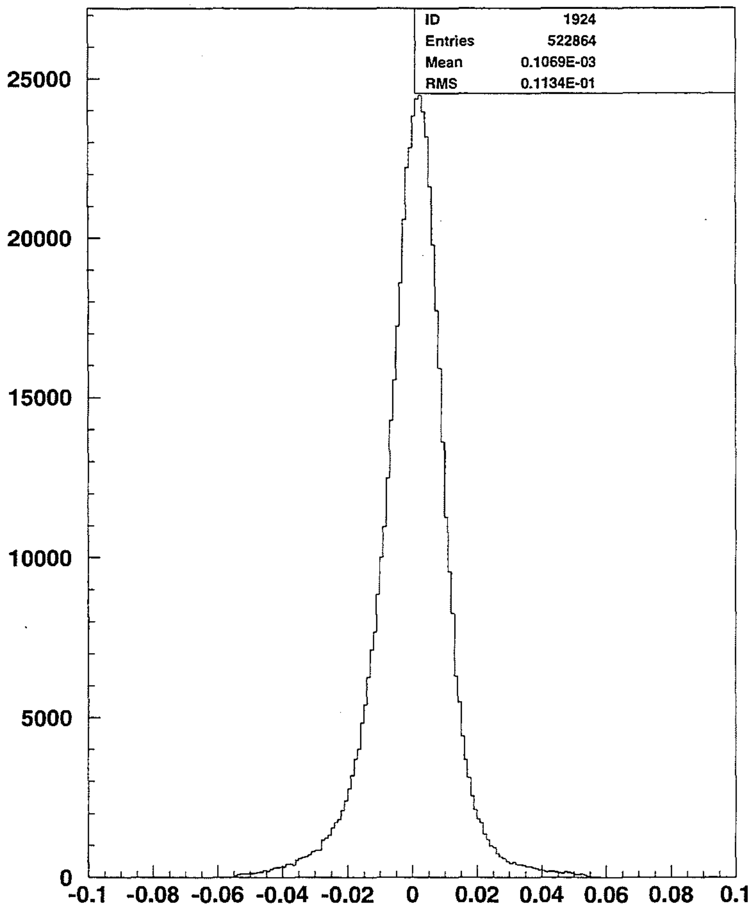

Figure 65: The photon x-position at the E683 target.

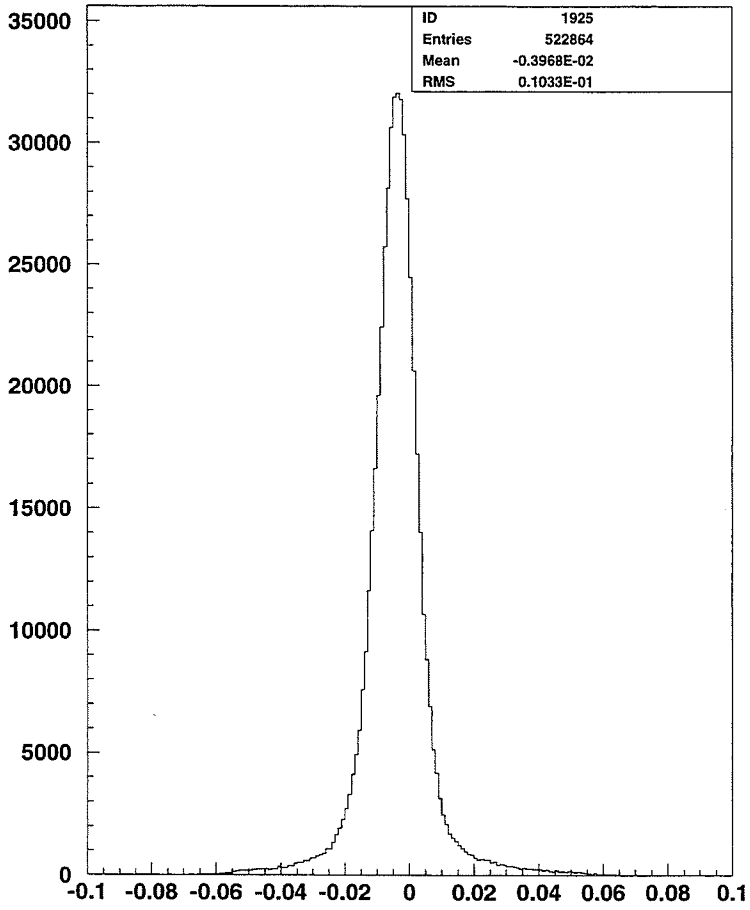

Figure 66: The photon y-position at the E683 target.

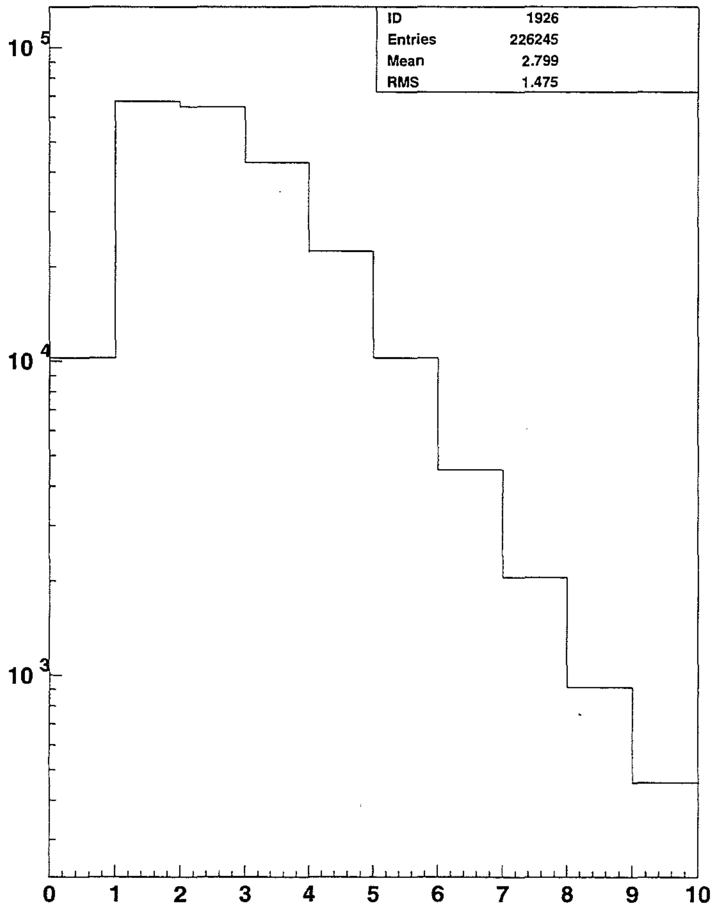

Figure 67: The photon multiplicity at the E683 target.

- Hydrogen or nuclear target at E683 (default: Hydrogen).
- RESH in the upstream or downstream position (default: downstream).

For more information please see the internal notes provided by the author [18] [19].

C Showering Simulation

C.1 Motivation

The former E683 standard showering algorithm was relatively accurate for shower simulation in the Main Calorimeter on a grand emsemble level. However, limitations became apparent on an event-by-event basis.

The author integrated suggestions by Dr. Peter Kasper with his own into a new showering simulation. The features of the new showering simulation are:

- Improved accuracy of the modelling of showers on an event-by-event basis. The mean and RMS values for the fractional energy in a given tower and its neighbors struck by a hadronic or electromagnetic particle are in better accord with calibration data.
- Transparent substitution over the previous showering algorithm.
- CPU demands comparable or less than the previous algorithm.
- A more intuitive algorithm.

Many of the details relevant to the development of this simulation were released in an E683 internal note written by the author [21].

C.2 Data Sample

The data sample for comparison to the new showering algorithm is composed of π (for hadrons) and e calibration data on $4'' \times 4''$, $6'' \times 6''$, and $8'' \times 8''$ towers at 30, 60, and 90 GeV.

C.2.1 Cuts in Data Sample

The following cuts were made to the calibration sample to ensure the integrity of the calibration sample:

- The tower aimed at was the tower with the most energy in the calorimeter. This ensured that the data sample did not include that part of the beam that hit a neighboring tower, etc.

- The Main Calorimeter measured at least 1/3 of the nominal beam energy. This ensured the integrity of the sample against μ events that formed a trigger.

- The fractional energy in the A′ and A layers was at least 60% of the total energy in the calorimeter. This ensured the data sample against showers that would develop late. Since any calorimeter tower diverged outward from the beamline at approximately 7^o from the beam axis in the LAB frame, and the calibration beam collided with the tower along the beam axis, a late-developing shower could deposit its energy in a neighboring tower.

- For plane 13 of our Wire Chambers, the particle could only register a hit within two wires of the wire most often hit; this ensured the data sample against fringe beam effects.

- (For electrons only) One and only one hit must be registered in plane 13 of the Wire Chambers, to avoid multiple e events.

The cuts were also made to the simulated sample, with the plane 13 cut replaced by an cut of ± 2″ from the center of the simulated beam (the simulated beam was itself smeared out in a Gaussian distribution to simulate the actual beam spread).

C.3 Showering Algorithm

C.3.1 Parameters

The parameters for the improved showering algorithm are:

- **n(r)**: The number of 'lumps' of energy within a radial interval between r and r+δ(r). In the simulation n(r)=a×r +b for all r.

- **a**: Empirically determined from calibration data. a=2.0 for e, and 0.0 for π.

- **b**: Empirically determined from calibration data. b=20.0 for e and 6.0 for π.

- **δ(r)**: Fixes the radial interval between intervals where n(r) is evaluated. Empirically determined to be 0.2″.

- σ_l: Determines the width of the lumpiness distribution. $\sigma_l = A(\log(B) - \log(E))$, where A and B are empirically determined and depend on tower type, energy, and particle type, and E is the energy of the incoming particle.

- σ_E: A blurring factor for the shower's internal distribution of energy. This is **not** a resolution factor for the overall energy in the shower: whatever energy the particle starts with is the energy spread in the shower. Other subroutines in the E683 simulation handle the calorimetry resolution.

C.3.2 Algorithm

The algorithm is relatively straightforward. The incoming position and energy of the particle are supplied to the algorithm. The algorithm then determines the proper σ_l and σ_E factors. Then in radial intervals of δ(r), n(r) **lumps**, or units of energy are generated. The number of lumps in a given radial interval varies according to the given σ_l, as well as the dependence n(r)=a×r +b. Each lump contains a certain amount of the original energy of the particle; at each radial ring part of the remaining amount of energy is distributed evenly among those lumps in the ring, with the σ_E determining the intra-ring lump energy variation. The energy in each ring therefore also varies according to the radial position of the ring. This continues until all the energy of the particle is distributed. The position of each lump is then used to determine what tower the lump falls in, and energy is distributed to that tower. The tower energies are then passed onto the rest of the E683 simulation.

The parameters were varied until the optimal matches for the means and RMS to the data were made. They were tuned seperately for each energy, tower type, and particle type (e or π). The distributions where the means and RMS were compared were the following:

- Fractional energy in the main calorimeter contained in the central tower.

- Fractional energy in the main calorimeter contained in an adjoining tower of the same tower type.

- Fractional energy contained in all the neighboring towers to the central tower.

- Fractional energy contained in all the next-to-neighboring towers to the central tower.

The cuts as aforementioned were implemented in the calibration data and the improved and old showering simulation.

C.4 Results

C.4.1 Hadronic Results

The best way to determine the results is to observe the histograms containing the four distributions mentioned above. Figure (68) contains the distributions for the fractional energy in the central tower for the calibration data (a), the improved simulation (b), and the standard simulation (c). Figure (69) contains the distributions for the fractional energy in a neighboring tower for the calibration data (a), the improved simulation (b), and the standard simulation (c). Figure (70) contains the distributions for the fractional energy in all neighboring towers for the calibration data (a), the improved simulation (b), and the standard simulation (c). Figure (71) contains the distributions for the fractional energy in all next-to-neighboring towers for the calibration data (a), the improved simulation (b), and the standard simulation (c).

C.4.2 Electromagnetic Results and Energy Dependence

The e results were also tuned to various energies. A few examples are shown below.

Figure (72) contains the distributions for the fractional energy in the central tower for the calibration data (a), and the improved simulation (b). Figure (73) contains the distributions for the fractional energy in a neighboring tower for the calibration data (a), and the improved simulation (b). Figure (74) contains the distributions for the fractional energy in all neighboring towers for the calibration data (a), and the improved simulation (b). Figure (75) contains the distributions for the fractional energy in all next-to-neighboring towers for the calibration data (a), and the improved simulation (b). Figure (76) contains the distributions for the fractional energy in the central tower for the calibration data (a), and the improved simulation (b). Figure (77) contains the distributions for the fractional energy in a neighboring tower for the calibration data (a), and the improved simulation (b). Figure (78) contains the distributions for the

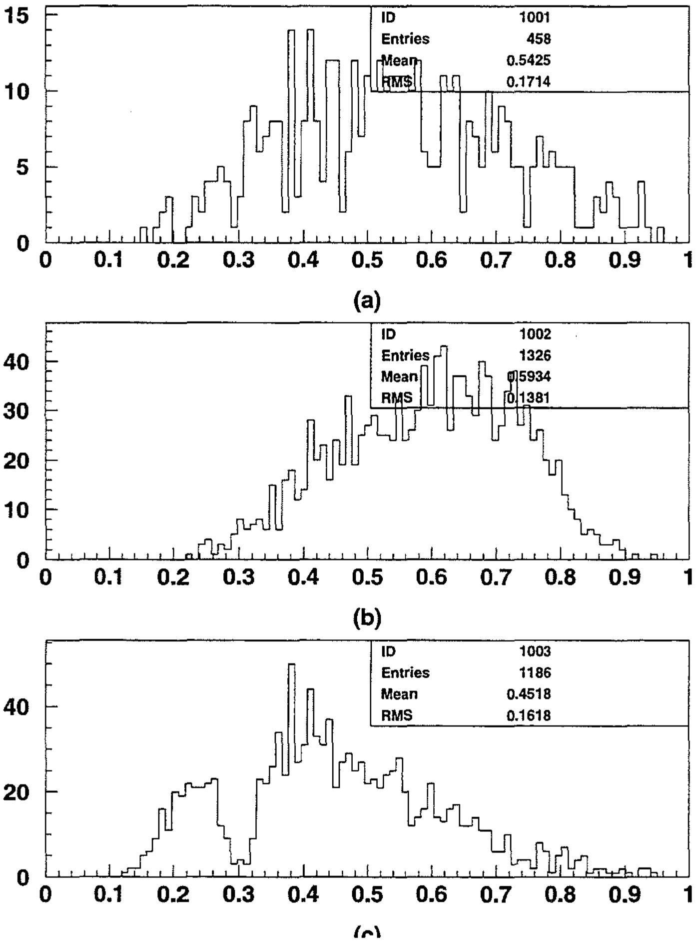

Figure 68: Comparison of the fractional energy contained in the central tower for 30 GeV π on tower 30. (a) is the calibration data, (b) is the improved simulation, and (c) is the standard simulaton.

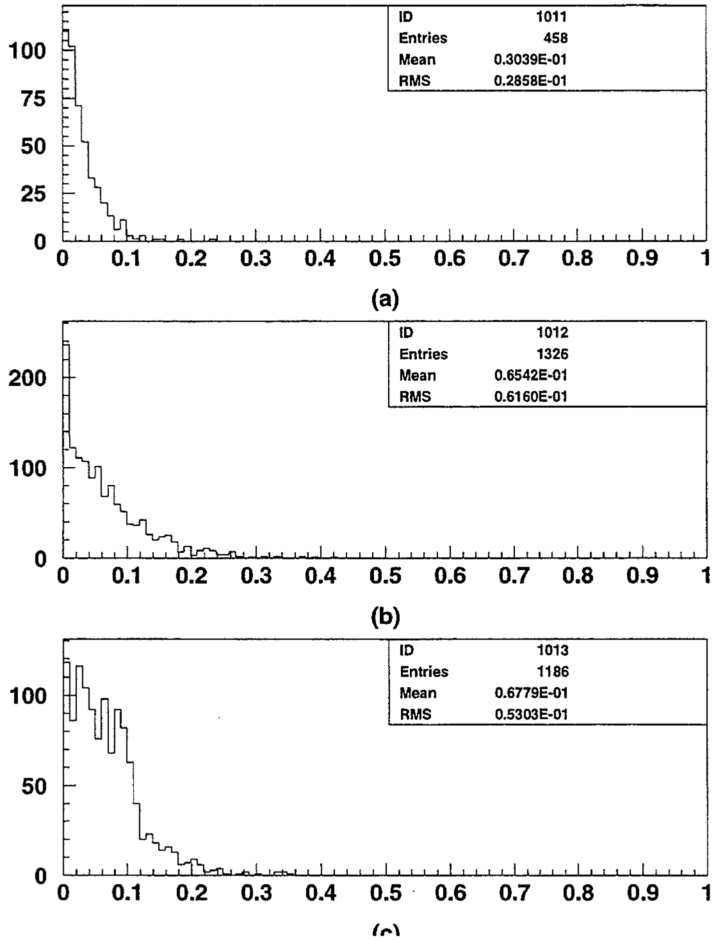

Figure 69: Comparison of the fractional energy contained in a neighboring tower for 30 GeV π on tower 30. (a) is the calibration data, (b) is the improved simulation, and (c) is the standard simulaton.

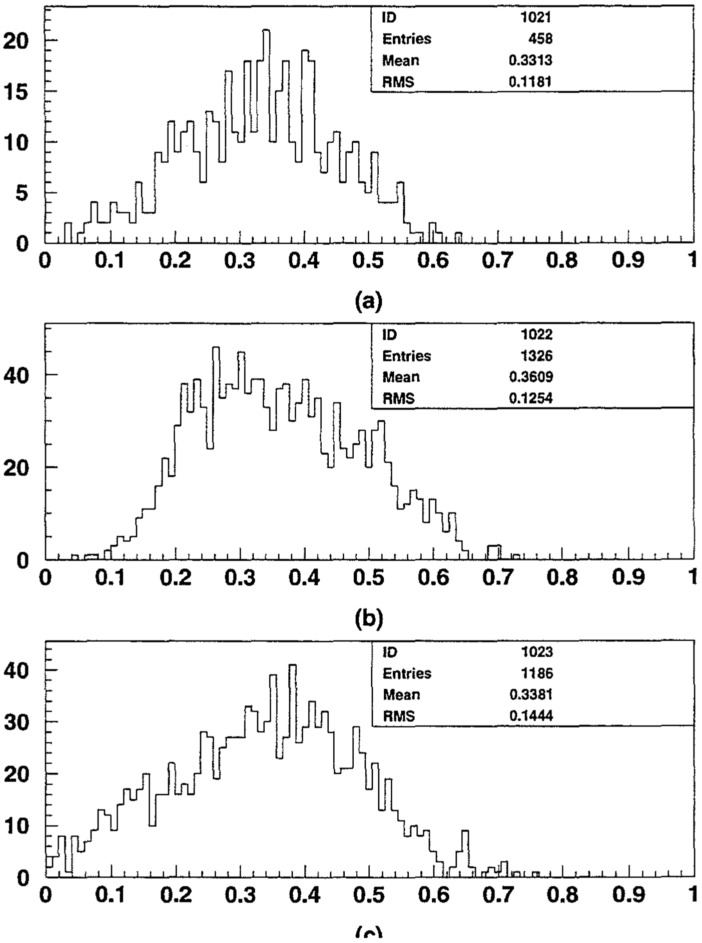

Figure 70: Comparison of the fractional energy contained in all neighboring towers for 30 GeV π on tower 30. (a) is the calibration data, (b) is the improved simulation, and (c) is the standard simulaton.

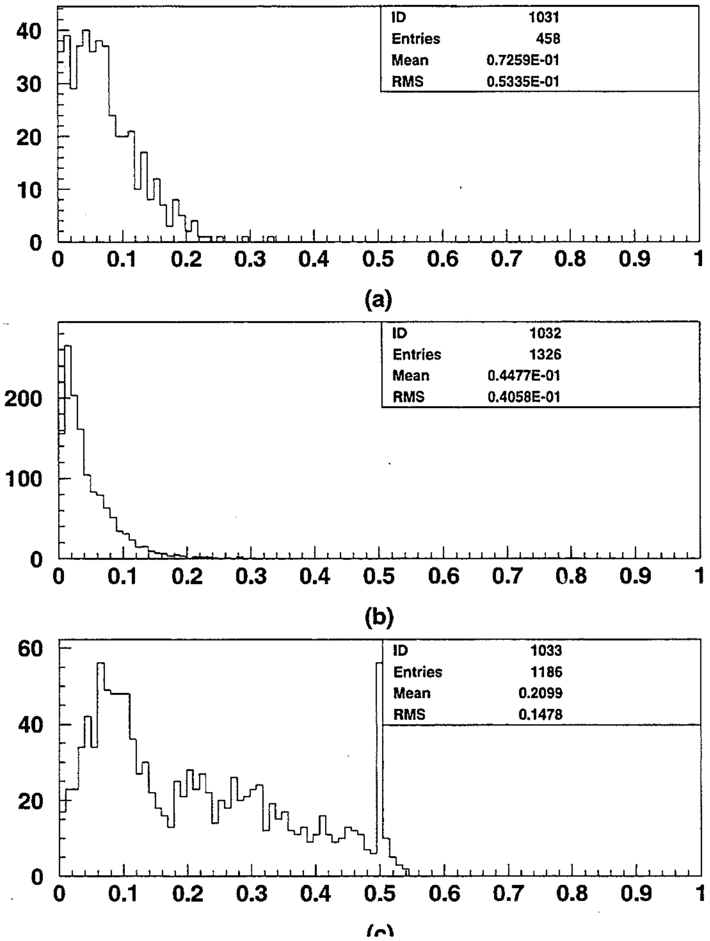

Figure 71: Comparison of the fractional energy contained in all neighboring towers for 30 GeV π on tower 30. (a) is the calibration data, (b) is the improved simulation, and (c) is the standard simulaton.

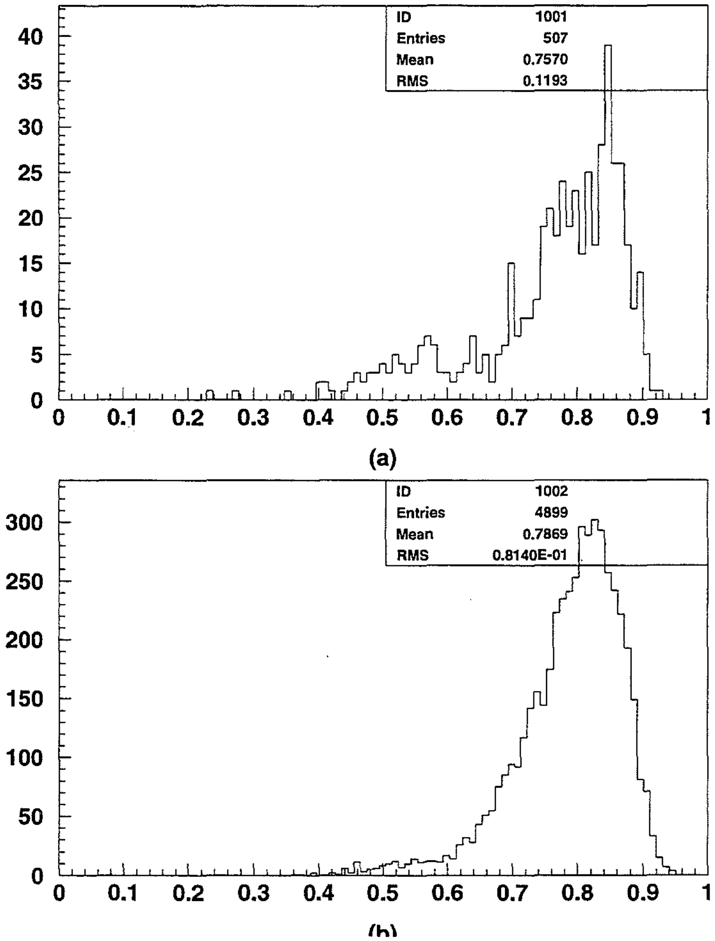

Figure 72: Comparison of the fractional energy contained in the central tower for 30 GeV e on tower 30. (a) is the calibration data, (b) is the improved simulation.

fractional energy in all neighboring towers for the calibration data (a), and the improved simulation (b). Figure (79) contains the distributions for the fractional energy in all next-to-neighboring towers for the calibration data (a), and the improved simulation (b).

C.4.3 Implementation

In tests in October 1994, a test of 5000 events on FNALO showed that the new simulation (with an initial steering program) used 4 min 13 sec of CPU time vs the previous simulation using 3 min 58 sec. Improvements to the new showering algorithm speed

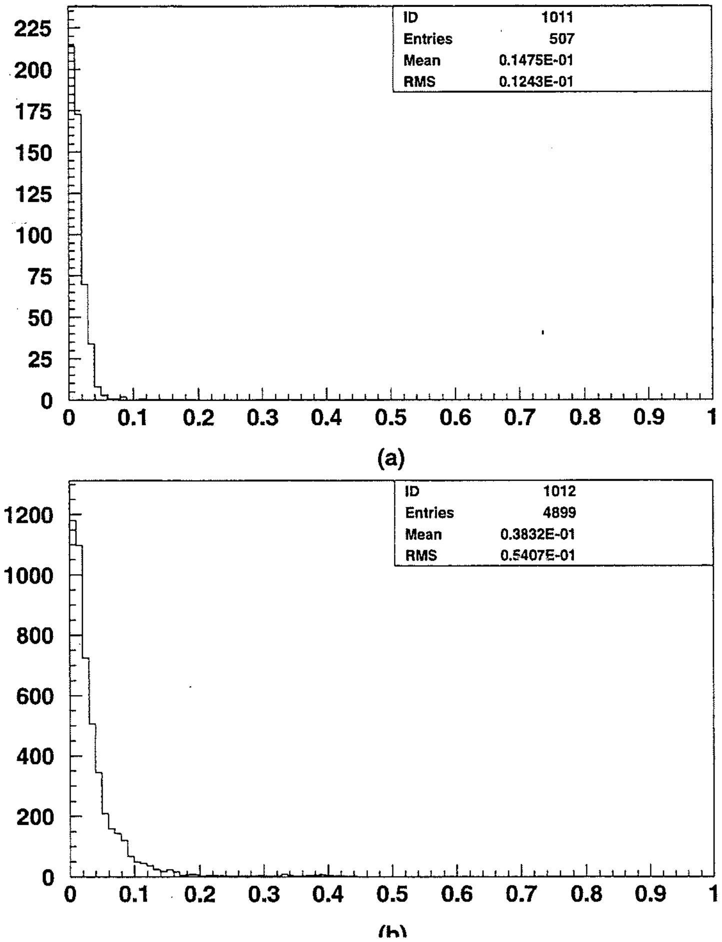

Figure 73: Comparison of the fractional energy contained in a neighboring tower for 30 GeV e on tower 30. (a) is the calibration data, (b) is the improved simulation.

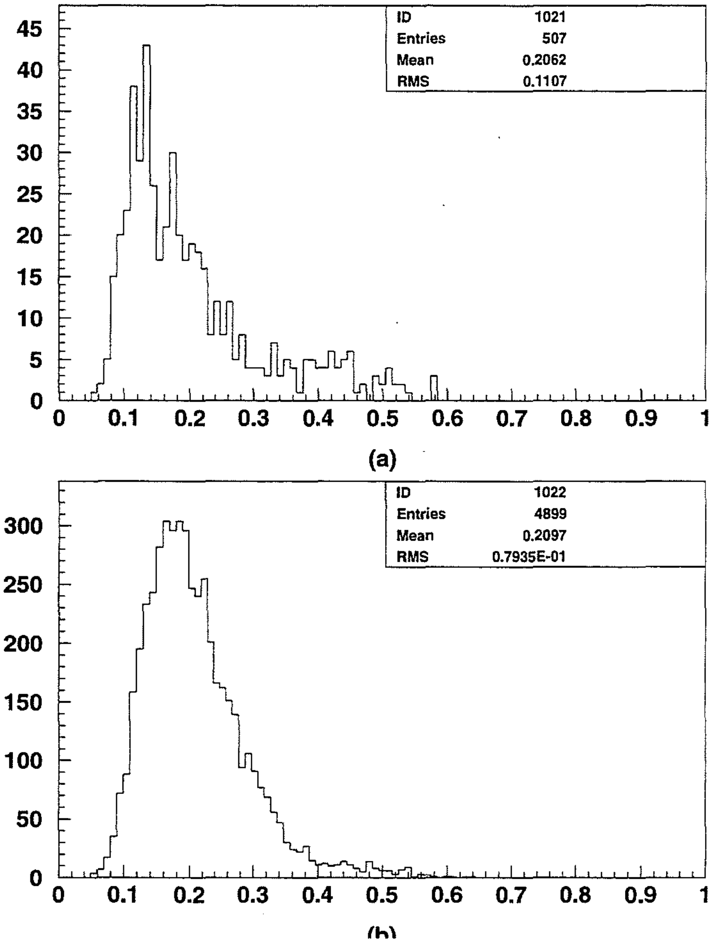

Figure 74: Comparison of the fractional energy contained in all neighboring towers for 30 GeV e on tower 30. (a) is the calibration data, (b) is the improved simulation.

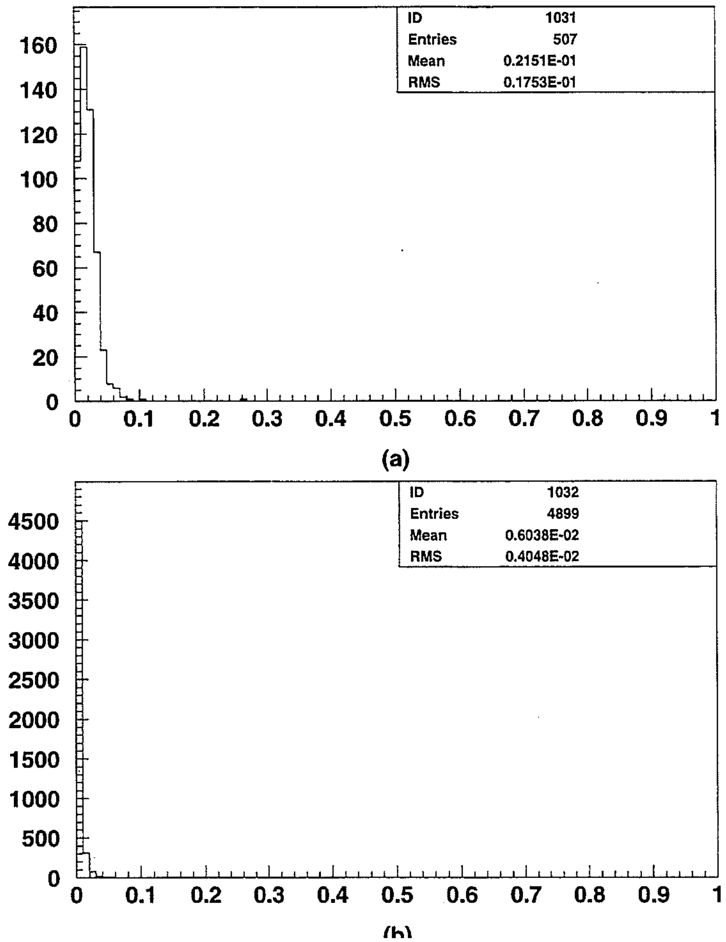

Figure 75: Comparison of the fractional energy contained in all next-to-neighboring towers for 30 GeV e on tower 30. (a) is the calibration data, (b) is the improved simulation.

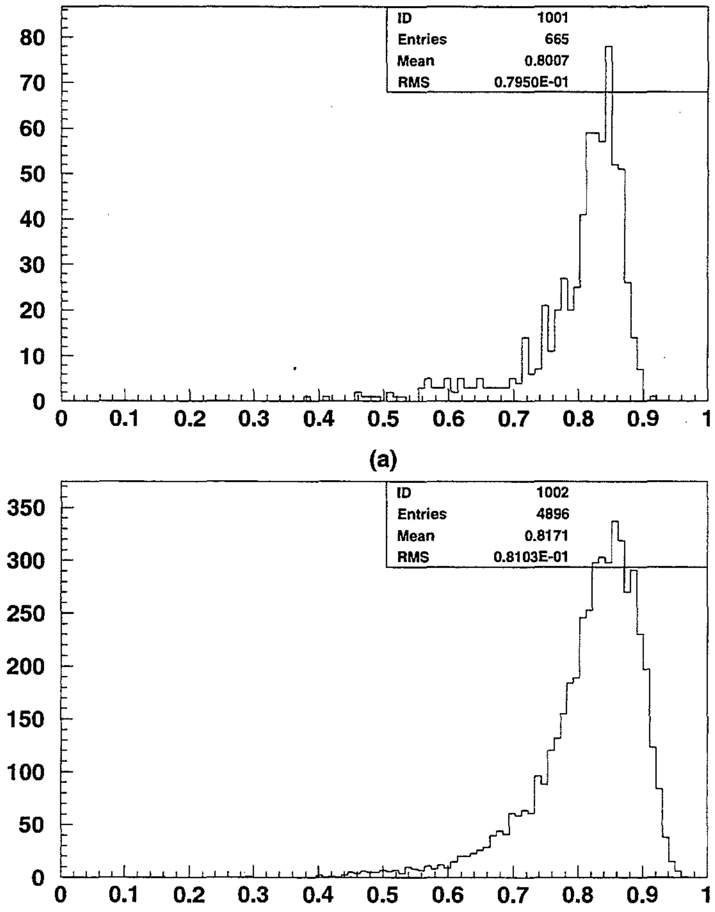

(a)

(b)

Figure 76: Comparison of the fractional energy contained in the central tower for 60 GeV e on tower 30. (a) is the calibration data, (b) is the improved simulation.

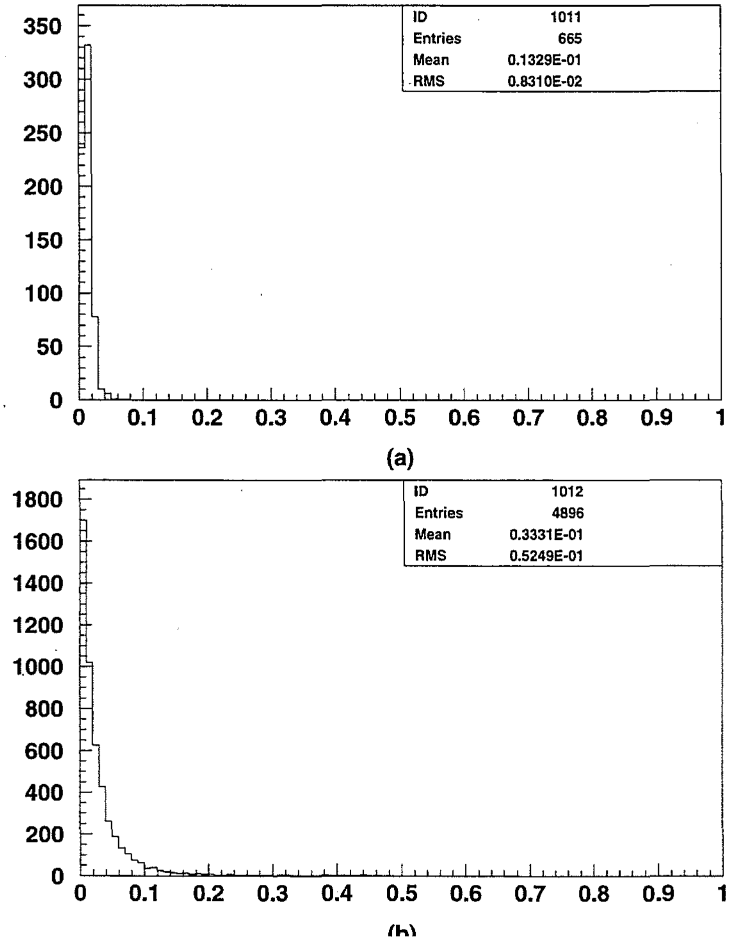

Figure 77: Comparison of the fractional energy contained in a neighboring tower for 60 GeV e on tower 30. (a) is the calibration data, (b) is the improved simulation.

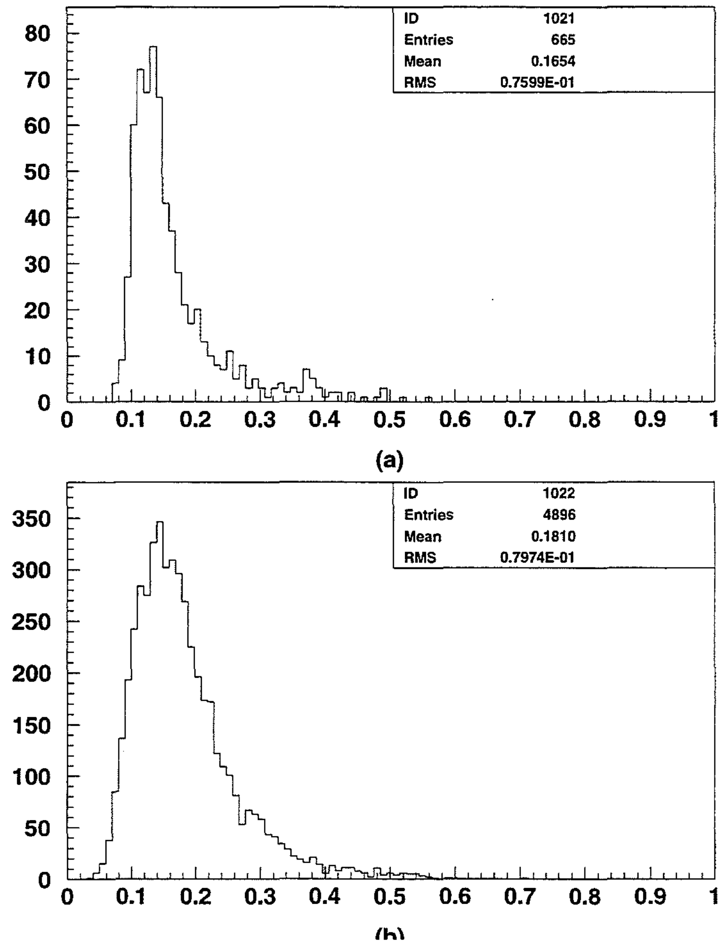

Figure 78: Comparison of the fractional energy contained in all neighboring towers for 60 GeV e on tower 30. (a) is the calibration data, (b) is the improved simulation.

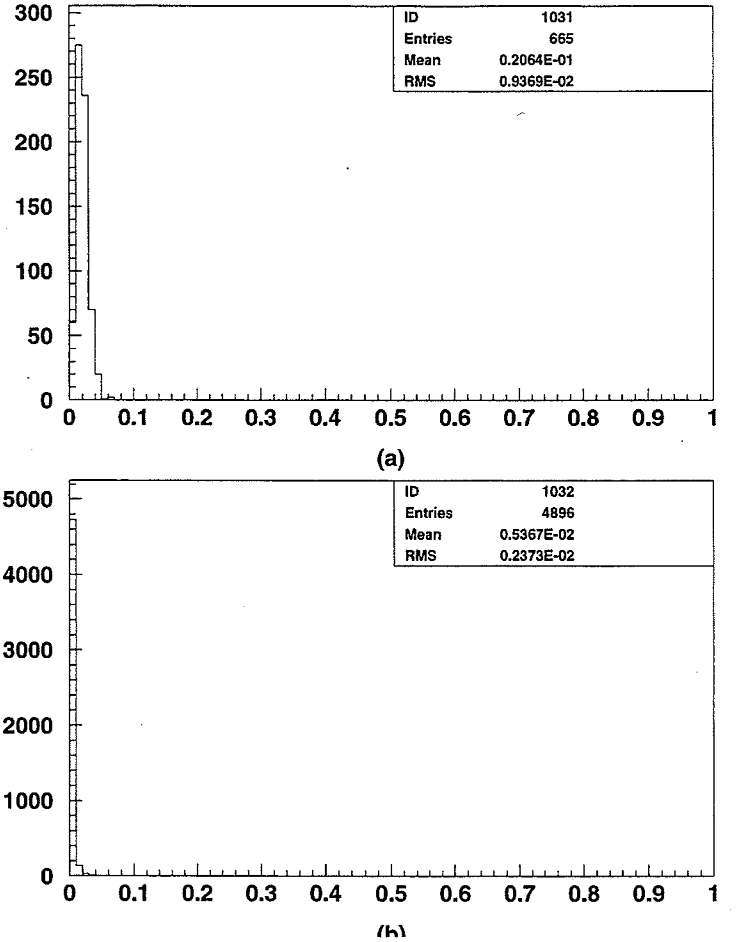

Figure 79: Comparison of the fractional energy contained in all next-to-neighboring towers for 60 GeV e on tower 30. (a) is the calibration data, (b) is the improved simulation.

have increased its speed since then. Further improvements are possible if necessary. The user merely needs to copy the subroutine and link to the new version instead of the old.

D FSLIB Unix-VMS Writing Routines

D.1 Overview

The universities on E683 have several computers with the Unix operating system. In order to utilize these computers to analyze the E683 data set, the author modifed the FSLIB library to have write-capability for Unix subarchitectures IRIX and AIX.

D.2 Capabilities

The following tranlations have been tested using the FSLIB write routines:

- Data produced by E-683 using VMS FSLIB write functions have been read on fndaui using Unix FSLIB read functions (disk and tape).
- Data generated by Unix FSLIB write functions have been read by fndaui using Unix FSLIB read functions (disk and tape).
- Data generated by Unix FSLIB write functions have been read on FNE683 using VMS FSLIB read functions (disk and tape).

D.3 Translation Characteristics

The following characteristics of the translation should be noted:

- This version of FSLIB invokes opens, closes, and writes using the BUFIO library developed by John Marraffino.
- This version of FSLIB does NOT produce labels on the tapes. BUFIO routines do nothing toward that goal.
- These functions handle the byte swapping of the longwords such that the file is **byte-swapped** relative to its normal appearance on Unix. This means that a longword consisting of four bytes which would normally appear order 1234 on Unix appears 4321 on these tapes (example: 'FRED' would be 'DERF' relative to Unix standard).
- The FSLIB read functions have been modified in order to ensure link-compatibility with the FSLIB write functions. Specifically, the library for these functions is now

compiled with the -qextname qualifier, and patches to c functions in the library were made in order to provide the option of compiling with the -qextname option. In order to provide full compatibility with the FSLIB write functions, the users should obtain the modified FSLIB read functions as well.

- When one mounts a tape produced by using Unix FSLIB write functions on a VAX, the user must specify mount/foreign/blocksize=#blks where blks is the blocksize specified in writing the tape to the Unix FSLIB write function fsfiow (see below).
- The blocksize used for writing is 4096 bytes. This may be relatively inefficient for writing short blocks of data, as the VMS size was 512 bytes. Interested parties can engage in further work to optimize the byte size if it is deemed desirable.

Further information can be found in the internal note distributed by the author [22].

References

[1] G.A. Schuler and T. Sjorstrand, *Towards a Complete Description of High-Energy Photoproduction.* CERN-TH. 6796/93

[2] J. Owens, private communication March 31, 1994.

[3] J. A. Bagger and J. F. Gunnion, *Higher-Twist Contributions, QCD, and Inclusive Meson photoproduction at High* $p_\perp$. Phys Rev D., vol 25 no. 9, 1 May 1982, p. 2291.

[4] G. Ingelman, *Twister-A Monte Carlo for QCD High-* $p_\perp$ *Scattering.* Computer Physics Communications 46 (1987) 217-240.

[5] G. Ingelman, *Lucifer-A Monte Carlo for QCD High-* $p_\perp$ *Photoproduction.* Computer Physics Communications 46 (1987) 241-261.

[6] J. Butler, *High Energy Photoproduction.* Fermi National Accelerator Laboratory January 15, 1989. Unpublished.

[7] G. Morrow, *Calibration of the E683 Main Calorimeter.* Rice University MA Thesis 1993.

[8] M. Traynor, *Beam Counters General Information.* E683 Internal note.

[9] M. Traynor, *Hodoscope General Information.* E683 Internal note.

[10] M. Traynor, *Trigger Digrams for E683.* E683 Internal Note. July, 1992.

[11] M. Traynor, *Construction of the E683 Hodoscope and Preliminary Calibration of the E683 Main Calorimeter.* Rice MA thesis, May 1990.

[12] A. Hocker, *The A-dependence of Jet Photoproduction.* Rice BS Thesis. April, 1994.

[13] J. Marraffino, *Momentum Resolutions of the E683 Spectrometer Magnet.* E683 Information Note. February 26, 1992

[14] D. Lincoln, *Design and Construction of a Beam Calorimeter for E683 at FNAL.* Rice MA Thesis. August 1989.

[15] D. Lincoln, *Observation of Jet Photoproduction and Comparison to Monte Carlo Simulation.* Rice PhD Thesis. August 1993.

[16] K. Johns, *The Calibration, Response, and Energy Resolution of a Segmented, Sampling Hadron Calorimeter Between 10 and 130 GeV/c.* Rice University MA Thesis 1983.

[17] J. Owens, private communication June 13, 1995.

[18] M. Traynor, *WB Beam Manual.* E683 Internal Note. April 5, 1993.

[19] M. Traynor, *Summary of Beam Behavior using Beam Monte Carlo.* E683 Internal Note. April 1993.

[20] Application Software Group Computing and Networks Division, *HBOOK Reference Manual Version 4.20.* CERN PM0082.

[21] M. Traynor, *Results of the New Showering Algorithm and Comparison to the Standard E683 Showering Algorithm and Calibration Data.* E683 Internal Note. October 1994.

[22] M. Traynor, *FSLIB Write Functions for Unix.* E683 Internal Note. March 19, 1992.